Hydrodynamics of nanomachines in biology

Erik Gauger

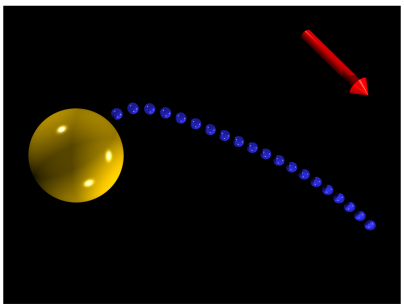

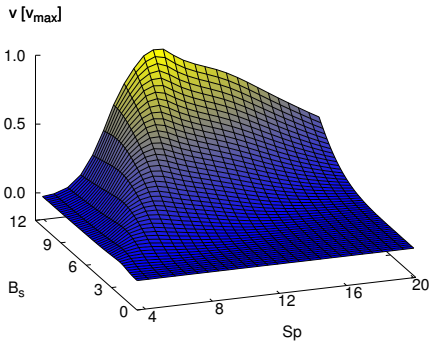

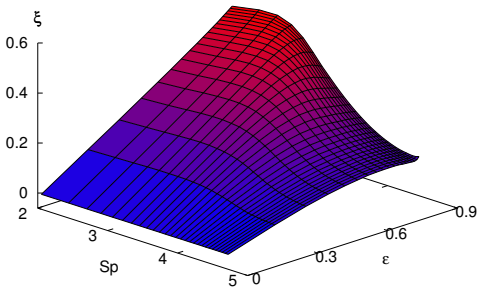

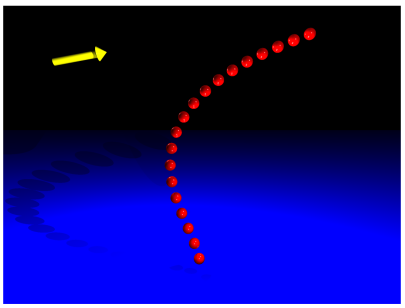

Diploma Thesis
Group of Dr. Holger Stark
University of Konstanz, 2005

Contents

Chapter 1

Introduction

Biological organisms on the scale of microns experience a very different hydrodynamic environment from the one we are used to in everyday life. We live in an environment that is dominated by inertia which in a fluid leads to turbulence. At the very low to zero Reynolds number regime, however, which will be shown to apply to the time and size scale of biological microorganisms, inertia is irrelevant and all motion is dominated by friction. As a consequence, concepts like hydrodynamic interactions and the need for non-reciprocal motion for generating propulsion become important. These effects are mostly unknown on the human scale and require a different approach towards the problem how a micro-swimmer achieves locomotion.

Nevertheless, nature has come up with several very successful examples of propulsive machinery. *E. coli* bacteria, for example, move by spinning a helical prothesis. The diameter of the prothesis and the rotary engine are on a molecular, that is on the nanometer scale [1]. The hair-like filaments called flagella that build the tail of *spermatozoa* generate thrust by passing bending waves from head to tail along the filament [5, 26, 36]. Similarly, cilia are whip-like appendages which pump fluid using an asymmetric beating cycle. In the case of motile cells, this transport of fluid also leads to propulsion [5, 29]. Thus, cilia provide ingenious biological solutions to the problems of fluid mixing and transport at low Reynolds numbers. Both the flagella of *spermatozoa* and cilia are inhabited by complicated contraptions on the nano scale to drive their motion. The beating of cilia, for example, relies on the internal structure of an axoneme, which is a cylindrical arrangement of microtubules that slide relative to each other to generate internal stresses. This sliding motion is powered by molecular dynein motors [7].

The goal of this work is not an investigation of the precise functioning of the driving nano mechanisms. Rather, we aim to shed some light on the relevance of the hydrodynamic environment that caused the evolution of these marvelously designed swimming apparatuses in the first place. This requires an understanding of fluid dynamics at low Reynolds number and the role of hydrodynamic interactions in generating motion. An illustrative overview of the peculiarities of locomotion at low Reynolds number has been given in Purcell's famous paper "Life at low Reynolds number" [32]. Along these lines, a general treatment of low Reynolds number hydrodynamics and swimming is presented in chapter 2, whereas a more comprehensive introduction to hydrodynamic interactions is deferred to chapter 3. Furthermore, the physical properties of elastic filaments in a viscous environment need to be outlined. We introduce the so-called *bead-spring model* which serves as model filament for simulating

the motion of cilia and flagella in chapter 4. The relevant forces acting on such a filament, its equation of motion and scaling laws are treated in this chapter to gain a general understanding of its dynamics.

A simulation study concerned with the hydrodynamic and propulsive effects of such slender filaments has been done by Lagomarsino [23]. Yet, the present work goes far beyond to what has been done by Lagomarsino both in terms of consideration of hydrodynamic interactions and also in the modeling of the filaments. Lagomarsino's approach is to apply an artificial force as a boundary condition to one end of a passive filament. This is analogous to the study of the elastohydrodynamic problems of Wiggins *et al.* [38] and thus produces valuable information for comparing simulation data to theoretical predictions. Moreover, it helps in outlining the qualitative applicability of a linearized theory to more realistic regimes of filament motion. However, biological filaments, notably with the exception of the helical flagella of *E. coli*, are both elastic and inherently active. So, any passive approach, while elucidating some physical aspects, will fall short of the concept of real biological swimmers.

The present work tries to do better justice to inherent ciliary activity by adapting a magnetic actuation technique that works on the whole filament rather than just on one end, an approach that has been brought to our attention by the work of R. Dreyfus [11]. Hence, the problem of a complicated internal actuation is circumvented by a relatively simple concept using an external field that applies a torque on the superparamagnetic model filament. This has the additional advantage of being experimentally realisable.

For this reason, our bead-spring model uses superparamagnetic beads and is designed analogously to the artificial filaments produced in the group of J. Bibette in Paris [11, 14]. These consist of superparamagnetic colloids with a diameter of about a micron. The colloids are linked by polymers, such as DNA snippets, that adhere to the specially prepared surfaces of the colloids. The filaments are assembled by preparing a suitable volume fraction of colloids in an aqueous solution that also contains an adequate concentration of polymers. An external magnetic field forces the colloids into an energetically favourable configuration which is a straight chain of aligned dipoles. The colloids do not come into contact, though, since they repel due to surface charges. The polymers then irreversibly link adjacent colloids together by permanent adhesion to the surfaces of the spheres. A theoretical approach of describing the dynamics of these magnetically driven elastic filaments analytically has been done by the group of H. Stone in Harvard [35].

In chapter 5 the model system of the "one-armed swimmer" consisting of a viscous load attached to a flagellar tail is studied, motivated by a recent experimental realisation of the first man-made micro-swimmer by Dreyfus *et al.* [11]. This micro-swimmer is built of a filament of superparamagnetic colloids that is tethered to a red blood cell. The system is actuated by an external time-varying magnetic field. The one-armed swimmer has recently also drawn a good deal of theoretical attention to it [7, 23, 38], so that both experimental data and theoretical predictions exist that can be compared to and enhanced by simulation data.

Furthermore, a second system with a model cilium attached to a wall is taken up in chapter 6. The dynamics of this system is heavily influenced by the complicated effect of hydrodynamic interactions close to a bounding wall. Therefore, we have derived appropriate mobility tensors [2, 3] to include these interactions to a good approximation. We study two ways of generating an asymmetric beating cycle with a magnetic actuation technique. Both are successful in that they show that surrounding fluid is indeed transported along the wall by the beating of the model cilium.

Chapter 2

Swimming at low Reynolds number

Understanding the physics of swimming both on a macroscopic and microscopic scale requires some knowledge about the principles governing the behaviour of fluids. Therefore, it is necessary to give but a short introduction to hydrodynamics before the topic of locomation can be studied on solid grounds.

2.1 Hydrodynamics

Hydrodynamics is concerned with a treatment of fluid motion. In physical terms this means finding a description for the flow, pressure and density fields induced by external forces and stresses. An example for a direct force on a fluid is gravity, whereas stresses are commonly imposed by boundary conditions. These boundary conditions may arise from containing walls in case of finite vessels. However, in comparatively big volumes with suspended colloids interfaces between fluid and particles are more important and the fluid may often be assumed to be unbounded.

While fluids, like all matter, possess a granular structure at the level of atoms, it is neither necessary nor practically possible to treat hydrodynamic phenomena on an atomistic level. Instead a treatment assuming fluids to be a continuous medium has successfully managed to make a wide variety of experimentally proven predictions and is sufficiently exact for the study of colloid dynamics.

2.1.1 Navier-Stokes equation

The *Navier-Stokes equation* governs fluid flow the way classical mechanics is governed by *Newton's second law*, $\mathbf{F} = \frac{\mathrm{d}}{\mathrm{d}t}\mathbf{p}$, where $\mathbf{F}$ is the force and $\mathbf{p}$ the momentum of a body. Indeed, the Navier-Stokes equation is just a generalisation of Newton's equation of motion.

Mass conservation law

In general, the mass density $\rho(\mathbf{r}, t)$ may depend on time and location. Yet, looking at an arbitrary but fixed volume V, the rate of change of molecules inside the volume must be equal to the number of molecules flowing through the boundary of V. Formally, this leads to the same equation of continuity that is also well known in electrodynamics and statistical

mechanics in connection with the conservation of charge and probability, respectively:

$$\frac{\mathrm{d}}{\mathrm{d}t}m(V) = \frac{\mathrm{d}}{\mathrm{d}t}\int\limits_V \rho(\mathbf{r},t)\,\mathrm{d}^3r = -\oint\limits_{\partial V} \rho(\mathbf{r},t)\mathbf{u}(\mathbf{r},t)\cdot\,\mathrm{d}\mathbf{S}\ . \tag{2.1}$$

$\mathrm{d}\mathbf{S}$ is defined as an outward pointing normal vector on the bounding surface. $\mathbf{x}\cdot\mathbf{y}$ denotes the scalar product of the vectors $\mathbf{x}$ and $\mathbf{y}$. Thus, the minus sign accounts for the decrease of mass inside V when particles leave the enclosed volume. Taking the time derivative inside the integral and using Gauss's integral theorem yields:

$$\int\limits_V \left[\frac{\partial}{\partial t}\rho(\mathbf{r},t) + \nabla\cdot\{\rho(\mathbf{r},t)\mathbf{u}(\mathbf{r},t)\}\right]\,\mathrm{d}^3r = 0\ . \tag{2.2}$$

Since this is true for any control volume V, it follows that the integrand must be identically zero. This is what is usually referred to as the *mass conservation law*.

In contrast to ideal gases where volume and pressure are inversely proportional to each other ($pV = nRT$), most fluids and water in particular may be considered to be incompressible to a very good approximation. Hence, the density can be considered a material constant that is spatially independent and does not vary with time. Putting this into equation (2.2) gives:

$$\nabla\cdot\mathbf{u}(\mathbf{r},t) = 0\ , \tag{2.3}$$

an equation which is known as the *incompressibility condition*.

Navier-Stokes equation for incompressible fluids

By applying Newton's equation of motion to a continuous medium with force density $\mathbf{f}$ and momentum density $\rho\mathbf{u}(\mathbf{r},t)$ one obtains

$$\rho\frac{\mathrm{d}}{\mathrm{d}t}\mathbf{u}(\mathbf{r},t) = \mathbf{f}\ , \tag{2.4}$$

where ρ is the constant mass density of the fluid. $\mathbf{r}(t)$ denotes the time dependent position of the volume element and $\mathbf{u} = \frac{\mathrm{d}}{\mathrm{d}t}\mathbf{r}$ is its velocity. The time derivative of the left side of equation (2.4) simply is:

$$\rho\left[\frac{\partial}{\partial t}\mathbf{u}(\mathbf{r},t) + \mathbf{u}(\mathbf{r},t)\cdot\nabla\mathbf{u}(\mathbf{r},t)\right] = \mathbf{f}. \tag{2.5}$$

Unless otherwise stated, a non-capital letter $\mathbf{f}$ always means a force density or a force per unit area rather than a total force on a particle. For the sake of brevity, in this text sometimes just force instead of force density is used. Two different kinds of forces contribute to $\mathbf{f}$:

$$\mathbf{f} = \mathbf{f}^{ext} + \mathbf{f}^{int}\ . \tag{2.6}$$

On the one hand, there may be an external field exerting a force $\mathbf{f}^{ext}$ on the fluid per unit volume, gravity is but one example. On the other hand, there are interactions with the surrounding fluid which are formally expressed in terms of a stress tensor $\boldsymbol{\sigma}(\mathbf{r},t)$. These forces act on the boundary of an arbitrary volume element V and the total force $\mathbf{F}_0$ on V is given by the surface integral

$$\mathbf{F}_0 = \oint\limits_{\partial V} \boldsymbol{\sigma}(\mathbf{r},t)\cdot\,\mathrm{d}\mathbf{S} = \int\limits_V \nabla\cdot\boldsymbol{\sigma}(\mathbf{r},t)\,\mathrm{d}^3r\ , \tag{2.7}$$

where the last equality is obtained with Gauss's integral theorem. Hence, the internal force density $\mathbf{f}^{int}$ is

$$\mathbf{f}^{int} = \nabla \cdot \boldsymbol{\sigma} \ . \tag{2.8}$$

One part of the internal forces stems from pressure gradients. This contribution constitutes the isotropic part of the stress tensor since the pressure has no preferred spatial direction. Therefore, it is always proportional to the unit matrix $\hat{\mathbf{I}}$. If the fluid is static the pressure p acting along the surface normal $\boldsymbol{\sigma} \cdot \mathrm{d}\mathbf{S} = -p\mathrm{d}\mathbf{S}$ is the only contribution to the stress tensor, so that

$$\boldsymbol{\sigma}^{static} = -p\hat{\mathbf{I}} \ . \tag{2.9}$$

It is possible and quite common to put effects of gravity into the pressure profile. Indeed, all conservative force fields can be expressed as gradients of a scalar potential and then lumped together with the pressure. This is the reason why the external force contribution $\mathbf{f}_{ext}$ is often omitted in the following equations (see also reference [22]).

The origin of the second part of the stress tensor is friction within the fluid. The main difference between solids and fluids is that stress in solids is proportional to the amount of deformation whereas fluids have no memory and stress depends on the rate of deformation. An unbounded fluid flowing at a homogeneous constant velocity will experience no internal friction forces. Friction only occurs when neighbouring fluid elements move at different velocities. Consequently, the force contribution will be proportional to spatial derivatives of the fluid flow velocity rather than the velocity itself. The instantaneous rate of deformation is characterized by the rate of strain tensor which is (see reference [22])

$$\mathbf{e} = \frac{1}{2}\left(\nabla\mathbf{u} + (\nabla\mathbf{u})^t\right) - \frac{1}{3}(\nabla \cdot \mathbf{u})\hat{\mathbf{I}} \ , \tag{2.10}$$

the term $\mathbf{a}^t$ denotes the transpose of a matrix $\mathbf{a}$ and $\mathbf{xy}$ is a dyadic product of the vectors $\mathbf{x}$ and $\mathbf{y}$. Fluids with a linear relation between $\boldsymbol{\sigma}$ and $\mathbf{e}$ are called *Newtonian*. Water and most other fluids with a compact molecular structure are Newtonian fluids whereas fluids consisting of long or otherwise complicated molecules often exhibit a more complex behaviour. For a Newtonian fluid $\boldsymbol{\sigma}$ is given by

$$\boldsymbol{\sigma} = -p\hat{\mathbf{I}} + 2\eta\mathbf{e} \ , \tag{2.11}$$

where the (dynamic) viscosity of the fluid has been introduced via the parameter η. For the purpose of the present work only Newtonian fluids that are also isotropic are considered.[1]

Taking the stress tensor[2] and putting all the pieces together yields the Navier-Stokes equation. As has been mentioned above, it is in many cases reasonable to assume incompressibility, i.e $\nabla \cdot \mathbf{u}(\mathbf{r}, t) = 0$. This gives the *Navier-Stokes equation* for incompressible Newtonian fluids:

$$\rho\frac{\partial}{\partial t}\mathbf{u}(\mathbf{r}, t) + \rho\mathbf{u}(\mathbf{r}, t) \cdot \nabla\mathbf{u}(\mathbf{r}, t) = \eta\nabla^2\mathbf{u}(\mathbf{r}, t) - \nabla p(\mathbf{r}, t) + \mathbf{f}_{ext} \ , \tag{2.12}$$

In this continuous treatment of the fluid, the medium is fully characterized by the two material constants η and ρ.

[1] An isotropic fluid is characterized by $\boldsymbol{\sigma} = -p\hat{\mathbf{I}} + \eta(\nabla\mathbf{u} + (\nabla\mathbf{u})^t)$.
[2] A more detailed treatment of internal stresses and the stress tensor is outlined in [10].

2.1.2 Rescaling the Navier-Stokes equation

The Navier-Stokes equation (2.12) consists of different terms which often are of very different order of magnitude. This means that for specific problems some terms can be dropped without losing the physical significance of the equation. In order to better see which terms dominate, we introduce rescaled variables. These will eventually lead to a dimensionless form of the Navier-Stokes equation in which all material parameters appear as prefactors. For a problem with typical linear dimension a and velocity $\mathbf{v}$, it is reasonable to rescale the quantities in the following way:

$$\begin{aligned} \mathbf{u'} &= \mathbf{u}/v \\ \mathbf{r'} &= \mathbf{r}/a \\ t' &= t/\frac{\rho a^2}{\eta} \\ p' &= p/\frac{\eta v}{a} \\ \mathbf{f'}_{ext} &= \mathbf{f}_{ext}/\frac{\eta v}{a^2} \ , \end{aligned}$$

where $\frac{\rho a^2}{\eta}$ is the characteristic time scale of the problem. By using scaled values the Navier-Stokes equation transforms into:

$$\frac{\partial}{\partial t'}\mathbf{u'} + Re\ \mathbf{u'} \cdot \nabla' \mathbf{u'} = \nabla'^2 \mathbf{u'} - \nabla' p' + \mathbf{f'}_{ext} \ , \tag{2.13}$$

where Re is a dimensionless number, the so-called *Reynolds number*, which is equal to:

$$Re = \frac{\rho a v}{\eta}. \tag{2.14}$$

It is obvious that solutions in primed quantities will be identical as long as the dimensionless Reynolds number remains constant. When changing the dimension a of the system, it is necessary to offset that in the Reynolds number by appropriately adjusting either one or all of η, ρ or v. In other words: the rescaled Navier-Stokes equation exhibits a scaling invariance for a given Reynolds number. This is not a surprising behaviour since a fluid has no intrinsic length scale of its own when looked upon as a continuous medium.

2.1.3 Creeping flow equations

The Navier-Stokes equation is nonlinear with respect to $\mathbf{u}$. Dropping the nonlinearity greatly simplifies the differential equation and expands the class of analytically solvable problems. As can be seen from (2.12), this is possible for Reynolds number $Re \ll 1$, since all other terms are by construction approximately of order one as elaborated in [10].

Whether $\rho\frac{\partial}{\partial t}\mathbf{u}$ needs to be retained depends on the time scale of the problem. This is further investigated in section 2.1.4, where we show that for motion on the Brownian time scale $\tau_D \gg \frac{\rho a^2}{\eta} \gg \tau_{solvent}$ and the flow field may be safely assumed to be stationary. This reduces equation (2.12) to:

$$\begin{aligned} \nabla p(\mathbf{r},t) - \eta \nabla^2 \mathbf{u}(\mathbf{r},t) &= \mathbf{f}_{ext}(\mathbf{r}) \\ \nabla \cdot \mathbf{u}(\mathbf{r},t) &= 0 \ . \end{aligned} \tag{2.15}$$

The first equation is known as the *Stokes equation* and both equations together are called *creeping flow equations*. We note that they do not contain any inertial effects of the fluid flow and that they are linear in the fluid velocity $\mathbf{u}$.

2.1.4 Hydrodynamic time scales

A suspended particle in a fluid experiences random kicks from solvent molecules leading to a motion of the particle that is opposed by a friction force $\mathbf{F}^{fricf}(\mathbf{v})$. The remaining effects of the kicks are then described by $\langle \mathbf{F}(t) \rangle = 0$, as must be the case since the kicks are entirely random and no direction is preferred.

As the simplest possible approach, the friction force is directly proportional to the velocity

$$\mathbf{F}^{fricf} = -\gamma \mathbf{v} = -\gamma \frac{\mathbf{p}}{M} ,$$

where γ is the constant of proportionality and is called friction coefficient. For a perfect sphere it is given by the Stokes factor $\gamma = 6\pi\eta a$, as we will show in section 3.3. Putting both contributions into Newton's equation of motion, one obtains the so-called *Langevin equation* due to the statistical nature of $\mathbf{F}(t)$:

$$\frac{\mathrm{d}}{\mathrm{d}t}\mathbf{p} = -\gamma \frac{\mathbf{p}}{M} + \mathbf{F}(t) \quad \text{with} \quad \langle \mathbf{F}(t) \rangle = 0 . \tag{2.16}$$

A more detailed study of this equation is performed in [10]. The solution indicates different aspects of motion for different time scales. In the case of colloids, whose size is on the micrometre scale:

$$10^{-14}\mathrm{s} \approx \tau_{solvent} \ll 10^{-9}\mathrm{s} \approx \frac{M}{\gamma} \ll \tau_D \tag{2.17}$$

The quotient $\frac{M}{\gamma}$ describes the decay of inertial effects in the motion of the particle. This is easily seen by setting $\mathbf{F}(t) = 0$. The solution to equation (2.16) is then given by

$$\mathbf{p} = \mathbf{p}_0 e^{-\frac{\gamma}{M}t} ,$$

corresponding to a momentum relaxation within a characteristic time interval of $\tau = \frac{M}{\gamma}$. To summarize, there is

- ballistic motion for $t \ll M/\gamma$; the positional displacement is proportional to t,
- diffusive motion on the Brownian time scale with $t \gg M/\gamma$. The position coordinates changes proportional to $\sqrt{t}$.

There is also an intermediate regime on the Fokker-Planck time scale $t \approx M/\gamma$. On that time scale, it is necessary to resolve the time dependence in the creeping flow equation. However, this regime is of no relevance here.

The time scale for momentum relaxation is not the only important time scale in hydrodynamics. The propagation velocity of flow fields is of particular interest when looking at hydrodynamic interactions that occur when several particles are in a state of motion. The motion of each particle is then influenced by the flow fields generated by all other particles. This makes hydrodynamic interactions a very difficult problem to solve that will be addressed in detail in chapter 3. At the moment, consider a single moving particle. Its motion can be viewed as a disturbance that produces a flow field in an otherwise quiescent fluid. There are

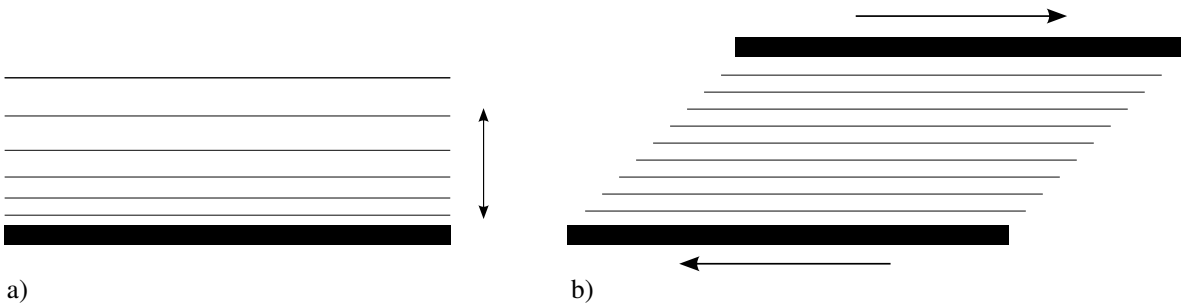

Fig. 2.1: **a**) Pressure waves by an orthogonal movement of a boundary area. **b**) Shear waves by sliding of two surfaces relative to each other.

two different kinds of disturbances to be distinguished: sound or pressure waves and shear waves. Explicitly solving the Navier-Stokes equation for both kinds gives an estimate for the velocities of propagation. An analysis in [10] comes to the conclusion that is fully justified to use the stationary creeping flow equations for all processes happening on Brownian time and length scale, i.e. the flow field can be assumed to be instantaneously present throughout the fluid.

This is the end of the short interlude into hydrodynamics and only the very basics have been treated. Some further insight into the fascinating world of hydrodynamic phenomena will be given later with the treatment of hydrodynamic interactions. For the time being, though, the groundwork for a closer look at the nature of locomation of microorganisms has been laid.

2.2 Locomotion at low Reynolds number

Locomotion on a microscopic scale at low Reynolds number is a very different process than in the macroscopic world. The difference in the swimming strategies of fish and of bacteria has been first investigated by Sir Geoffrey Taylor [36] in 1951 and later in a famous and illustrative article *Life at low Reynolds number* by Purcell in 1977 [32]. This chapter tries to give an introduction and short overview over the peculiarities of locomotion at low Reynolds number. As the field has recently become more and more comprehensive, not all details can be explored at full depth but a focus on topics in some way related to the present work needs to be set.

2.2.1 Physical meaning of the Reynolds number

Many microorganisms, like e.g. *E. coli* bacteria, fulfill the requirements for very low Reynolds numbers. According to the preceding section, their interaction with the surrrounding fluid can then be described well by the creeping flow equations, that approximate the Navier-Stokes equation for Reynolds numbers much smaller than one. In this context, a closer look at the Reynolds number is helpful to better understand the physics at work in such an environment.

The Reynolds number $Re = \frac{\rho a v}{\eta}$ that was introduced in section 2.1.2 in a rather formal way in the derivation of a scaling invariance of the Navier-Stokes equation is quite a tangible

quantity as it describes the ratio between inertial to viscous forces

$$Re = \frac{\text{forces in fluid due to inertia}}{\text{forces due to friction}} = \frac{\rho v^2/a}{\eta v/a^2} = \frac{\rho v a}{\eta}$$

So, a small Reynolds number corresponds to an overdamped system while processes at large Reynolds numbers are dominated by inertia. The Reynolds number depends on the two material parameters ρ and η that fully characterize an isotropic, incompressible Newtonian fluid. Both have no inherent length scale of their own. Additionally, Re depends on the size a and a typical velocity v of the problem under consideration. Now, since $\mathbf{v} \sim \mathbf{f}$[3], the Reynolds number also depends on the forces at work. A macroscopic body can experience Stokes flow if subjected to small enough forces. But what is small enough?

Consider the quotient of the squared viscosity and the density of a fluid,

$$\frac{\eta^2}{\rho} = |\mathbf{f}_{crit}| \ ,$$

with the dimension of a force. Forces much bigger than this critical force $|\mathbf{f}| \gg |\mathbf{f}_{crit}|$ invariably lead to turbulences while much smaller forces $|\mathbf{f}| \ll |\mathbf{f}_{crit}|$ ensure a pure laminar and viscous flow. The argument is taken to more detail in [29], where it is especially shown that $|\mathbf{f}| \ll |\mathbf{f}_{crit}|$ is equivalent to Reynolds numbers much smaller than one. Table 2.1 shows some typical Reynolds numbers ranging from the macroscopic to the very microscopic regime.

Just a few words on the negligibility of momentum relaxation in the Navier-Stokes equation at low Reynolds number. For a particle on the micron scale, like e.g. *E. coli* bacteria ($a \approx 3$ μm), with a typical velocity of about $v \approx 30$ $\mu m/s$ the total way travelled after the pushing force has stopped can be easily estimated:

$$\begin{aligned} \tau &= \frac{M}{\gamma} = \frac{\rho a^3}{6\pi\eta a} \approx 10^{-6} \text{ s} \ , \\ \Delta x &= v\,\tau \approx 0.1 \text{ Å} \ . \end{aligned}$$

So, the coasting distance Δx is roughly of order 0.1 Å in a time interval of scarcely a microsecond. As this distance is many orders of magnitude smaller than the size of the particle, this constitutes an impressive argument for the irrelevance of inertia in the motion of microorganisms.

Swimmer	**Approximate size of swimmer**	**Reynolds number**
Dolphin	3 m	10^7
Human swimmer	2 m	$10^4 - 10^5$
Jellyfish	20 cm	10^3
Goldfish	5 cm	10^2
Plankton	1 mm	10
Microorganism	1 μm	$10^{-5} - 10^{-4}$

Tab. 2.1: Some examples for typical Reynolds numbers of various swimmers in water. The viscosity of water is $\eta \approx 10^{-3}$ kg/(ms). Typical swimming velocities are used.

[3] In turbulent flow the relation may not be linear, but $\mathbf{v} = \mathbf{v}(\mathbf{f})$ still holds.

2.2.2 Time reversal in hydrodynamics

The key difference between Navier-Stokes equation and the creeping flow equations is that of turbulent versus laminar flow. In laminar flow, all fluid motion is just that of sliding layers which can be slided back without a loss of order or structure. Mathematically, this is a consequence of the time-reversal symmetry of the Stokes equation. To get the terms straight, let us begin quite generally with the time reversal symmetry of physical equations.

As an illustrative example of time-reversal invariance, consider a movie of an object being thrown up into the air decelerated by gravity. The movie stops at the point at which the object stands still just before it changes direction and falls down. Then watch the same movie backwards and it looks as if the object was dropped in midair and is accelerated by the same force of gravity. Both cases make perfect (physical) sense.

Newton's equation of motion,

$$m\frac{\mathrm{d}^2\mathbf{x}}{\mathrm{d}t^2} = \mathbf{F}(\mathbf{x}) = -\nabla U \ ,$$

is an example for time-reversal invariance; let $\mathbf{x}(t)$ be an arbitrary solution of it, then $\mathbf{x}(-t)$ also solves the equation since the force, as the negative gradient of a conservative potential U, does not change sign.

Not all equations have this property. The Navier-Stokes equation and the diffusion equation $\frac{\partial}{\partial t}c(\mathbf{x},t) - D\nabla^2 c(\mathbf{x},t) = 0$, for instance, exhibit no time-reversal symmetry. In the case of the Navier-Stokes equation the friction term $\eta\nabla^2\mathbf{u}$ is not time-reversal invariant.

When the inertial term in the Navier-Stokes equation (2.12) can be neglected, the flow field, as a solution of the Stokes equation (2.15), does not explicitly depend on time. Due to the structure of the Stokes equation a solution of it remains a solution of the Stokes equation when both the time variable and also the external forces are reversed. However, the original and the time-reversed solutions need not be the same in general.

While time irreversibility is, generally speaking, connected with the dissipation of energy or an increase of entropy, this does not mean that no energy is dissipated in the creeping flow equations. This is to do with the fact that in order to retrace the trajectory of a particle, it is necessary not only to reverse the time variable but also to flip the sign of the force responsible for the motion: $\mathbf{x}(t) \to \mathbf{x}(-t)$, $\mathbf{f}(t) \to -\mathbf{f}(-t)$, in contrast to solutions of Newton's equation of motion.

But the lack of an explicit time dependence gives rise to another interesting aspect of the motion of a particle in Stokes flow: the energy that is dissipated while transversing a given trajectory from A to B does not depend on the time taken. On the contrary, reversing the same path back from B to A at an arbitrary pace not only has the same energetic cost associated with it, but will also restore the initial state of its surroundings by sliding all layers of fluid back to their initial position. In this respect, all paths $\mathbf{r}(s,t)$ from A to B (or from B to A) along the same trajectory are equivalent, independent of how long they take.

2.2.3 Swimming strategies at low Reynolds number

How is locomotion in a highly viscous fluid achieved? The only thing an aspirant swimmer can do is to deform its body in a way that is propulsory in effect. The deformation should be of a periodic nature since a single swimming stroke is not going to take it very far. Finding a suitable periodic deformation is not as easy as it might seem because many deformations are

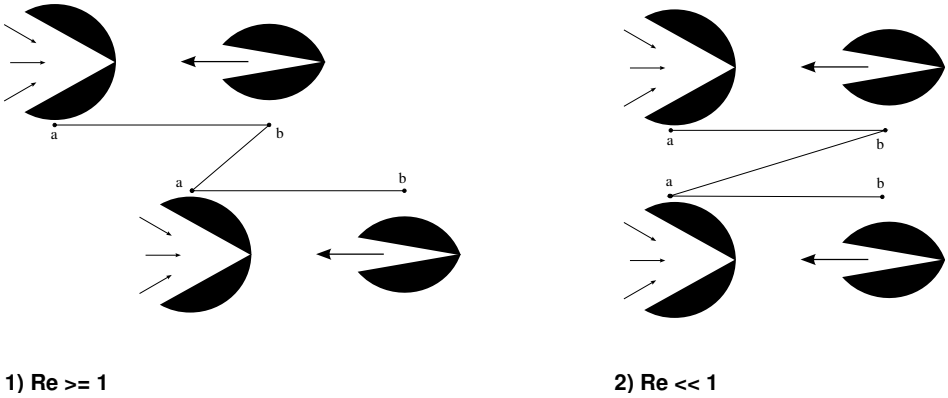

Fig. 2.2: Purcell's scallop theorem: repetition of the two step process of a) sucking in water slowly and b) squirting it out fast leads to net movement on a macroscopic scale as is demonstrated in part 1). It does not work, however, at a small Reynolds number since the cycle is reciprocal as is illustrated in part 2).

reciprocal and therefore do not lead to net motion per cycle, as the following argument will show.

A cyclic reciprocal motion is a motion that looks the same on time reversal $t \to -t$. Yet, reversing the time variable also entails a reversal of the swimming velocity and the forces exerted on the fluid. Remember that any solution of the Stokes equation remains a solution on time-reversal (if the forces are also reversed). What happens on time-reversal for a cyclic reciprocal motion is the following: Since the motion itself is not changed, the solution to the Stokes equation also needs to be time-reversal invariant meaning that the resulting flow field does not change either. Yet, the swimming direction is reversed. However, this is a contradiction because any swimming is connected to a directed flow field. Consequently, a full cycle of reciprocal motion cannot lead to locomotion!

The implications of Stokes flow with respect to locomotion are summed up very well in Purcell's so-called *scallop theorem*. On a macroscopic scale where inertia is important, moving a stiff oar through the fluid alternately, say, slowly leftwards and fast rightwards is a perfectly successful way of generating propulsion. Similarly, the scallop sea-shell moves by performing a periodic two-step process. First it slowly opens its shell, filling the interior space with surrounding water. In the second step of the cycle, the shell closes much faster generating a net thrust and then drifting by inertia, see figure 2.2. This is a special case of what most swimming mechanisms in everyday life make use of, namely that of drifting by inertia.

At small Reynolds numbers, $Re \ll 1$, however, this method of propulsion no longer works simply because the deformation of the scallop's body shape is reciprocal. Alternately performing half a stroke fast and the other half slowly with rigid paddles does not help. The concept of doing something fast versus slow is of no relevance in Stokes flow. A low Reynolds number swimmer needs to find a way to make its propulsory motion non-reciprocal. There are numerous ways of doing this. A simple way is using a flexible oar instead of a stiff one [32]. Other possibilities include the turning of helical objects, "cork-skrews", as propellers [36, 34] or a periodical change of the swimmer's body shape to have time-dependent friction coefficients. Travelling waves along filaments as used by *spermatozoa* are not reciprocal either and entail the desired effect as well.

The lesson from the scallop theorem is that one degree of mechanical freedom is not enough

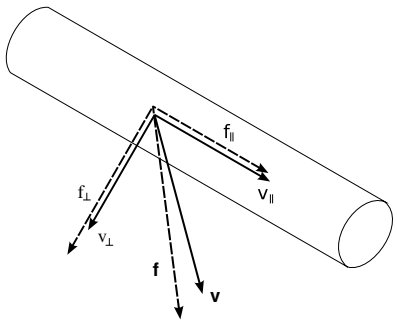

Fig. 2.3: Dragging of a thin rod with velocity $\mathbf{v}$ at low Reynolds number. The force required for the motion is $\mathbf{f}$ which is the resultant from $f_\perp$ and $f_\parallel$. These are linearly related by the friction coefficients to the components of $\mathbf{v}$ parallel and orthogonal to the rod's axis. Both velocity components are shown at the same length, but the resulting components of $\mathbf{f}$ are different, meaning $\mathbf{f}$ and $\mathbf{v}$ cannot be parallel.

for net motion at a low Reynolds number. Purcell has invented a hypothetical swimmer with two degrees of freedom which is the minimum necessary for periodic non-reciprocal deformations. Another micro-swimmer consisting of three beads with variable-length linkers aligned on a straight line was devised by Najafi and Golestanian [28]. It uses a clever sequence of linker extensions and contractions to achieve net motion.

2.2.4 Efficiency of propulsion

Due to the linearity of the creeping flow equation, the relation between force and velocity in Stokes flow is also linear and can be written as a matrix multiplication,

$$\mathbf{F} = \boldsymbol{\zeta} \cdot \dot{\mathbf{r}} \,, \tag{2.18}$$

where $\boldsymbol{\zeta}$ is called the friction matrix. This is all we need to know to work out an upper bound of the efficiency of swimming by means of moving an elastic cylindrical object. A straight rod with diameter d and length L dragged through a fluid has a friction matrix given by [10]

$$\boldsymbol{\zeta} = \begin{pmatrix} \zeta_\parallel & 0 & 0 \\ 0 & \zeta_\perp & 0 \\ 0 & 0 & \zeta_\perp \end{pmatrix} \,,$$

as is immediately clear from the axial symmetry. $\zeta_\parallel$ is the friction coefficient for movement strictly along the long axis of the rod and $\zeta_\perp$ gives the friction for motion exactly perpendicular to it. In the limit of a very long and slender rod, where $d/L \to 0$, the friction coefficient for movement in the direction of the long axis is half as big as for movement normal to it $\zeta_\perp = 2\zeta_\parallel$ [5]. For real cylinders of shorter length with a finite diameter, the relation $\zeta_\parallel < \zeta_\perp < 2\zeta_\parallel$ holds [10].

Imagine to drag a straight cylinder through a fluid for (a), a fixed and straight distance orthogonal to the long axis ("power stroke"), and (b), the same distance back parallel to it ("recovery stroke"), as is illustrated in figure 2.5 (for the sake of simplicity, we will not consider the rotation of 90 degrees required on the turning point).

As in the scallop theorem, the time taken for each way is not important, so both ways may as well be travelled with the same velocity v_0. In order to drag the rod with a velocity

v_0 a force is required that can be calculated from equation (2.18). Going both ways shall be called a cycle. If the force necessary for way (a) and for way (b) do not have the same strength, then the time-averaged force of one cycle does not vanish:

$$\bar{\mathbf{f}} = \int\limits_{(a)+(b)} \mathbf{f}(t)\,\mathrm{d}t \;\neq\; \mathbf{0}\;.$$

A remaining net force $\bar{\mathbf{f}}$ per cycle, however, leads to propulsion. With equation (2.18) it is apparent that (i) propulsion by this mechanism is possible only if $\zeta_\parallel \neq \zeta_\perp$ and (ii) the magnitude of a net propulsive force per cycle only depends on the difference between $\zeta_\perp$ and $\zeta_\parallel$. With the purpose of defining a measure of efficiency, let us look at the time integral over $\mathbf{v}\cdot\mathbf{f}$ which gives the work. Now, the difference between work done during way (a) and way (b) divided by the total work done can be defined as an efficiency measure ξ:

$$\xi = \frac{\int_{(a)} \mathbf{v}\cdot\mathbf{f}\,\mathrm{d}t - \int_{(b)} \mathbf{v}\cdot\mathbf{f}\,\mathrm{d}t}{\int\limits_{(a)+(b)} \mathbf{v}\cdot\mathbf{f}\,\mathrm{d}t}\;. \tag{2.19}$$

Evaluating this expression gives the fraction of the total work done that is transformed into net thrust. It is obvious that this value has an upper bound at $\zeta_\perp = 2\zeta_\parallel$:

$$\xi_{max} = \frac{(f_{(a)} - f_{(b)})v_0 t_0}{(f_{(a)} + f_{(b)})v_0 t_0} = \frac{\zeta_\perp - \zeta_\parallel}{\zeta_\perp + \zeta_\parallel} \leq \frac{1}{3}\;, \tag{2.20}$$

where both the velocity v_0 and the forces $f_{(a)}, f_{(b)}$ are, without loss of generality, assumed to be constant and to have no time dependence. Moving with an efficiency of 33% is the best you can do with a cylinder at low Reynolds number!

A real cilium, as sketched on the left in figure 2.5, cannot move like that since one of its ends is attached to a surface. Going one way parallel and the other orthogonal to the long axis can only be realized to a some extent by an internal bending of the cilium. This also needs to be done in a way that allows for periodic movement. These geometrical restrictions further reduce the percentage of the total work that can be used for propulsion.

Furthermore, the beating of the cilium is powered by a complicated internal driving machinery consisting of molecular motors that do not run at one hundred percent efficiency either. Accordingly, the overall efficiency in terms of chemical fuel (ATP) used compared to the energy dissipated by directed motion of a bacterium is typically at around only 1% [32, 29].

A similar reasoning applies not only to motion through ciliary beating but also to the rotation of rigid helical objects. A short segment of length $\mathrm{d}s$ on such a corkskrew can be considered to be a straight rod and treated as in figure 2.3. For rigid helices, all segments move at the same velocity. Therefore, if the force exerted onto the fluid is strictly parallel to the velocity vector, it cancels out on integration over $\mathrm{d}s$ (see reference [29]). As for ciliary beating, the difference between $\zeta_\perp$ and $\zeta_\parallel$ makes such a mechanism viable.

2.3 Elastohydrodynamics of slender filaments

Many eucaryotic cells use whip-like appendages for generating locomotion. These appendages can be considered to be long and thin elastic rods and will hereafter be referred to as filaments.

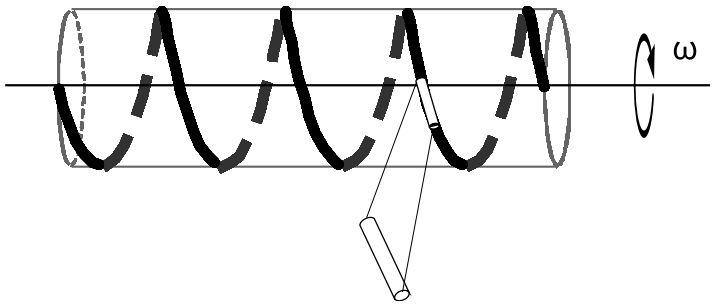

Fig. 2.4: Some bacteria like for instance *E. coli* swim by turning bundles of helical flagella. For better visibility, the schematic helical coil shown here is drawn on the surface of a cylinder. The helix can locally be approximated by segments of straight cylinders. The generation of net thrust is not achieved by "pushing back water" (like it is done with the propeller of a boat) but rather by the local anisotropy of drag coefficients. Compare to figure 2.3.

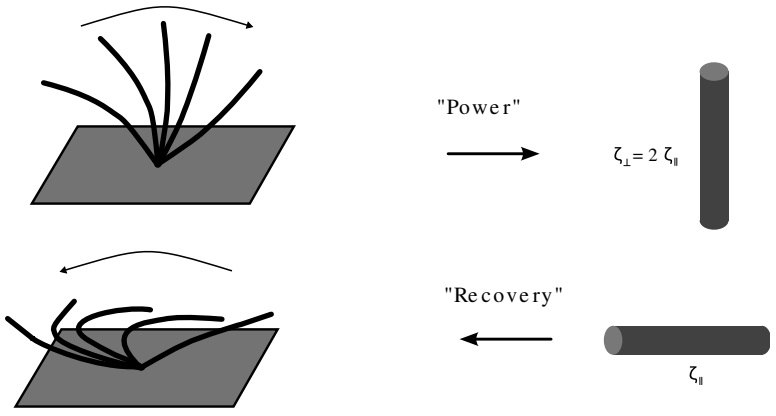

Fig. 2.5: On the left, a schematic of the beating cycle of a cilium is sketched. As an extreme simplification, a stiff rod can be taken to travel one way orthogonal to the axis of symmetry and back parallel to it. This cycle leads to a net transport of fluid parallel to the surface.

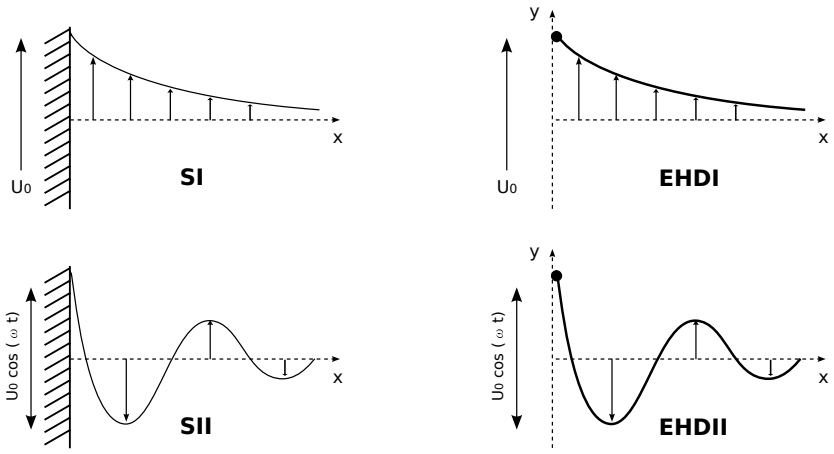

Fig. 2.6: The geometry of the two Stokes problems (SI and SII) of a moving wall and the analogous elastohydrodynamic problems (EHDI and EHDII) as treated by Wiggins *et al.* is sketched. It is visible that all solutions are governed by exponential decay.

When some kind of motion is enforced on one of the ends, the shape of the filament is determined locally by an equilibrium of viscous and elastic forces. A simple model of such an elastic filament in a viscous environment capturing the essentials has been developed by Wiggins, Goldstein *et al.* [38, 39]. Using the same premises but also enforcing inextensibility of the filament to a better approximation, Camalet and Jülicher [7, 6] have studied a more specific problem more closely adapted to the beating of cilia. Following the publications mentioned above, this section will give some insight into basic aspects of overdamped filament dynamics in a highly viscous surrounding.

Looking at a broader picture, the elastohydrodynamic problem of the dynamics of a filament subject to a time-dependent constraint at one of its ends is related to two problems in Stokes flow that were identified and solved by Stokes in 1851:

- SI: impulsively moving of an infinite wall bounding a fluid,
- SII: oscillations of the same wall with frequency ω.

In both cases, the Navier-Stokes equation reduces to a simple, one-dimensional diffusion-type equation

$$\frac{\partial}{\partial t}u = \nu\frac{\partial^2}{\partial x^2}u \tag{2.21}$$

with the kinematic viscosity $\nu = \eta/\rho$. The distinction between SI and SII is in the boundary conditions imposed. In SII, the solutions describe decaying waves that move away from the wall [38]:

$$u(x,t) = u_0 \exp\left(-\frac{x}{l_\nu}\frac{1}{\sqrt{2}}\right)\cos\left(\frac{x}{l_\nu}\frac{1}{\sqrt{2}} - \omega t\right) \ . \tag{2.22}$$

The rate of decay follows an exponential law whose extinction length is called viscous penetration length $l_\nu = (\nu/\omega)^{1/2}$. In analogy to SI and SII the elastohydrodynamic problems have been formulated by Goldstein and Wiggins as follows:

- EHDI: move the end of a filament impulsively,

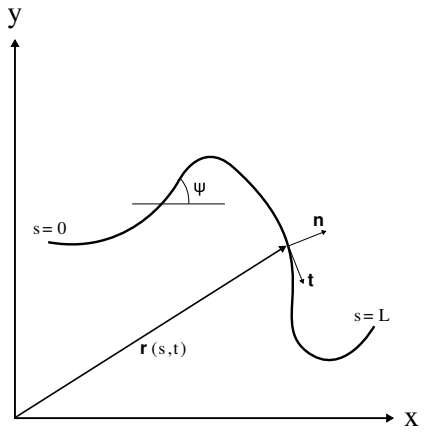

Fig. 2.7: The filament is completely defined in time and space by $\mathbf{r}(s,t)$ which is a function of the arclength parameter s. $\hat{\mathbf{t}}(s)$ and $\hat{\mathbf{n}}(s)$ are the unit tangent and normal, respectively.

- EHDII: oscillate the end of a filament with frequency ω.

Especially EHDII is of interest with respect to a simple mechanism for generating propulsion by periodic motions. For the sake of simplicity, the analysis is carried out in planar geometry. Considering a twodimensional system is not as big a limitation as it might first appear to be because many cilia do indeed move in a well-defined plane.

In order to continue with EDHII, a notation and a Hamiltonian governing the elastic behaviour of the filament need to be established. Imagine a continuous description of an inextensible elastic filament. At any instant, the filament is completely defined by a curve $\mathbf{r}(s,t)$ with s being arclength parameter (see figure 2.7). While a more general description of energies and forces governing thin elastic rods is presented in section 4.1, just the Hamiltonian responsible for the bending elasticity is given here:

$$H = \frac{A}{2} \int_0^L \boldsymbol{\beta}^2 \, \mathrm{d}s \ , \tag{2.23}$$

where $\boldsymbol{\beta}(s) = \frac{\mathrm{d}\hat{\mathbf{t}}(s)}{\mathrm{d}s}$ is the bend vector that describes the local curvature, that is the change of direction of the unit tangent. The restitution force that resists bending and acts on the filament is given by the negative functional derivative of H. In slender-body approximation, the friction of the filament with the surrounding viscous fluid is considered by introducing two different drag coefficients that do not depend on the arclength parameter s. These drag coefficients account for the local friction anisotropy of a slender cylinder. Since they are independent of s, the actual shape of the filament does not enter and the filament is assumed to be locally straight [5]. The equation of motion for such a filament then reads:

$$\dot{\mathbf{r}} = -\left(\frac{1}{\zeta_\parallel} \hat{\mathbf{t}}\hat{\mathbf{t}} + \frac{1}{\zeta_\perp} \hat{\mathbf{n}}\hat{\mathbf{n}} \right) \frac{\delta H}{\delta \mathbf{r}(s)} \ , \tag{2.24}$$

where $\hat{\mathbf{t}}\hat{\mathbf{t}}$ and $\hat{\mathbf{n}}\hat{\mathbf{n}}$ are tensors that act as projectors onto the tangent and the normal direction and $\zeta_\parallel$, $\zeta_\perp$ are the respective friction coefficients. For small planar deviations $y(x)$ from the

completely straight filament oriented parallel to the x-axis, H can be written as

$$H = \frac{A}{2} \int_0^L \left(\frac{\partial^2 y}{\partial x^2} \right)^2 \mathrm{d}x \ ,$$

and the linearized equation of motion assumes the form of a *hyperdiffusion equation* with the hyperdiffusion constant $\tilde{\nu} = \frac{A}{\zeta_\perp}$.

$$\frac{\partial}{\partial t} y(x,t) = -\frac{A}{\zeta_\perp} \frac{\partial^4}{\partial x^4} y(x,t) \ . \tag{2.25}$$

The enforced oscillatory wiggling is considered by the right choice of boundary conditions on one of the ends while the other end remains free.

A more rigorous treatment in [7], where the curve shape is expressed by the angle $\psi(s,t)$ that the local tangent forms with the x-axis, leads to two analytically exact equations for the evolution of the filament shape:

$$\partial_t \psi = \frac{1}{\zeta_\perp}(-A\partial_s^4\psi + \tau\partial_s^2\psi + \partial_s\psi\partial_s\tau) + \frac{1}{\zeta_\parallel}\partial_s\psi(A\partial_s^2\psi\partial_s\psi + \partial_s\tau) \ , \tag{2.26}$$

$$\partial_s^2\tau - \frac{\zeta_\parallel}{\zeta_\perp}(\partial_s\psi)^2\tau = -A\partial_s(\partial_s\psi\partial_s^2\psi) + \frac{\zeta_\parallel}{\zeta_\perp}\partial_s\psi(-A\partial_s^3\psi) \ . \tag{2.27}$$

$\tau(s,t)$ is the tension that ensures the inextensibility constraint. It is the consequence of a Lagrangian tension parameter that needs to be added to the Hamiltonian (2.23). Subject to appropriate boundary conditions, these two equations need to be solved. For small deflections ε, the equations for ψ and τ can be written in a functional expansion about the obvious solution for zero drive $\psi_0(s,t) = 0$, $\tau_0(s,t) = 0$:

$$\psi = \varepsilon\psi_1 + \varepsilon^2\psi_2 + \dots$$
$$\tau = \varepsilon\tau_1 + \varepsilon^2\tau_2 + \dots$$

As a result equations (2.26) and (2.27) decouple up to second order in ε [7, 23] The same hyperdiffusion equation as (2.25) can be derived. It will be used in the following.

As will be seen later, a lot can be gained from rescaling the hyperdiffusion equation to a non-dimensional form. In combination with boundary conditions for EHDII, the solutions describe damped waves moving along the filament in full analogy to SII, as illustrated in figure 2.6. The characteristic length of the hyperdiffusion equation is the extinction length of the exponential decay analogous to the viscous penetration length of SII. As the differential equation is of fourth order, it is given by

$$l_{\tilde{\nu}} = \left(\frac{\tilde{\nu}}{\omega} \right)^{\frac{1}{4}} \ . \tag{2.28}$$

The rescaled length of the filament is an important and fundamental quantity that has been dubbed Sperm number by others [26, 23]:

$$Sp := \frac{L}{l_{\tilde{\nu}}} = \left(\frac{\zeta_\perp \omega L^4}{A} \right)^{\frac{1}{4}} \ . \tag{2.29}$$

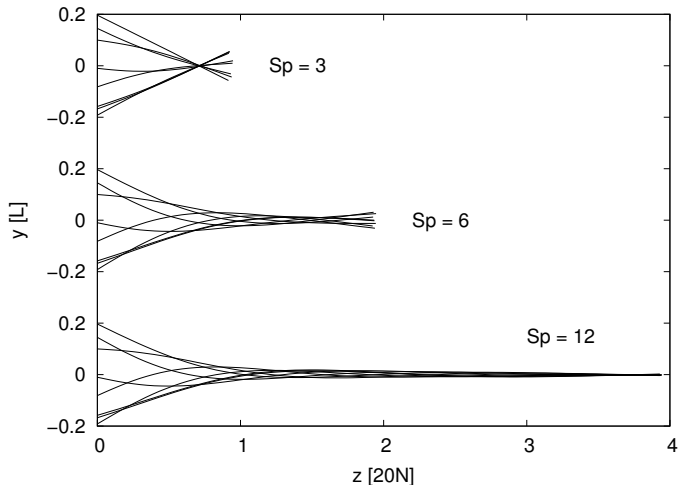

Fig. 2.8: Snapshots of a time series of EHDII for different filament lengths with the same driving frequency. The y-axis corresponds to the wiggling amplitude given in units of the filament length. The x-axis gives the length of the filament as a multiple of 20 beads. The wiggling amplitude of 0.2 is higher than used in EHDII, but this does not modify the qualitative behaviour as has been shown by Lagomarsino [23]. However, the point about which the rigid filament pivots is not at two thirds of its length but further to the end. The increasing damping of the undulations starting at the left end is clearly visible from top to bottom: at Sperm numbers $Sp \lesssim 3$ the filament pivots like a rigid rod. At about $Sp \approx 6$ a pronounced state of bending is assumed over the entire length of the filament while at $Sp \gtrsim 12$ the wave is heavily damped. The data has obtained from the same simulations that are described in section 4.7.3.

Sp describes the length of the filament scaled by the characteristic distance over which undulations subside. Thus, if $Sp \ll 1$ the filament behaves like a rigid rod with only very small deflections. For $Sp \approx 1$ a pronounced state of bending is expected, while for $Sp \gg 1$ the filament is very "sloppy" and bending only occurs at the ends.[4] If the end is oscillated, as is the case in EHDII, a wave pattern is imposed that will determine the shape of the filament close to the end of excitation, whereas the free end remains at rest. In this way, $l_{\tilde{\nu}}$ somewhat resembles the persistence length $L_p = A/k_BT$, which gives the typical distance over which orientational correlations of the ends of a flexible rod in thermal equilibrium are lost.

After these interesting reflections on the nature of the Sperm number Sp, let us get back to the task of rescaling the hyperdiffusion equation (2.25). Introducing reduced quantities as follows,

$$\tilde{x} = x/L \ , \ \tilde{y} = y/L \ , \ \tau = t\frac{A}{\zeta_\perp L^4} \ ,$$

leads to the dimensionless equation

$$\frac{\partial}{\partial\tau}\tilde{y} = -\frac{\partial^4}{\partial\tilde{x}^4}\tilde{y} \ . \tag{2.30}$$

Solving for $\tilde{y}$ under appropriate boundary conditions for EHDII is carried out in detail in [38]. The mathematical details are exhaustive and of no further relevance in the present

[4] In practice, the filament will behave similar to a rigid rod up to $Sp \lesssim 3$ due to the small pre-factor of the contribution of fourth order in Sp in equation (2.32). Pronounced bending then occurs at around $Sp \approx 6$. See figure 2.8.

work. Hence, let it suffice to give the solution straightaway:

$$\frac{y}{y_0} = \frac{1}{2}\left[e^{-\alpha\xi}\cos(\beta\xi+\omega t) + e^{-\beta\xi}\cos(\alpha\xi-\omega t)\right] \ , \tag{2.31}$$

where $\alpha = \cos(\pi/8)$, $\beta = \sin(\pi/8)$ and $\xi = x/l_{\tilde{\nu}}$. The leading terms of an expansion of the exact solution in powers of Sp^4 read [39]:

$$\frac{y}{y_0} \cong \left(1-\frac{3}{2}\tilde{x}\right)\cos(\omega t) + \frac{Sp^4}{1680}[16\tilde{x} - 70(\tilde{x}^3-\tilde{x}^4) - 21\tilde{x}^5] + O(Sp^8) \ . \tag{2.32}$$

Up to zeroth order in Sp the filament is nothing but a rigid rod pivoting about the point two-thirds down its length. At this point, wiggling does not elude the scallop theorem and the motion is fully reciprocal. However, the time-reversal invariance is broken with flexible corrections of fourth order in Sp. The question of interest is, of course, how the non-reciprocal motion of the filament can be related to some kind of propulsion. For this purpose, the time-averaged force exerted on the fluid by the filament is calculated ([39])

$$\overline{\mathrm{F}} = \frac{1}{2}y_0^2\zeta_\perp|\omega|Y(Sp) \ , \tag{2.33}$$

where $Y(Sp)$ is a scaling function that only depends on Sp and that can be calculated exactly; the curve $Y(Sp)$ is shown in figure 2.9. Wiggins *et al.* refer to $\overline{\mathrm{F}}$ as the propulsive force of the system and also derive an efficiency measure based on it. It is interesting that both $Y(Sp)$ (see figure 2.9) and also the efficiency curve (not shown) have a distinct maximum at around $Sp \approx 4$, which seems to be the optimal trade-off between friction and elasticity for generating thrust.

Nonetheless, as Lagomarsino has pointed out, equation (2.33) can, in fact, not be directly interpreted as a measure for a propulsive effect or a swimming velocity since it only contains the transverse friction coefficient. No swimming should be possible for equal friction coefficients $\zeta_\perp = \zeta_\parallel$, a fact that is also shown by Lagomarsino with formal arguments [23]. Instead, Lagomarsino has used a different approach from Jülicher *et al.* [6] to derive the expression

$$v = y_0^2\left(1-\frac{\zeta_\perp}{\zeta_\parallel}\right)\frac{\omega}{4\sqrt{2}L}Y(Sp) \tag{2.34}$$

that correctly predicts no swimming for $Sp = 0$, i.e. when the motion is reciprocal, as well as for $\zeta_\perp = \zeta_\parallel$. The direction of swimming is opposite to the direction of the waves propagating along the filament.[5]

In Lagomarsino's simulation study [23], the predictions for the swimming velocity as a function of Sp are compared with simulation results and a perfect agreement for the small amplitude limit is found. The plateau for large Sp in figure 2.9 is also confirmed in this limit. This seems somewhat odd at first sight, since it predicts no punishment for "infinitely sloppy" filaments. However, for larger, more realistic angular deviations, the simulations show a good qualitative agreement in the lower Sp region and a fast drop of the plateau, see figure 2.10. Interestingly, the distinct maximum in swimming velocity is a feature also present for large amplitudes at roughly the same value of Sp.

[5]The change of swimming direction for $\zeta_\perp < \zeta_\parallel$ [see equation (2.34)] does actually occur in nature with the help of a special surface structure (see reference [23]).

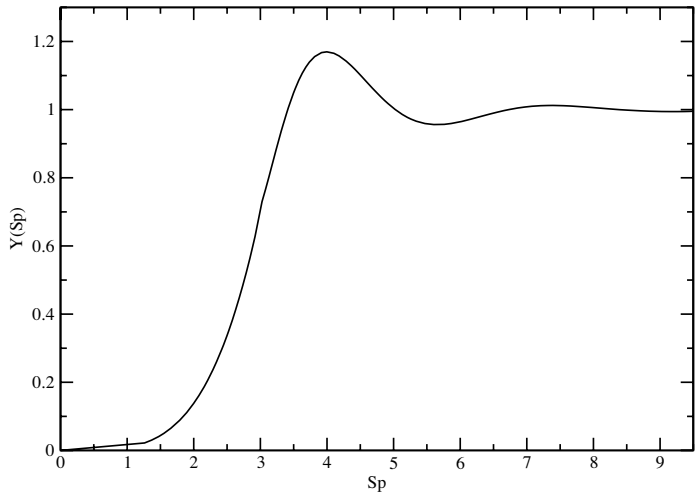

Fig. 2.9: The scaling function $Y(Sp)$ from Wiggins *et al.* that is related to the effect of propulsion of a wiggling filament. The curve can be calculated exactly. The plot is taken from the dissertation thesis of Lagomarsino [23].

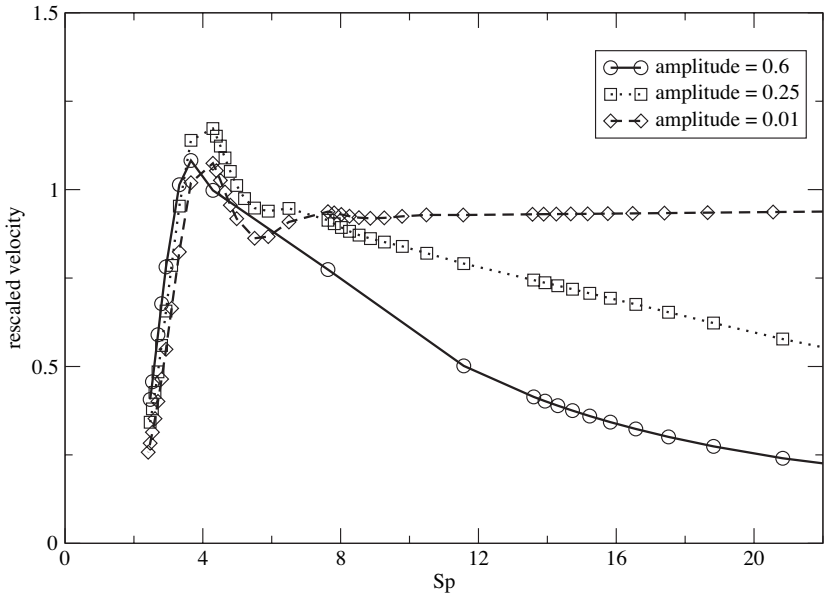

Fig. 2.10: Another plot from Lagomarsino [23]: the rescaled swimming velocity of a simulated filament is shown against the Sperm number for different wiggling amplitudes. The amplitudes are given in units of the overall filament length, while the velocity is plotted in units of the amplitude length per cycle. Of interest is the fact that a well-pronounced maximum exists for all amplitudes at roughly the same value of Sp.

Chapter 3

Hydrodynamic Interactions

3.1 Introduction to hydrodynamic interactions

Particles immersed in a fluid experience so-called *hydrodynamic interactions* besides direct interactions of e.g. electrostatic or magnetic nature. This is simply due to the fact that every moving particle induces a flow field around itself which propagates through the solvent instantaneously when treated by the Stokes equation as in the case of Brownian particles. When this flow field encounters other particles it affects their motion as well.

Why is this not easily observed in everyday life in watery suspensions? Well, hydrodynamic interactions are particularly relevant for small Reynolds numbers. On a macrospopic scale, this effect gets subdued by inertia and turbulences in the fluid flow but on the colloidal length scale it is a long-range interaction to be reckoned with.

Of course, since every particle's motion now depends on the positions, forces acting on and states of rotation of all other particles, evaluating a particle's trajectory now involves solving a system of coupled differential equations constituting a complicated N-body problem.

Often one is not explicitly interested in the flow field itself but rather in the effect of the viscous environment on the motion of immersed particles. In these cases the calculation of mobility relations connecting the total driving forces on the particles and the resultant velocities is the real aim. This is what the following sections will be primarily about.

3.1.1 System of equations of motion

Due to friction, a particle experiencing a force in a solvent does not attain infinitely high velocities but reaches a terminal velocity where the pushing and dragging forces are exactly opposite and balance. For low Reynolds numbers, dominated by friction whereas inertia is irrelevant, the (terminal) velocity is reached instantaneously and is at any time directly proportional to the force $\dot{\mathbf{r}} \sim \mathbf{F}$. The constant of proportionality is a 3×3 matrix that depends on the shape of the particle and is called the mobility tensor. The equation of motion for a single particle in a highly viscous environment then is:

$$\mathbf{v} = \boldsymbol{\mu} \cdot \mathbf{F} \ . \tag{3.1}$$

Occurring in between a matrix and a vector the symbol "$\cdot$" denotes a matrix multiplication. However, when the dot connects two vectorial quantities $\mathbf{x}$ and $\mathbf{y}$, it is meant to express the scalar product $\mathbf{x}^t \cdot \mathbf{y}$ (where $\mathbf{x}^t$ is the transpose of $\mathbf{x}$) rather than the dyadic product $\mathbf{x} \cdot \mathbf{y}^t$ which we write without a dot $\mathbf{xy}$.

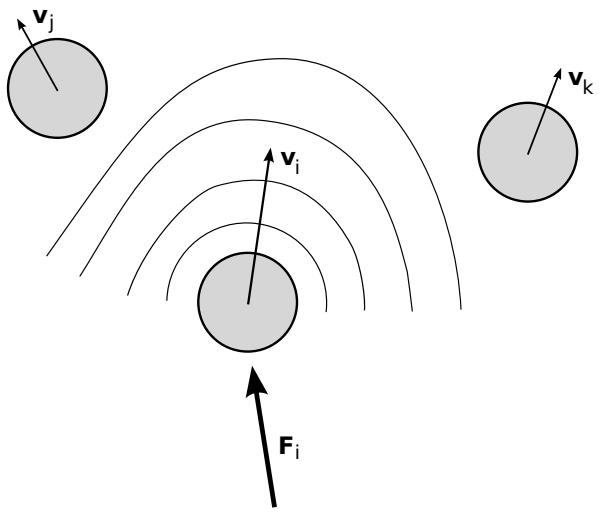

Fig. 3.1: A force acting on one particle leads to a velocity of that particle. This entails a disturbance in the fluid that induces a flow field hitting other particles and affecting their motion. This is called hydrodynamic interaction.

Let us now look at a system of N particles immersed in a fluid. As the creeping flow equations (2.15) are linear, hydrodynamic interactions also lead to linear relations between the velocity of one particle i and the flow field induced by a force pushing particle j. Linear relations can be written as matrix multiplications. Taking into account all possible combinations of translational and also rotational coupling, we obtain:

$$\mathbf{v}_i = \sum_{j=1}^{N} (\boldsymbol{\mu}_{ij}^{tt} \cdot \mathbf{F}_j + \boldsymbol{\mu}_{ij}^{tr} \cdot \mathbf{T}_j) \ , \tag{3.2}$$

$$\boldsymbol{\omega}_i = \sum_{j=1}^{N} (\boldsymbol{\mu}_{ij}^{rt} \cdot \mathbf{F}_j + \boldsymbol{\mu}_{ij}^{rr} \cdot \mathbf{T}_j) \ , \tag{3.3}$$

here $\mathbf{v}_i$ is the velocity of particle i, $\boldsymbol{\omega}_i$ its angular frequency around an axis $\hat{\boldsymbol{\omega}}_i$, $\mathbf{F}_j$ the total external force exerted on particle j and $\mathbf{T}_j$ the torque on the j-th particle. The 3×3 matrices $\boldsymbol{\mu}_{ij}^{ab}$, the mobilities, contain the full spatial configuration of the whole system, i.e. are a function of $3N$ particle coordinates.[1]

The four different types of mobility matrices treat the different possibilities of coupling between translation and rotation. Here, the following notation has been adapted:

- $\boldsymbol{\mu}_{ij}^{tt}$ translational - translational coupling
- $\boldsymbol{\mu}_{ij}^{rr}$ rotational - rotational coupling
- $\boldsymbol{\mu}_{ij}^{tr}$ translational - rotational coupling
- $\boldsymbol{\mu}_{ij}^{rt}$ rotational - translational coupling

[1] If the particles are non-sperical, more than $3N$ particle coordinates are required as the rotational orientation of each particle also becomes important.

The same correlation can also be written in a more compact form as a single matrix multiplication using the so-called *grand mobility matrix*[2]:

$$\mathbf{V} = \mathbf{M} \cdot \mathbf{F} \ . \tag{3.4}$$

$\mathbf{V}$ is a generalised vector for the velocities and rotational speeds of all N particles under consideration. $\mathbf{F}$ is the corresponding generalised force vector and contains all forces and torques acting on all particles and $\mathbf{M}$ is the mobility matrix. Writing out the vectorial components, one obtains:

$$\begin{pmatrix} \mathbf{v}_1 \\ \mathbf{v}_2 \\ \vdots \\ \mathbf{v}_n \\ \boldsymbol{\omega}_1 \\ \vdots \\ \boldsymbol{\omega}_n \end{pmatrix} = \begin{pmatrix} \boldsymbol{\mu}_{11}^{tt} & \boldsymbol{\mu}_{12}^{tt} & \cdots & \boldsymbol{\mu}_{1n}^{tt} & \boldsymbol{\mu}_{11}^{tr} & \cdots & \boldsymbol{\mu}_{1n}^{tr} \\ \boldsymbol{\mu}_{21}^{tt} & \boldsymbol{\mu}_{22}^{tt} & & \vdots & \vdots & & \vdots \\ \vdots & & \ddots & \vdots & \vdots & & \vdots \\ \boldsymbol{\mu}_{n1}^{tt} & \boldsymbol{\mu}_{n2}^{tt} & \cdots & \boldsymbol{\mu}_{nn}^{tt} & \boldsymbol{\mu}_{n1}^{tr} & \cdots & \boldsymbol{\mu}_{nn}^{tr} \\ \boldsymbol{\mu}_{11}^{rt} & \boldsymbol{\mu}_{12}^{rt} & \cdots & \boldsymbol{\mu}_{1n}^{rt} & \boldsymbol{\mu}_{11}^{rr} & \cdots & \boldsymbol{\mu}_{1n}^{rr} \\ \vdots & & \ddots & \vdots & \vdots & \ddots & \vdots \\ \boldsymbol{\mu}_{n1}^{rt} & \boldsymbol{\mu}_{n2}^{rt} & \cdots & \boldsymbol{\mu}_{nn}^{rt} & \boldsymbol{\mu}_{n1}^{rr} & \cdots & \boldsymbol{\mu}_{nn}^{rr} \end{pmatrix} \cdot \begin{pmatrix} \mathbf{F}_1 \\ \mathbf{F}_2 \\ \vdots \\ \mathbf{F}_n \\ \mathbf{T}_1 \\ \vdots \\ \mathbf{T}_n \end{pmatrix} \tag{3.5}$$

The $2N \times 2N$ matrix is just a shorthand notation for a matrix which has $6N \times 6N$ components and consists of four different blocks. Each block describes one of the aforementioned combinations of translational and rotational coupling.

Elements on the diagonale are called *self-mobilities* and are just "three-dimensional" mobility coefficients. They satisfy the direct response in terms of a particle's motion when an external force or a torque is applied. Moreover, if no other particles are present or nearby, the self-mobilities dominate or in the former case even fully determine the trajectory of the particle. If in addition the particles are spherical, the translational self-mobilities are $\boldsymbol{\mu}_{\alpha\beta}^{tt} = (6\pi\eta a)^{-1}\delta_{\alpha\beta}$, where $\delta_{\alpha\beta}$ is the Kronecker symbol and $6\pi\eta a$ the Stokes friction coefficient (see section 3.3). In all other cases, the self-mobilities possess, in general, three different principal mobilities due to a non-sperical particle shape.

All other elements are called *cross-mobilities*. These are the additional contributions due to hydrodynamic interactions. As all particles interact via their flow fields, a force or a torque acting on particle j will have an influence on the velocity or the state of rotation of particle i.

The leading order contribution for pure translation coupling goes with a/r, so this is a true long-range effect. In contrast, the leading order for rotational coupling is $(a/r)^3$ and subsides over much shorter distances.[3] Hence, in the far field approximation it is often justified to consider only translational coupling. Furthermore, for spherical particles $\mathbf{T}_i = 0$. From here onwards $\boldsymbol{\mu}_{ij}$ will always refer to $\boldsymbol{\mu}_{ij}^{tt}$ unless explicitly stated otherwise.

3.1.2 Properties of the mobility matrix

The mobility matrix is a function of the instantaneous spatial configuration of the whole system. Velocities of the single particles do not enter. There are two ways of writing down a

[2]Sometimes, the matrix with the name grand mobility matrix contains more contributions like a strain rate and and strain coupling terms.

[3]Translational - rotational and rotational - translational coupling have a leading order of $\left(\frac{a}{r}\right)^2$; all these terms can be found in e.g. [33].

linear relation between two vectors, so that

$$\mathbf{V} = \mathbf{M} \cdot \mathbf{F} \ , \tag{3.6}$$

$$\mathbf{F} = \mathbf{R} \cdot \mathbf{V} \ , \tag{3.7}$$

are perfectly equivalent representations of the same circumstance. $\mathbf{R}$ is called the resistence matrix for obvious reasons. It follows, that both $\mathbf{M}$ and $\mathbf{R}$ are inverse to each other:

$$\mathbf{M} \cdot \mathbf{R} = \mathbf{M} \cdot \mathbf{R} = \hat{\mathbf{I}} \ . \tag{3.8}$$

Furthermore, as a consequence of *Lorentz' reciprocal theorem* it can be shown that both $\mathbf{M}$ and $\mathbf{R}$ are symmetric [20] which imposes conditions on the matrices $\boldsymbol{\mu}_{ij}^{ab}$, greatly reducing the number of independent components.

Due to the dissipative nature of energy lost to friction the resistence matrix must be positive definite [33]. This can be seen by looking at the expression that gives the rate of dissipated energy in a viscous environment, $\mathrm{W}^{\mathrm{diss}} = \mathbf{V} \cdot \mathbf{F}$. Substituting $\mathbf{F} = \mathbf{R} \cdot \mathbf{V}$ for the force $\mathbf{F}$ gives:

$$\mathrm{W}^{\mathrm{diss}} = \mathbf{V} \cdot \mathbf{R} \cdot \mathbf{V} > 0 \ . \tag{3.9}$$

Because $\mathrm{W}^{\mathrm{diss}}$ needs to be greater than zero to pay tribute to a dissipative process, where energy is lost not gained, the right-hand side of equation (3.9) is nothing but the definition of the positive definiteness of the friction matrix. This property is retained on inversion, so that $\mathbf{M}$ is also positive definite.

The Einstein-Stokes relation links diffusion and mobility of a single particle: $D_0 = k_B T \mu_0$ [29]. The same relation also holds for the many-body mobility matrix $\mathbf{D}$ which describes the collective diffusion of the particles:

$$\mathbf{D} = k_B T \, \mathbf{M} \qquad , \qquad \mathbf{d}_{ij} = k_B T \, \boldsymbol{\mu}_{ij} \ . \tag{3.10}$$

For the purpose of this work, Brownian motion and diffusion are neither considered nor necessary rendering the distinction between mobilities and diffusion matrices unnecessary.

3.2 Oseen tensor

The creeping flow equations (2.15) are linear. This means a superposition of solutions will give a new solution which is a substantial advantage over the Navier-Stokes equation (2.12) since the mathematical concept of Green's function can be employed.

3.2.1 Green's function for creeping flow equations

As in [10] we consider an external force acting on a single point $\mathbf{r'}$ in the fluid. Mathematically, this is described by a delta distribution:

$$\mathbf{f}_{ext}(\mathbf{r}) = \mathbf{F}_0 \delta(\mathbf{r} - \mathbf{r'}) \ . \tag{3.11}$$

Again making use of the linearity of the creeping flow equations, the fluid flow velocity at an arbitrary point $\mathbf{r}$ in the fluid due to a point force at $\mathbf{r'}$ is linearly related:

$$\mathbf{u}(\mathbf{r}) = \mathbf{T}(\mathbf{r} - \mathbf{r'}) \cdot \mathbf{F}_0 \ . \tag{3.12}$$

$\mathbf{T}$ is the *Oseen tensor*; it connects a point force at one location $\mathbf{r'}$ in the fluid to a resulting fluid flow at another point $\mathbf{r}$. As the choice of origin is of no significance, it follows from translational invariance that $\mathbf{T}$ can only be a function of the difference vector $\mathbf{r'} - \mathbf{r}$. The pressure at $\mathbf{r}$ is related to the a point force at $\mathbf{r'}$ in formally the same way:

$$p(\mathbf{r}) = \mathbf{g}(\mathbf{r} - \mathbf{r'}) \cdot \mathbf{F}_0 \ . \tag{3.13}$$

As has been mentioned before, it is possible to use any superposition of solutions as a new solution to the creeping flow equations. This allows us to treat a continously distributed force density in the following way:

$$\mathbf{u}(\mathbf{r}) = \int \mathbf{T}(\mathbf{r} - \mathbf{r'}) \cdot \mathbf{f}(\mathbf{r'}) \ \mathrm{d}^3 r' \ , \tag{3.14}$$

$$p(\mathbf{r}) = \int \mathbf{g}(\mathbf{r} - \mathbf{r'}) \cdot \mathbf{f}(\mathbf{r'}) \, \mathrm{d}^3 r' \ . \tag{3.15}$$

So, the Oseen tensor and the pressure vector $\mathbf{g}$ are Green's functions of the creeping flow equations. A given problem can now be solved in two equivalent ways. First, the creeping flow equations can be solved directly by finding a fitting description of a three-dimensional flow field that satisfies the boundary conditions. Or secondly, the flow field can be evaluated in the above integral representation by expressing the boundary conditions through an appropriate force density that is exerted on the fluid. Of course, the latter approach presupposes knowledge of Green's function.

3.2.2 The Oseen tensor

The form of Green's function can be either formally derived by Fourier transform or by using the solution for a translating sphere [22] . As all calculations are somewhat lengthy, the result is taken directly from [10]:

$$\mathbf{T}(\mathbf{r}) = \frac{\mathbf{G}(\mathbf{r})}{8\pi\eta} \quad \text{with} \quad \mathbf{G}(\mathbf{r}) = \frac{1}{r}\hat{\mathbf{I}} + \frac{\mathbf{rr}}{r^3} \ . \tag{3.16}$$

It is common to split $\mathbf{T}$ into the factor $(8\pi\eta)^{-1}$ and the purely geometrical part $\mathbf{G}$. Remember that $\mathbf{xx}$ is the dyadic product and evaluates to a matrix with components $x_i x_j$. In contrast, scalar products and matrix multiplications are written as $\mathbf{x} \cdot \mathbf{x}$ throughout this text. A point disturbance in a fluid (see equation 3.12) is sometimes referred to as a *stokeslet* and Green's function as the *Stokes propagator* since it describes the propagation of the flow field induced by a stokeslet to any other location within the medium.

The same calculation in [10] also determines the pressure vector, which is

$$\mathbf{g}(\mathbf{r}) = \frac{1}{4\pi}\frac{\mathbf{r}}{r^3} \ . \tag{3.17}$$

On top of enabling an integral representation for solving the Stokes equation, the Oseen tensor also plays an important role in calculating hydrodynamic interaction mobility matrices insofar as it is the leading term in an expansion of the mobility matrices with respect to inverse distances. The reason for this circumstance simply is that two particles far apart from each other can always be assumed to be point-like.

3.3 Flow past a single sphere

As a first application of the Oseen tensor, the flow initiated by a sphere moving at a steady velocity or being in a state of uniform rotation is considered. In both cases the surface of the sphere moves fluid along and thus creates a flow field. Mathematically, the problem is a complicated boundary-condition problem, solely facilitated by the symmetry of the sphere. The assumption of *stick boundary conditions* or *no-slip boundary conditions* is often adapted and has been proven to deliver excellent results. The fluid is assumed to stick to all surfaces due to attractive interactions between fluid molecules and surface material. Consequently, the boundary condition to be imposed for a sphere translating at velocity $\mathbf{v}$ and rotating with an angular frequency $\mathbf{\Omega}$ is

$$\mathbf{u}(\mathbf{r}) = \mathbf{v} + \mathbf{\Omega} \times (\mathbf{r} - \mathbf{r}_p) \ , \ \mathbf{r} \in \partial V \ , \tag{3.18}$$

where $\mathbf{r}_p$ is the centre and ∂V the surface of the sphere. Furthermore, any disturbance in the fluid may be assumed to decay over large distances and completely to vanish at infinity. Thus,

$$\mathbf{u}(\mathbf{r}) \to 0 \qquad , \qquad r \to \infty \ . \tag{3.19}$$

Now, evaluation of the integrals

$$\mathbf{u}(\mathbf{r}) = \oint_{\partial V} \mathbf{T}(\mathbf{r} - \mathbf{r'}) \cdot \mathbf{f}(\mathbf{r'}) \, \mathrm{d}S' \ , \tag{3.20}$$

$$p(\mathbf{r}) = \oint_{\partial V} \mathbf{g}(\mathbf{r} - \mathbf{r'}) \cdot \mathbf{f}(\mathbf{r'}) \, \mathrm{d}S' \ , \tag{3.21}$$

choosing appropriate surface forces yields the flow field of a single sphere. The calculation is done in [10] for the separate cases of a translating and a rotating sphere. The spherical symmetry turns out to very handy as it can be exploited for performing the integrations over the surfaces. Still, the calculation is a bit lengthy, so that just the results are printed here.

3.3.1 Uniformly translating sphere

A promising ansatz for the force per unit area exerted onto the fluid by a surface element of the sphere of radius a is to choose it proportional to the sphere's velocity,

$$\mathbf{f}(\mathbf{r'}) = \frac{c}{4\pi a^2} \mathbf{v} \ , \tag{3.22}$$

the constant $c = 6\pi\eta a$ needs to be determined by satisfying the boundary condition (3.18) for $\Omega = 0$. The flow field initiated by a uniformly translating sphere in an otherwise quiescent fluid then is:

$$\begin{aligned} \mathbf{u}(\mathbf{r}) = & \left\{ \frac{3}{4} \frac{a}{|\mathbf{r} - \mathbf{r}_p|} \left[\hat{\mathbf{I}} + \frac{(\mathbf{r} - \mathbf{r}_p)(\mathbf{r} - \mathbf{r}_p)}{|\mathbf{r} - \mathbf{r}_p|^2} \right] \right. \\ & \left. + \frac{1}{4} \left(\frac{a}{|\mathbf{r} - \mathbf{r}_p|} \right)^3 \left[\hat{\mathbf{I}} - 3 \frac{(\mathbf{r} - \mathbf{r}_p)(\mathbf{r} - \mathbf{r}_p)}{|\mathbf{r} - \mathbf{r}_p|^2} \right] \right\} \cdot \mathbf{v} \end{aligned} \tag{3.23}$$

Stokes's friction law can be easily derived by calculating the integral

$$\mathbf{F} = \oint_{\partial V} \mathbf{f}(\mathbf{r'}) \, \mathrm{d}S' = \frac{c}{4\pi a^2} \mathbf{v} \, 4\pi a^2 = c\mathbf{v} \ , \tag{3.24}$$

The result is just the wellknown expression that has already been used in earlier sections when the friction coefficent was needed:

$$\mathbf{F} = 6\pi\eta a\mathbf{v} \ . \tag{3.25}$$

3.3.2 Uniformly rotating sphere

The obvious choice for the force per unit area exerted on the fluid by a surface element of the sphere is just that of a force proportional to the velocity of the surface element:

$$\mathbf{f}(\mathbf{r'}) = \frac{c}{4\pi a^2}\boldsymbol{\Omega} \times (\mathbf{r} - \mathbf{r}_p) \ , \tag{3.26}$$

with $c = 8\pi\eta a^3$ being the parameter that needs to be chosen to satisfy the boundary condition (3.18) for $\mathbf{v} = \mathbf{0}$. Substitution into equation (3.20) and evalution of the integral yields the simple expression

$$\mathbf{u}(\mathbf{r}) = \left(\frac{a}{r}\right)^3 \boldsymbol{\Omega} \times (\mathbf{r} - \mathbf{r}_p) \ , \tag{3.27}$$

which just describes cylindrical sliding layers of fluid. Stokes's friction law for rotational motion is found to be [10]:

$$\mathbf{T} = \oint_{\partial V} \mathbf{f}(\mathbf{r'}) \times (\mathbf{r} - \mathbf{r}_p)\, \mathrm{d}S' = 8\pi\eta a^3\boldsymbol{\Omega} \ , \tag{3.28}$$

where $\mathbf{T}$ is the torque on the sphere.

3.3.3 Differential representation of the flow field

It is possible to derive the same results in other ways as is done in many textbooks, e.g. [25, 16, 19]. Solutions to the Stokes equation for given boundary conditions can be shown to be unique [22]. Reversely, when such a solution is found by chance, educated guessing or intuition, then it must be the unique solution.

This is done in [22] by looking at derivatives of the Oseen tensor $\mathbf{T}(\mathbf{r})$. The approach gets its justification in section 3.4. In the case of a translating sphere, the combination $(1 + (a^2/6)\nabla^2)\mathbf{T}(\mathbf{r})$ is considered. Evaluating at $r = a$ gives

$$\left(1 + \frac{a^2}{6}\nabla^2\right)\mathbf{T}(\mathbf{r})\bigg|_{r=a} = \frac{1}{6\pi\eta a}\hat{\mathbf{I}} \ , \tag{3.29}$$

so a flow field satisfying the boundary conditions is immediately obtained by setting

$$\mathbf{u}(\mathbf{r}) = 6\pi\eta a\mathbf{v} \cdot \left(1 + \frac{a^2}{6}\nabla^2\right)\mathbf{T}(\mathbf{r}) \ . \tag{3.30}$$

An expression for the flow field of a uniformly translating sphere can thus be derived in a very straightforward fashion with no need for integrations. In a similar way, the problem of a rotating sphere is tackled in [22].

3.4 Multipole expansion

Like in electrostatics, disturbances in hydrodynamics can be treated with a multipole expansion. At great distances from the surface of a particle $|\mathbf{r}-\mathbf{r'}|/a \gg 1$, it is hard to distinguish between points $\mathbf{r'}$ on the particle surface and an origin $\mathbf{0}$ chosen conveniently inside the particle. Consequently, the approximation $\mathbf{T}(\mathbf{r}-\mathbf{r'}) \approx \mathbf{T}(\mathbf{r})$ is a good one at distances large enough. Then, however, all that remains of equation (3.14) is

$$\mathbf{u}(\mathbf{r}) \sim \mathbf{F} \cdot \mathbf{T}(\mathbf{r}) \ , \tag{3.31}$$

and the particle shape does not enter any more. This is analogous to a point charge in electrostatics. In this approximation of a pointlike particle rotations are irrelevant. Higher order corrections for the flow field close to the particle may be obtained by expanding $\mathbf{T}(\mathbf{r}-\mathbf{r'})$ into a Taylor series in $\mathbf{r'}$ around $\mathbf{r'}=\mathbf{0}$:

$$\mathbf{T}(\mathbf{r}-\mathbf{r'}) = \sum_{n=0}^{\infty} \frac{(-1)^n}{n!} (\mathbf{r'}\cdot\nabla)^n \mathbf{T}(\mathbf{r}) \ . \tag{3.32}$$

The calculation is taken further in [22]. Yet, some facts can be pointed out at this level without going into the details. For an arbitrarily shaped particle many terms of the series are necessary to obtain a good approximation of the flow field near the particle's surface because higher order terms do not necessarily decay fast on distances comparable to the linear dimension of the particle [22].

However, if a particle exhibits a high degree of symmetry, it may be hoped that only a few terms of the series will be different from zero. Remember, in electrostatics the expression for a point charge is analytically correct for problems involving an uniformly charged sphere. Since the Stokes equation is not quite as simple as the Poisson equation, an additional contribution to account for the finite size needs to be added - in the case of a spherical particle this is the quadrupole moment as the second term on the right-hand side of equation (3.30) shows. This is the reason the simple approach in section 3.3.3 works. However, a more rigorous derivation can be found in [13].

3.5 Hydrodynamic interactions on the Oseen level

An approximate solution of the creeping flow equations for two spheres suspended in a quiescent fluid is calculated below. The resulting mobility matrices describe hydrodynamic interactions in leading order. They are sufficient if all particles are far apart from each other and can be considered point-like.

For the sake of simplicity and to obtain analytical expressions, all further investigation of hydrodynamic interactions will be restricted to spherical particles. Whenever the letter a occurs, it denotes the radius of the spheres under consideration. Of course, the employed concepts also work for any other shape but, in general, analytical solutions are not known.

We assume stick-boundary conditions for all spheres:

$$\mathbf{u}(\mathbf{r}) = \mathbf{v}_i + \boldsymbol{\Omega}_i \times (\mathbf{r}-\mathbf{r}_i) \ , \ \mathbf{r} \in \partial V_i \ , \tag{3.33}$$

where $\mathbf{v}_i$ and $\boldsymbol{\Omega}_i$ are the translational and rotational velocity of particle i, respectively. As this is a many body problem the integrals (3.20), (3.21) transform into sums of integrals

ranging over all particle surfaces:

$$\mathbf{u}(\mathbf{r}) = \sum_{j=1}^{N} \oint_{\partial V_j} \mathbf{T}(\mathbf{r}-\mathbf{r'}) \cdot \mathbf{f}_j(\mathbf{r'}) \, \mathrm{d}S' \ , \tag{3.34}$$

$$p(\mathbf{r}) = \sum_{j=1}^{N} \oint_{\partial V_j} \mathbf{g}(\mathbf{r}-\mathbf{r'}) \cdot \mathbf{f}_j(\mathbf{r'}) \, \mathrm{d}S' \ , \tag{3.35}$$

where $\mathbf{f}_j$ is the force per unit area exerted on the fluid by a surface element of particle j. The combined equations (3.34) and (3.33),

$$\mathbf{v}_i + \boldsymbol{\Omega}_i \times (\mathbf{r}-\mathbf{r}_i) = \sum_{j=1}^{N} \oint_{\partial V_j} \mathbf{T}(\mathbf{r}-\mathbf{r'}) \cdot \mathbf{f}_j(\mathbf{r'}) \, \mathrm{d}S' \ , \ \mathbf{r} \in \partial V_i \ , \ j \neq i \ , \tag{3.36}$$

need to be calculated. Up to this point everything is exact. If one considers the approximation $|\mathbf{r}_i - \mathbf{r}_j| \gg 2a$, and therefore $\mathbf{T}(\mathbf{r}-\mathbf{r'}) \approx \mathbf{T}(\mathbf{r}_i - \mathbf{r}_j)$ for $(i \neq j)$, one can immediately write down the (translational) mobility matrices $\boldsymbol{\mu}_{ij}$:

$$\boldsymbol{\mu}_{ii} = \frac{1}{6\pi\eta a}\hat{\mathbf{I}} = \mu_0 \hat{\mathbf{I}} \ , \ \mu_0 = \gamma^{-1} = \frac{1}{6\pi\eta a} \tag{3.37}$$

$$\boldsymbol{\mu}_{ij} = \mathbf{T}(\mathbf{r}_i - \mathbf{r}_j) = \frac{3}{4}\mu_0 \frac{a}{r_{ij}} \left[\hat{\mathbf{I}} + \hat{\mathbf{r}}_{ij}\hat{\mathbf{r}}_{ij}\right] \ , \ i \neq j \ . \tag{3.38}$$

3.6 Faxén theorems

An important question in connection with hydrodynamic interactions is the translational or rotational motion that a body immersed in a fluid does acquire from an existing flow field. This is what Faxén's theorems are about.

Consider a sphere immersed in a fluid with an already existing flow velocity field $\mathbf{u}_0(\mathbf{r})$. We add the homogeneous solution $\mathbf{u}_0(\mathbf{r})$ of the Stokes equation to equation (3.36)

$$\mathbf{v}_p + \boldsymbol{\Omega}_p \times (\mathbf{r}-\mathbf{r}_p) = \mathbf{u}_0(\mathbf{r}) + \oint_{\partial V} \mathbf{T}(\mathbf{r}-\mathbf{r'}) \cdot \mathbf{f}(\mathbf{r'}) \, \mathrm{d}S' \ , \tag{3.39}$$

where $\mathbf{r}_p$ is the centre and ∂V the surface of the sphere. Again, $\mathbf{f}$ is the force per unit area exerted on the fluid by the sphere. Integration over ∂V gives [10]

$$\mathbf{v}_p = \frac{1}{6\pi\eta_0 a}\mathbf{F}_p + \frac{1}{4\pi a^2}\oint_{\partial V} \mathbf{u}_0(\mathbf{r}) \, \mathrm{d}S' \ , \tag{3.40}$$

where $\mathbf{F}_p$ is the drag force of particle p. Due to symmetry the integration over the rotational contribution has vanished. Now, the flow field $\mathbf{u}_0(\mathbf{r})$ is Taylor expanded around the centre of the sphere $\mathbf{r} = \mathbf{r}_p$:

$$\mathbf{u}_0(\mathbf{r}) = \mathbf{u}_0(\mathbf{r}_p) + (\mathbf{r}-\mathbf{r}_p) \cdot \nabla_p \, \mathbf{u}_0(\mathbf{r}_p) + \frac{1}{2}(\mathbf{r}-\mathbf{r}_p)(\mathbf{r}-\mathbf{r}_p) : \nabla_p \nabla_p \, \mathbf{u}_0(\mathbf{r}_p) + \ldots \tag{3.41}$$

Substitution of the Taylor series into equation (3.40) yields with α being a pre-factor:

$$\mathbf{v}_p = \frac{1}{6\pi\eta_0 a}\mathbf{F}_p + \mathbf{u}_0(\mathbf{r}_p) + \frac{1}{6}a^2\nabla_p^2\,\mathbf{u}_0(\mathbf{r}_p) + \nabla_p^2\nabla_p^2[\alpha\mathbf{u}_0(\mathbf{r}_p) + \ldots] \; . \tag{3.42}$$

However, all terms in the square brackets are identically zero since the Stokes equation is biharmonic $\nabla^2\nabla^2\mathbf{u}_0 = 0$. This can be seen by taking the divergence of the creeping flow equations [10]. Hence, all that remains is *Faxén's theorem* for translational motion:

$$\mathbf{v}_p = \frac{1}{6\pi\eta_0 a}\mathbf{F}_p + \mathbf{u}_0(\mathbf{r}_p) + \frac{1}{6}a^2\nabla_p^2\mathbf{u}_0(\mathbf{r}_p) \; , \tag{3.43}$$

and its rotational analogue

$$\boldsymbol{\Omega}_p = \frac{1}{8\pi\eta_0 a^3}\mathbf{T}_p + \frac{1}{2}\nabla_p \times \mathbf{u}_0(\mathbf{r}_p) \; , \tag{3.44}$$

given without derivation. Once again, in case $\mathbf{u}_0(\mathbf{r}) = 0$, Stokes' friction laws are reproduced.

3.7 Rotne-Prager approximation

Imagine two spheres in uniform translational motion in an otherwise quiescent fluid. Without hydrodynamic interactions both move according to Stokes's law $\mathbf{v}_i = \mu_0\mathbf{F}_i$. The velocity field induced by sphere i is given by equation (3.23). The effect of this flow field on the translational motion of particle j is determined by Faxén's theorem (3.43) where $\mathbf{u}_0$ is the field induced by particle i:

$$\mathbf{v}_j = \mu_0\left\{\mathbf{F}_j + \left[1 + \frac{1}{6}\,a^2\nabla_j^2\right]\mathbf{M}(\mathbf{r}_j - \mathbf{r}_i)\cdot\mathbf{F}_i\right\} \; , \tag{3.45}$$

where

$$\mathbf{M}(\mathbf{r}) = \frac{3}{4}\frac{a}{r}\left[\hat{\mathbf{I}} + \frac{\mathbf{r}\mathbf{r}}{r^2}\right] + \frac{1}{4}\left(\frac{a}{r}\right)^3\left[\hat{\mathbf{I}} - 3\frac{\mathbf{r}\mathbf{r}}{r^2}\right] \; . \tag{3.46}$$

A comparison with the definition of the mobility matrices (3.5) with a focus on translational motion identifies the mobility matrices as

$$\boldsymbol{\mu}_{ii} = \mu_0\hat{\mathbf{I}} \tag{3.47}$$

$$\begin{aligned}\boldsymbol{\mu}_{ij} &= \mu_0\left[1 + \frac{1}{6}\,a^2\nabla_i^2\right]\mathbf{M}(\mathbf{r}_i - \mathbf{r}_j) \; , \; i \neq j \\ &= \mu_0\left\{\frac{3}{4}\,\frac{a}{r_{ij}}\left[\hat{\mathbf{I}} + \hat{\mathbf{r}}_{ij}\hat{\mathbf{r}}_{ij}\right] + \frac{1}{2}\left(\frac{a}{r_{ij}}\right)^3\left[\hat{\mathbf{I}} - 3\,\hat{\mathbf{r}}_{ij}\hat{\mathbf{r}}_{ij}\right]\right\} \; ,\end{aligned} \tag{3.48}$$

with $\mathbf{r}_{ij} = \mathbf{r}_i - \mathbf{r}_j$ and $\hat{\mathbf{r}}_{ij} = \mathbf{r}_{ij}/r_{ij}$. Expression (3.48) is generally called *Rotne-Prager matrix* and goes one term further in a series expansion into the inverse distances between two spheres compared to the Oseen matrix. Consequently, hydrodynamic interaction can be more accurately described for spheres closer together. Indeed, the Rotne-Prager matrix is known to be reasonably exact down to distances of roughly three radii between the sphere centres.

3.7.1 Method of reflections

The Rotne-Prager matrix is the first step in an iterative process. Now, one could continue to calculate the flow field of particle j, the so-called first order "reflected flow field". This could be used in Faxén's theorem to get a better approximation of the velocity of particle i. The series can be repeated infinitely and is known as the method of reflections. The more terms of the series are considered, the better the accuracy of the expansion. At small distances or close to contact, it becomes necessary to account for lubrication effects, which is usually done by introducing a new lubrication term.

For more than two particles immersed an optimal approximation will also have to account for three and more body hydrodynamic interaction, which makes the whole procedure a lot more expensive in terms of computational power needed.

In this work, however, interactions on the pairwise additive Rotne-Prager level are sufficient since all particles are kept at distances $r \approx 3a$.

3.7.2 Rotne-Prager matrix for differently sized spheres

There are several ways of generalising the Rotne-Prager cross-mobilities for two spheres with different radii. A possible derivation in a similar way as in the previous section is sketched in [10]. The result is also given in [8].

Jeffrey & Onishi [20] use a development of the methods of reflections that is called twin multipole expansion. By the appropriate choice of coordinate system and some general properties of mobility functions, they manage to find an expression for each mobility tensor that only depends on two scalar functions due to the uni-axial symmetry of a configuration of two spheres. In turn these functions are again written as series expansions that can be taken to an arbitrary level of accuracy. For this approach, the spheres do not have to be of the same size.

A calculation along those lines yields a generalisation of the Rotne-Prager matrix for spheres with unequal radii a_i and a_j:

$$\boldsymbol{\mu}_{ij} = \frac{1}{6\pi\eta r_{ij}} \left\{ \frac{3}{4} \left[\hat{\mathbf{I}} + \hat{\mathbf{r}}_{ij}\hat{\mathbf{r}}_{ij} \right] + \frac{1}{4} \frac{a_i^2 + a_j^2}{r_{ij}^2} \left[\hat{\mathbf{I}} - 3\,\hat{\mathbf{r}}_{ij}\hat{\mathbf{r}}_{ij} \right] \right\} . \tag{3.49}$$

Of course, for spheres of equal size this just reduces to equation (3.48).

3.8 Hydrodynamic interactions close to a wall

The presence of an infinitely extended wall in an otherwise unbounded fluid makes the problem of calculating mobility matrices for spherical particles significantly harder. First of all, the self-mobility is no longer given by the Stokes factor times a unit matrix as e.g. in the Rotne-Prager approximation, since the translational symmetry of the fluid is broken by the wall. For the self-mobility an axial symmetry can still be employed but for interactions between two particles this is not the case and for boundary conditions three different surfaces need to be considered. As we have done so far, we assume no-slip boundary conditions on all surfaces.

Similar to electrostatics, the boundary condition of a vanishing fluid velocity field on an infinitely extended plane can be realised by introducing an appropriate images. Unlike electrostatics, where it suffices to just mirror the charge distribution, the hydrodynamic image

system is more complicated because of the more complicated structure of the Stokes equation when compared to the Poisson equation.

3.8.1 Blake's Green tensor

The image system and the Green function replacing the Oseen tensor in the presence of a bounding wall was first derived by Blake [2]. It turns out that in addition to the mirrored stokeslet point disturbance, also called anti-stokeslet, two other contributions called stresslet or Stokes-doublet and sourcelet are needed,

$$\begin{aligned} \mathbf{G}^{Blake}(\mathbf{r}_i, \mathbf{r}_j) &= \mathbf{G}(\mathbf{r}_i - \mathbf{r}_j) + \mathbf{G}^{im}(\mathbf{r}_i, \mathbf{r}_j) \\ &= \mathbf{G}(\mathbf{r}_i - \mathbf{r}_j) - \mathbf{G}(\mathbf{r}_i - \overline{\mathbf{r}}_j) + \delta\mathbf{G}^{im}(\mathbf{r}_i, \overline{\mathbf{r}}_j) \ , \end{aligned} \tag{3.50}$$

where $\mathbf{r}_j$ is the coordinate vector of the stokeslet and $\overline{\mathbf{r}}_j$ is the position of the image stokeslet:

$$\mathbf{r}_i = (x_i, y_i, z_i) \ ; \ \mathbf{r}_j = (x_j, y_j, z_j) \ ; \ \overline{\mathbf{r}}_j = (x_j, y_j, -z_j) \ .$$

The geometry is also illustrated in figure 3.2. $\mathbf{G}(\mathbf{x})$ is the Oseen tensor (3.16) for a point disturbance. Let h be the height of particle j above the plane and $\mathbf{m}$ the unit normal to the plane along the z-axis, then $\mathbf{r}_j - \overline{\mathbf{r}}_j = 2h\mathbf{m}$. In this notation the additional contribution to the image system $\delta\mathbf{G}^{im}(\mathbf{r}_i, \overline{\mathbf{r}}_j)$ is given by [2, 3]:

$$\begin{aligned} \delta G^{im}_{\alpha\beta}(\mathbf{r}_i, \overline{\mathbf{r}}_j) &= h^2(\delta_{\beta m} - 2\delta_{\beta 3}\delta_{m3})\nabla^2_{\mathbf{r}_j} G_{\alpha m}(\mathbf{r}_i, \overline{\mathbf{r}}_j) \\ &+ 2h(\delta_{\beta m} - 2\delta_{\beta 3}\delta_{m3}) \frac{\partial}{\partial(\overline{\mathbf{r}}_j)_m} G_{\alpha 3}(\mathbf{r}_i, \overline{\mathbf{r}}_j) \ , \end{aligned} \tag{3.51}$$

here, the subscripts α, β, m denote vectorial or matrix components, $\delta_{\alpha\beta}$ is the Kronecker symbol and $(\overline{\mathbf{r}}_j)_m$ is the m-th component of $\overline{\mathbf{r}}_j$. Note that Einstein's summation convention has been adopted in equation (3.51) with respect to the index m. The calculated matrix components of the stresslet and sourcelet part of Blake's Green's tensor $\delta\mathbf{G}^{im}(\mathbf{r}_i, \overline{\mathbf{r}}_j)$ can be found in [21] and are also given in Appendix A.1.

3.8.2 Calculation of mobility matrices near a planar boundary

If all particles are far enough apart from each other to be considered point-like, it suffices to use the Blake tensor for the mobility functions as some authors do, e.g., [12]. It gets more difficult when the particles come closer and their finite sizes become relevant.

Several approaches using multipole expansion techniques have addressed the problem for a single sphere [31] and two-sphere-interactions [9, 21]. In these cases, a multipole expansion of the hydrodynamic force density induced on the spheres and Blake's image representation, to account for the bounding wall are used. However, the expansions and solutions are expressed in two infinite sets of solutions to the homogeneous Stokes equation consisting of complex functions similar to the spherical harmonics in quantum mechanics. Even though the concept of this approach simple, producing results with it is a complicated enterprise.

Here, following [3], another way is chosen to derive mobility functions on the Rotne-Prager level. Analogous to equation (3.14), a point force $\mathbf{f}_0$ located at a location $\mathbf{r'}$ above the plane generates a velocity field at $\mathbf{r}$

$$\mathbf{u}(\mathbf{r}) = \frac{\mathbf{G}^{Blake}(\mathbf{r}, \mathbf{r'})}{8\pi\eta} \cdot \mathbf{F}_0 \ , \tag{3.52}$$

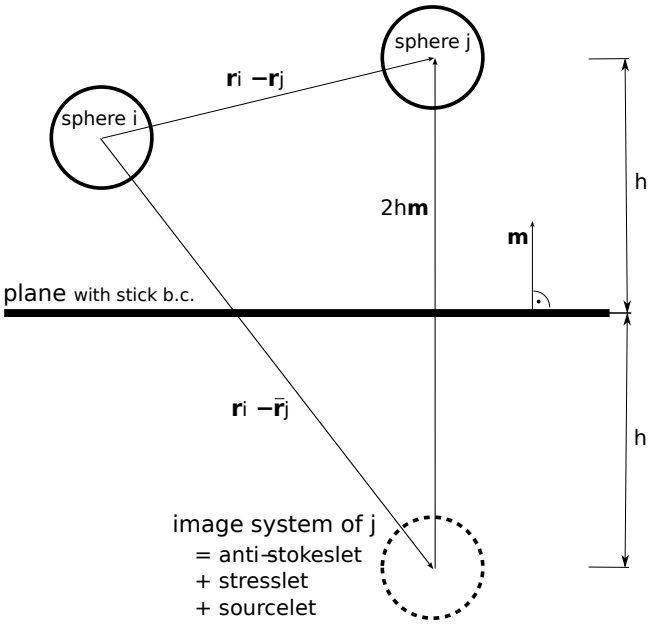

Fig. 3.2: Geometry of the Blake tensor. The disturbance at point $\mathbf{r}_j$ gets mirrored across the infinite plane. The height of $\mathbf{r}_j$ above the plane is given by h and the unit normal to the plane is $\mathbf{m}$.

the use of $\mathbf{G}^{Blake}(\mathbf{r}, \mathbf{r'})$ intstead of the Oseen tensor ensures that the velocity field is zero on the bounding plane. Now consider $\mathbf{f}(\mathbf{r'})$ to be the force density on the surface ∂V_j of a sphere j with its centre at $\mathbf{r}_j$. Expanding $\mathbf{G}^{Blake}(\mathbf{r}, \mathbf{r'})$ about $\mathbf{r'} = \mathbf{r}_j$ yields for the flow field

$$\begin{aligned} \mathbf{u}(\mathbf{r}) &= \frac{1}{8\pi\eta} \int_{\partial V_j} \mathbf{G}^{Blake}(\mathbf{r}, \mathbf{r'}) \cdot \mathbf{f}(\mathbf{r'}) \, \mathrm{d}S' \\ &= \frac{1}{8\pi\eta} \left[\left(1 + \frac{a^2}{6} \nabla^2_{\mathbf{r'}} + \dots \right) \mathbf{G}^{Blake}(\mathbf{r}, \mathbf{r'}) \right]_{\mathbf{r'}=\mathbf{r}_j} \cdot \mathbf{F}_j \ . \end{aligned} \tag{3.53}$$

The expansion is truncated after the monopole and the quadrupole because this would give the exact solution for an isolated sphere in an unbounded fluid, as has been shown in sections 3.3.3, 3.4. The quadrupole contribution is necessary to account for the finite size of the sphere as elaborated in [13]. Higher order terms due to the presence of the bounding wall are neglected, so the generated flow field using Blake's tensor is just an approximation and not valid close to the particle. The effect on the motion of another sphere i is computed using Faxén's theorem:

$$\mathbf{v}_i = \frac{1}{6\pi\eta a} \mathbf{F}_i + \left(1 + \frac{1}{6} a^2 \nabla^2_{\mathbf{r}_i} \right) \mathbf{u}(\mathbf{r}_i) \ . \tag{3.54}$$

To calculate the self-mobility of a sphere, we start with the Stokes mobilitiy. However, we need to also consider the image system of the sphere because its flow field will have an effect on the self-mobility, particularly so when the sphere is close to the bounding wall. Consequently, the flow field of the image system is expanded and the effect at the position of the sphere is then evaluated by Faxén's theorem. Combining equations (3.53) and (3.54) and comparing

with the formal definition of the mobility function, one identifies:

$$\boldsymbol{\mu}_{ii} = \frac{1}{8\pi\eta}\left[\frac{4}{3a}\hat{\mathbf{I}} + \left(1+\frac{a^2}{6}\nabla^2_{\mathbf{r}_i}\right)\left(1+\frac{a^2}{6}\nabla^2_{\bar{\mathbf{r}}_i}\right)\Delta\mathbf{G}^{Blake}(\mathbf{r}_i,\bar{\mathbf{r}}_i)\right] \tag{3.55}$$

$$\boldsymbol{\mu}_{ij} = \frac{1}{8\pi\eta}\left[\left(1+\frac{a^2}{6}\nabla^2_{\mathbf{r}_i}\right)\left(1+\frac{a^2}{6}\nabla^2_{\mathbf{r}_j}\right)\mathbf{G}^{Blake}(\mathbf{r}_i,\mathbf{r}_j)\right] \ , \tag{3.56}$$

where

$$\Delta\mathbf{G}^{Blake}(\mathbf{r}_i,\bar{\mathbf{r}}_i) = \mathbf{G}(\mathbf{r}_i-\bar{\mathbf{r}}_i) + \delta\mathbf{G}^{im}(\mathbf{r}_i,\bar{\mathbf{r}}_i)$$

is the appropriate image system for the interaction of a sphere with a wall that is required for calculating the self-mobility.

To summarize: Application of the differential operator

$$\frac{1}{8\pi\eta}\left(1+\frac{a^2}{6}\nabla^2_{\mathbf{r}_i}\right)\left(1+\frac{a^2}{6}\nabla^2_{\mathbf{r}_j}\right)$$

to the components of Blake's Green tensor gives the components for the hydrodynamic interaction matrix between two spheres close to a wall. After a little thought (or by explicit calculation), it is clear that application to the two Oseen terms in Blake's tensor just reproduces Rotne-Prager matrices. The more complicated part is the calculation of the sourcelet and the stresslet contribution to the mobility functions, see Appendix A.2.

In this approximation the mobility functions for pairwise interaction of equally sized spheres close to an infinitely extended plane are:

$$\boldsymbol{\mu}^{wall}_{ii} = \mu_0\hat{\mathbf{I}} - \boldsymbol{\mu}^{rp}(\mathbf{r}_i-\bar{\mathbf{r}}_i) + \delta\boldsymbol{\mu}_{self} \tag{3.57}$$

$$\boldsymbol{\mu}^{wall}_{ij} = \boldsymbol{\mu}^{rp}(\mathbf{r}_i-\mathbf{r}_j) - \boldsymbol{\mu}^{rp}(\mathbf{r}_i-\bar{\mathbf{r}}_j) + \delta\boldsymbol{\mu}_{ij} \ . \tag{3.58}$$

Here the $\boldsymbol{\mu}^{rp}(\mathbf{x}-\mathbf{y})$ are Rotne-Prager tensors. The components of $\delta\boldsymbol{\mu}_{self}$ and $\delta\boldsymbol{\mu}_{ij}$ are given in Appendix A.2.

Chapter 4

Dynamics of discrete superparamagnetic filaments

The goal of this chapter is to develop a model of a slender filament composed of superparamagnetic particles that can be used subsequently for simulating the wiggling of flagella and the beating of cilia. With this in mind, we start by presenting mechanical properties of slender elastic rods. Once the Hamiltonian governing such a rod has been established, we continue by introducing the so-called bead-spring model, which is a computationally efficient, discretized realisation of the elastic rod. The beads are assumed to be superparamagnetic and thus develop a dipole moment in the presence of an external magnetic field. This enables us to actuate the filament by dipolar interactions in analogy to the experimental filaments of the group of J. Bibette [14, 11]. As another major advantage, hydrodynamic interactions can be conveniently included in the bead-spring model. After the more technical details of the simulations have been dealt with, we proceed to the next step of this chapter and undertake a rescaling of the equations governing the dynamics of such a system. This leads to scaling laws that reduce the number of relevant parameters needed to characterize our model filament. Towards the end of this chapter, predictions of the scaling laws are compared to simulation data. The task of swimming and ciliary beating, however, will then be addressed in the following chapters.

4.1 Elastic rod as a wormlike chain

As the filaments used for generating propulsion and net fluid transport have a shape similar to a long elastic cylinder, it is appropriate to study the physical properties of such objects.

Consider a long and thin elastic rod of cylindrical shape with diameter d and length L. For $d \ll L$ the position on the rod can be parameterized by one scalar variable $s \in [0, L]$ specifying the position along the rod starting from one of the ends which is shown in figure 4.1. In the following, such a slender rod will also be called filament, as has been done before in section 2.3. The state of deformation of a short segment $\mathrm{d}s$ of the elastic rod is fully characterized by three local parameters [29]:

- the stretch or extensional deformation is a dimensionless scalar: $u(s) = \frac{\mathrm{d}\Delta}{\mathrm{d}s}$, where $\mathrm{d}\Delta$ is the change in length of the short segment.

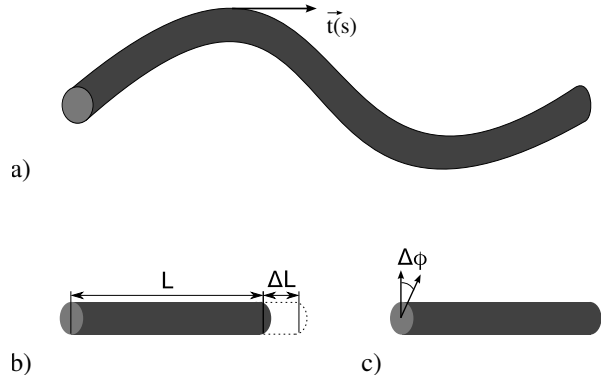

Fig. 4.1: Elastic rod. **a)** rod in a bent configuration; the scalar parameter s describes the position starting from the left end. $\hat{\mathbf{t}}$(s) is the tangent unit at the position s. The bend vector is defined as $\boldsymbol{\beta} = \mathrm{d}\hat{\mathbf{t}}/\mathrm{d}s$. **b)** Definition of stretch or tension. **c)** Definition of a twist density.

- the bend or bending deformation measures the change of direction of the unit tangent along the rod: $\boldsymbol{\beta}(s) = \frac{\mathrm{d}\hat{\mathbf{t}}}{\mathrm{d}s}$.
- the twist density or torsional deformation $\omega(s) = \frac{\mathrm{d}\varphi}{\mathrm{d}s}$, where $\mathrm{d}\varphi$ is the relative angle between the ends of the segment $\mathrm{d}s$.

Any deformation of the rod has an energy cost associated with it. By analogy to Hooke's law, the relationship should be quadratic for small deformations. Energy contributions must be scalar. $\boldsymbol{\beta}$ is a vectorial quantity, precluding products with the scalar parameters. This leaves just four possible terms for the free energy per unit length:

$$w = \frac{1}{2}\left[A\boldsymbol{\beta}^2 + ku^2 + \Xi\omega^2 + \Psi u\omega\right] \ , \tag{4.1}$$

where A is the bend stiffness, k the spring constant and Ξ and Ψ give the twist stiffness and the coupling between twisting and stretching. The total energy of the rod is

$$H = \int_0^L w\mathrm{d}s \ . \tag{4.2}$$

Sometimes, the bend stiffness is expressed in terms of k_BTL_p instead of A with the identity $A = \frac{1}{2}k_BTL_p(D-1)$, where D is the number of spatial dimensions of the system and L_p is called persistence length [38]. It can be shown that L_p is the length of an elastic rod after which all directional correlations are lost due to thermal fluctuations [29]. In this sense, L_p is a more tangible quantity than A and a filament can be characterized by comparing its contour length L to its persistence length L_p:

- A rod with $L \gg L_p$ is a flexible filament with a shape that is anything but straight even if no external forces act on the rod. It performs a random walk in space.
- For $L \approx L_p$ the rod is a semiflexible filament which is not necessarily straight.
- For $L \ll L_p$ it is a rigid rod with a perfectly straight shape in absence of external forces acting on it.

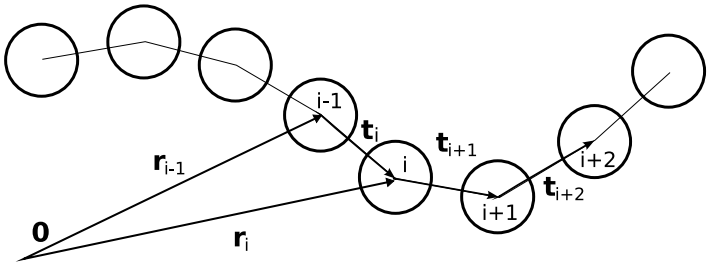

Fig. 4.2: Bead-spring model. The linkers are given by $\mathbf{t}_i = \mathbf{r}_i - \mathbf{r}_{i-1}$ and connect the centres of two adjacent beads.

For instance, the persistence length L_p of the bio-polymer DNA is roughly 50 nm while it is around 20 μm for actin filaments. In this work, however, thermal fluctuation of the elastic rod are neglected since the persistence length L_p of the model filaments that we consider in the following are much larger than their lengths L.

For the filaments we use with the intention of modelling artificial cilia and flagella, not all energy contributions in equation (4.1) are equally relevant. We neglect torsional deformations since our model will not rely on torques that could lead to twisting of the filament. For the goal of generating propulsion by periodic deformations, the bending of a filament is the essential deformation to be considered, whereas stretching of the filament is not important. When inextensibility is also assumed, the energy density (4.1) reduces to only the bending term. These kinds of filaments are commonly referred to as *wormlike chains*.

In analytical treatments, inextensibility is a restriction that can be introduced by a Lagrangian multiplier [7]. Its implementation in simulations is done in a straightfoward fashion [23] but requires an advanced algorithm and additional computing power. It is numerically more efficient to include stretching of the filament but to use a large spring constant k that keeps variations of the filament length small.

4.2 Bead-spring model

The so-called *bead-spring model* is the discretized representation of the wormlike chain model introduced in the previous section. The general idea of a discrete description of an elastic filament is to express the elastic forces of bending and stretching in a way that they only act on a finite number of N discrete points $\mathbf{r}_i$ along the filament. Furthermore, in the bead-spring model the three-dimensional character of a flexible filament is considered by positioning beads at the discretization points $\mathbf{r}_i$. Thus, the bead-spring model is simply a linear chain of beads. The centres of two adjacent beads are connected by stiff linkers as illustrated in figure 4.2. The bond vector between bead $i-1$ and i is defined as

$$\mathbf{t}_i = \mathbf{r}_i - \mathbf{r}_{i-1} \tag{4.3}$$

and the length of the bond is subsequently denoted by $l_i = |\mathbf{t}_i|$. Moreover, l_0 gives the equilibrium length with respect to stretching. In this simple model all forces (of elastic or other origin) are assumed to act on the centres of the beads. This makes sure that no torques on the beads ensue. The linkers are extensible in length but do not bend. Bending occurs only through swivelling of the respective linkers around the points $\mathbf{r}_i$.

Since we are interested in filaments that are immersed in a highly viscous environment, we need to consider the friction of the filament with the surrounding fluid through the spheres that also interact hydrodynamically. This justifies a short overview over several approaches for obtaining friction coefficients of elastic rods.

Generally speaking, the calculation of viscous friction coefficients (or, equivalently, hydrodynamic mobilities) can be a daunting task for objects of arbitrary shape. However, analytical solutions exist for particles that exhibit a high degree of symmetry like, e.g., a perfect sphere (see chapter 3). One suggested workaround for particles with a more complex shape is that of modelling the object with (different-sized) spheres as closely as possible. Alternatively, the volume or specifically the surface can be constructed of a packaging of much smaller beads [37].

The first approach works especially well for a long thin cylinder, which is modelled by a linear chain of beads, as elucidated in [10]. In the limit of very long cylinders $L \gg d$ with length L and diameter d, analytically valid expressions for the friction coefficients can be given [10]:

$$\begin{aligned} \zeta_{\parallel} &= \frac{2\pi\eta L}{\log(L/d)} \,, \\ \zeta_{\perp} &= 2\zeta_{\parallel} \,, \end{aligned} \tag{4.4}$$

where $\zeta_{\parallel}$ is the friction coefficient parallel to the long axis of the cylinder and $\zeta_{\perp}$ orthogonal to it and, as before, η is the viscosity of the fluid. However, these results are only applicable to straight cylinders.

In *slender-body theory*, the expressions for a slender cylinder (4.4) are nevertheless assumed to be locally correct for each short segment ds of a bent slender filament. By this approach, hydrodynamic interactions between the segments are, however, neglected. The slender-body approximation has already been used in section 2.3 in connection with the elastohydrodynamic problems EHDI and EHDII.

Now let us go back to the bead-spring model. The linkers are assumed to be slender enough so that friction with the fluid can be ignored. In this case, only the spheres of the bead-spring model remain and their friction coefficients are already known. Furthermore, we have also developed a method for including hydrodynamic interactions between two spheres to a good approximation in chapter 3. Therefore, the task of describing friction with the fluid and even hydrodynamic interactions of an elastic filament is comparatively simple for the bead-spring model.

To summarize: by introducing the bead-spring model, we have managed to find a description of an elastic filament in a highly viscous environment, in which the difficult problems of satisfying elastic properties and the consideration of hydrodynamic interactions can both be mapped to a many-body problem of N spheres. Each of them has its own equation of motion, although the equations of motion are coupled by hydrodynamic interactions and elastic bending and stretching forces. The bead-spring model is quite a common approach to various problems. Indeed, the technique has been numerously employed for simulations both with and without hydrodynamic interactions by e.g. [27, 23, 24, 26] and has recently also been experimentally realised by Bibette *et al.* [14, 11].

4.3 Discretizing the wormlike chain model

The bead-spring model as described in section 4.2 requires the discretization of the bending and stretching energy and a subsequent calculation of forces acting on the points connecting two linkers.

4.3.1 Stretching forces

Keeping the overall length of the filament close to its equilibrium value is attained by linkers that act like relatively stiff springs and obey Hooke's law. Thus, the total energy stored in stretching the filament is given by the sum over the squared deviations of each linker from its equilibrium length:

$$H^S = \frac{1}{2}k\sum_i (l_i - l_0)^2 \ . \tag{4.5}$$

The force acting on bead i is then given by Hooke's law:

$$\mathbf{F}_i^S = -k(l_i - l_0)\hat{\mathbf{t}}_i + k(l_{i+1} - l_0)\hat{\mathbf{t}}_{i+1} \ . \tag{4.6}$$

4.3.2 Bending forces

In section 4.1 we introduced the bend energy of an elastic rod as a line integral over the squared curvature $\boldsymbol{\beta}$ of the filament

$$H_0^B = \frac{1}{2}A\int_0^L \mathrm{d}s \left(\frac{\mathrm{d}\hat{\mathbf{t}}}{\mathrm{d}s}\right)^2 \ , \tag{4.7}$$

where A denotes the bending stiffness in [Jm], s is the arclength along the rod with $s \in [0, L]$ and $\hat{\mathbf{t}}(s)$ is the unit tangent along the rod. Application of the bending energy to the discrete bead-spring model requires a discretization of equation (4.7). For this purpose, $\mathrm{d}s$ is substituted by l_0

$$\begin{aligned} H^B &= \frac{A}{2}\sum_{i=2}^{N-1} l_0 \left(\frac{\hat{\mathbf{t}}_{i+1} - \hat{\mathbf{t}}_i}{l_0}\right)^2 \\ &= \frac{A}{l_0}\sum_{i=2}^{N-1}(1 - \hat{\mathbf{t}}_{i+1}\cdot\hat{\mathbf{t}}_i) \ . \end{aligned} \tag{4.8}$$

In our model bending forces act on the points $\mathbf{r}_i$ connecting two linkers. We obtain them from equation (4.8) as $\mathbf{F}_i^B = -\nabla_{\mathbf{r}_i} H^B$ using $\hat{\mathbf{t}}_i = \frac{\mathbf{r}_i - \mathbf{r}_{i-1}}{|\mathbf{r}_i - \mathbf{r}_{i-1}|}$. Several tangent vectors contribute to $\mathbf{F}_i^B$. To facilitate the calculation of $\mathbf{F}_i^B$ at both ends of the filament, it is advantageous to introduce the bending potential as follows:

$$H^B = \frac{A}{l_0}\sum_{i=1}^{N} f_i(1 - \hat{\mathbf{t}}_{i+1}\cdot\hat{\mathbf{t}}_i) \ , \qquad f_i = \begin{cases} 1 & : \ i > 1 \ ; \ i < N \\ 0 & : \ i \leq 1 \ ; \ i \geq N \end{cases} \ . \tag{4.9}$$

A lengthy calculation using the relations $\nabla_{\mathbf{r}_i}\hat{\mathbf{t}}_i = \frac{1}{l_i}(1 - \hat{\mathbf{t}}_i\hat{\mathbf{t}}_i)$ and $\nabla_{\mathbf{r}_i}\hat{\mathbf{t}}_{i+1} = -\frac{1}{l_i}(1 - \hat{\mathbf{t}}_{i+1}\hat{\mathbf{t}}_{i+1})$ from [15] finally gives

$$\begin{aligned}\mathbf{F}_i^B &= \frac{A}{l_0}\left\{\frac{f_{i-1}}{l_i}\hat{\mathbf{t}}_{i-1} - \left[\frac{f_{i-1}}{l_i}\hat{\mathbf{t}}_{i-1}\cdot\hat{\mathbf{t}}_i + \frac{f_i}{l_{i+1}} + \frac{f_i}{l_i}\hat{\mathbf{t}}_i\cdot\hat{\mathbf{t}}_{i+1}\right]\hat{\mathbf{t}}_i\right. \\ &+ \left.\left[\frac{f_i}{l_{i+1}}\hat{\mathbf{t}}_i\cdot\hat{\mathbf{t}}_{i+1} + \frac{f_i}{l_i} + \frac{f_{i+1}}{l_{i+1}}\hat{\mathbf{t}}_{i+1}\cdot\hat{\mathbf{t}}_{i+2}\right]\hat{\mathbf{t}}_{i+1} - \frac{f_{i+1}}{l_{i+1}}\hat{\mathbf{t}}_{i+2}\right\} . \qquad (4.10)\end{aligned}$$

This is the restitution force resisting a bent configuration that acts on each bead i.

4.4 Actuation of the filament by dipolar interactions

Having thus established the mechanical properties of a discrete filament composed of spheres, we still need to find a way to induce a motion of the filament. Several driving mechanisms exist in biology. The rotating helical flagellum that *E. coli* bacteria use for swimming is powered by a rotary molecular motor. *Spermatozoa* swim by propagating a wave down their tail, which requires complicated internal machinery [26]. Many cilia rely on the internal mechanism of an axoneme, which is a cylindrical arrangement of parallel doublets of microtubules that generate internal stresses through sliding relative to each other powered by molecular dynein motors [7]. With the notable exception of rotary motors, all other mentioned mechanisms consist of a complicated interplay of inherently active elements over the full length of the filament. These techniques merit a detailed discussion in their own right. The beating of cilia, for example, is analysed by Gueron and Levit-Gurevich [17, 18] who use a complicated mathematical function that describes the filament shape in time to good accuracy. Another notable approach to the question of ciliary beating that builds directly on the internal structure of the axoneme is given by Camalet and Jülicher [7].

For developing a simulation model, the technique employed by Dreyfus *et al.* [11] of actuation through dipolar interaction in an external magnetic field has several advantages. On the one hand, the description is simple and can easily be incorporated into a scaling model of the discrete filament as will be done in section 4.7. More importantly though, models built on these assumptions can be realised and verified experimentally, as has been done for the one-armed swimmer [11]. From an experimental vantage, such an approach is feasible since the energy required for motion is transmitted to the system by means of a time-varying external magnetic field. The amplitude and frequency of the wiggling magnetic field control the swimming and even allow for steering.

4.4.1 Magnetic drive

A free magnetic dipole aligns itself parallel to an external magnetic field, as this is the position of minimal potential energy. In (super)paramagnetic particles, the dipole moments are induced parallel to the field and each dipole already possesses minimal energy. In a chain of induced dipoles, however, the particles will be displaced due to dipole-dipole interactions. The potential of two parallel dipoles at a fixed distance has a minimum for the configuration where both dipoles are behind each other in a straight line as illustrated in figure 4.3. In the plot on the right one can see that two parallel dipoles in line attract each other while two parallel dipoles orthogonal to the connecting vector repel. For this reason, a linear chain of induced dipoles always has the tendency to align with the external field. In absence of inertia,

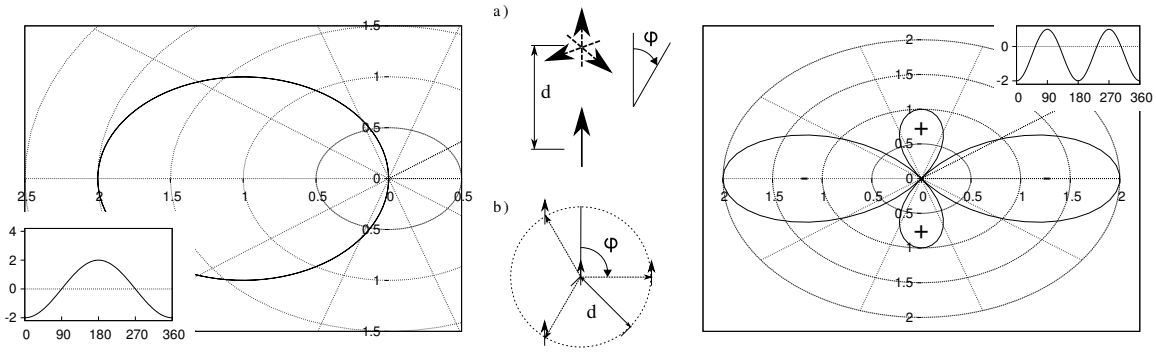

Fig. 4.3: Interaction of two dipoles: interaction potential H^D of two dipoles of equal strength at a fixed distance d. The main plots are in polar coordinates, starting due east with $\varphi = 0°$ and going up to $\varphi = 360°$ clockwise. The solid line gives the potential in arbitrary units. The distance from the centre of the plot (as shown with the help of the dotted ellipses) gives the magnitude of the potential for a given φ. The insets show the same graph in an xy-plot where the x-axis gives the angle in degrees and the the y-axis the potential energy in arbitrary units. **Left:** one dipole is aligned with the vector pointing to the other dipole, whereas the orientation of the second dipole is the angular coordinate of the polar plot; see drawing a) in the middle. **Right:** Both dipoles are parallel at all times and the angular coordinate is the angle of the connecting vector with the dipole orientation; drawing b) in the middle.

viscous damping resists an immediate alignment for a time varying magnetic field. Due to its elasticity the chain acquires a state of bending while following the field as illustrated in figure 4.4. As has been argued in section 2.3, bending is crucial for eluding Purcell's scallop theorem that applies to all reciprocal motion.

The actuation of a chain of induced dipoles is a straightforward and also experimentally realisable model that is well-suited for our goal of studying propulsory properties of biomimetic filaments in a viscous environment.

4.4.2 Dipolar forces

In the presence of a homogenous external magnetic field $\mathbf{B}$, spherical paramagnetic bodies develop a magnetic dipole moment according to

$$\mathbf{p}(t) = \frac{4\pi a^3}{3\mu_0} \boldsymbol{\chi} \cdot \mathbf{B}(t) \ . \tag{4.11}$$

Here, $\boldsymbol{\chi}$ is the magnetic susceptibility per unit volume. Note that in this context μ_0 refers to the magnetic permeability of vacuum rather than a hydrodynamic mobility. In real colloids $\boldsymbol{\chi}$ is often not perfectly isotropic and has two different values parallel and orthogonal to a symmetry axis $\mathbf{s}$, so that $\boldsymbol{\chi} = \chi_\parallel \mathbf{ss} + \chi_\perp(\hat{\mathbf{I}} - \mathbf{ss})$ [11]. We will not bother with these complications and just assume an isotropic material with scalar susceptibility χ:

$$\mathbf{p}(t) = \frac{4\pi a^3}{3\mu_0} \chi \mathbf{B}(t) \ . \tag{4.12}$$

Disregarding the fact that all dipoles contribute to the local magnetic field of a certain dipole, we can assume all dipoles to be perfectly aligned with the externally supplied magnetic

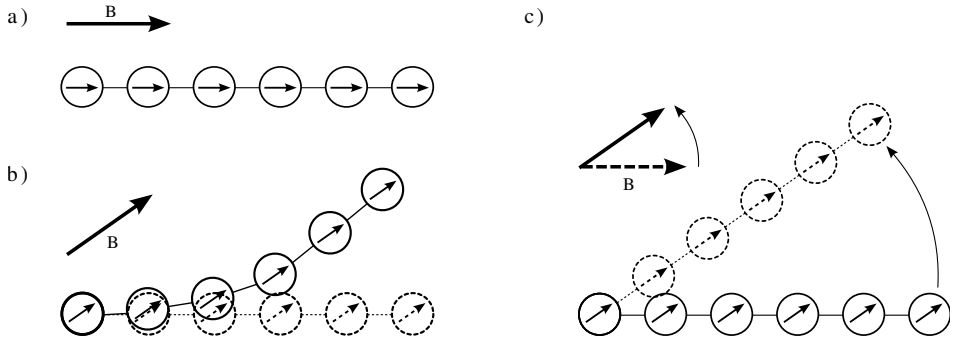

Fig. 4.4: Alignment of a chain of dipoles: **a)** in equilibrium a chain of dipoles in a constant magnetic field is aligned with the field vector B. If a change of direction of the **B** vector occurs but is sufficiently slow for the chain to follow, this is still the prevalent picture. **b)** A sudden or fast change of the field direction has the consequence that the chain cannot follow immediately and bending occurs. **c)** shows the chain just after a change of direction of **B**, after a long enough time the parallel alignment will again be achieved. In the pictures shown the left end is kept at a fixed position, otherwise the reorientation would be symmetric about the middle of the chain.

field at any time. The most general expression for dipole-dipole interaction is given by [4]

$$H^D = \sum_{i,j} \frac{\mu_0}{4\pi} \frac{\mathbf{p}_i \cdot \mathbf{p}_j - 3(\mathbf{p}_i \cdot \hat{\mathbf{r}}_{ij})(\mathbf{p}_j \cdot \hat{\mathbf{r}}_{ij})}{r_{ij}^3} \ . \tag{4.13}$$

The corresponding force on a single dipolar bead is then obtained in the usual way by $\mathbf{F}_i^D = -\nabla_{\mathbf{r}_i} H^D$, which works out to [4]

$$\mathbf{F}_i^D = \frac{3\mu_0}{4\pi} \frac{(\mathbf{p}_i \cdot \hat{\mathbf{r}}_{ij})\mathbf{p}_j + (\mathbf{p}_j \cdot \hat{\mathbf{r}}_{ij})\mathbf{p}_i + (\mathbf{p}_i \cdot \mathbf{p}_j)\hat{\mathbf{r}}_{ij} - 5(\mathbf{p}_i \cdot \hat{\mathbf{r}}_{ij})(\mathbf{p}_j \cdot \hat{\mathbf{r}}_{ij})\hat{\mathbf{r}}_{ij}}{r_{ij}^4} \ . \tag{4.14}$$

Both the energy and the force term are simplified in the case where both dipole-moment vectors are parallel and have the same magnitude, $\mathbf{p}_i = \mathbf{p}_j$, as is the case for identical beads in a homogeneous external field.

4.5 Equations of motion in the bead-spring model

According to equation (3.3) the full equation of motion for a bead immersed in a viscous medium reads

$$\begin{aligned} \mathbf{v}_i &= \sum_{j=1}^{N} (\boldsymbol{\mu}_{ij}^{tt} \cdot \mathbf{F}_j + \boldsymbol{\mu}_{ij}^{tr} \cdot \mathbf{T}_j) \ , \\ \boldsymbol{\omega}_i &= \sum_{j=1}^{N} (\boldsymbol{\mu}_{ij}^{rt} \cdot \mathbf{F}_j + \boldsymbol{\mu}_{ij}^{rr} \cdot \mathbf{T}_j) \ . \end{aligned}$$

Although there are several ways in which rotational degrees of freedom could be relevant, we neglect them for two reasons. First, there is no torque acting on the beads of our system as we will explain below. Secondly, any translational-rotational coupling by hydrodynamic

interactions is small and can be neglected. This is especially true because our model does not rely on the rotational state of the beads which is therefore not even evaluated. So even if translational-rotational coupling occurred, it would not make a difference to our representation of the bead spring model.

Let us think of a deformation necessitating a rotation of the beads in the bead-spring model. It is immediately clear that stretching has no influence on a bead's state of rotation. If twisting were possible, the beads of the chain would have to rotate; but this is not the case because the bead-spring model, as adapted for our model filament, does not consider torsional deformations. Let us look at bending: In our bead-spring model a linker connects the centres of two beads (see section 4.2). Hence, we have no coupling between bending and rotations of the constituent beads of the flexible filament. Note that this is different for the bead-spring model of the artificial cilia of [14], in which the linkers are glued to the surfaces of the beads. This necessitates a slight rotation of the beads when the filament is bent, albeit the angles of rotation remain small.

Thus disregarding the rotational degrees of freedom of the beads greatly simplifies the equations of motion to

$$\mathbf{v}_i = \sum_{j=1}^{N} \boldsymbol{\mu}_{ij} \cdot (\mathbf{F}_j^S + \mathbf{F}_j^B + \mathbf{F}_j^S) \ . \tag{4.15}$$

Numerical integration of these N equations fully determines the trajectories of all beads and thus governs the dynamics of the whole filament. The mobilities $\boldsymbol{\mu}_{ij}$ and the bending and stretching forces solely depend on the spatial configuration of the beads, while the dipolar forces have a time dependence through the orientation of the magnetic field that changes with time.

Note that analytical solutions are feasible only in absence of hydrodynamic interactions and for the restriction to next neighbour interactions, an example of an equation of motion for such a system is given in [11, 35]. For the equations (4.15), however, the dependence on the coordinates of all N particles only allows for numerical integration of the equations of motion.

4.6 Simulation details

4.6.1 Integration methods

The equation of motion (4.15) is a differential equation of first order with respect to the time variable t. Once an initial state has been chosen, one obtains an approximation of the trajectories $\mathbf{r}_i(t)$ by numerically integrating the $\mathbf{v}_i$. For example, the position of bead i, $\mathbf{r}_i$, at time $t_0 + \Delta t$ is given by the formula $\mathbf{r}_i(t_0 + \Delta t) = \mathbf{r}_i(t_0) + \Delta t \mathbf{v}_i(t_0)$ commonly known as Euler's method. In this way the time-dependent trajectories of all beads can be simulated. However, while Euler's method may be the simplest way of advancing a solution through a small time interval Δt, in general it does not produce the best results as will be outlined in the following. Using Euler's method, an improved accuracy can only be achieved by smaller time steps Δt. This question of the necessary time resolution is addressed in section 4.6.2 as it is connected to characteristic relaxation times of the system.

Although most simulations of the present work make use of the simple Euler integration technique, in some cases results need to be "double-checked" with the more advanced fourth

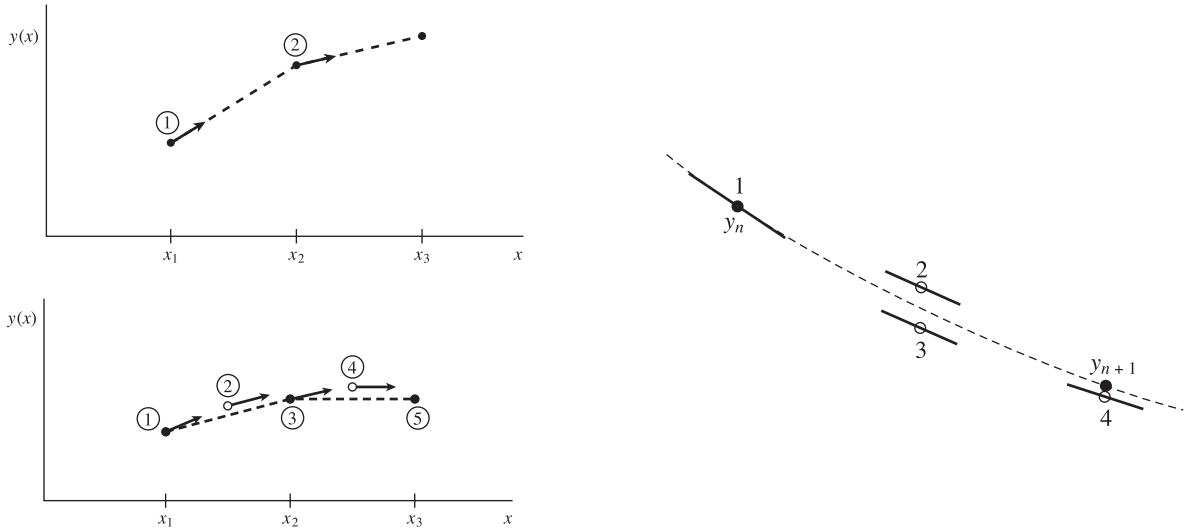

Fig. 4.5: Runge-Kutta integration from [30]. **Left top:** Euler's method with first order accuracy. The derivative is taken on one end of the interval between x_1, x_2. **Left Bottom:** the mid-point method has second order accuracy. Derivative information is taken in the middle of the interval at the position of the open dots. These points are discarded after evaluation of the derivative. **Right:** schematic representation of fourth order Runge-Kutta integration. Four different derivatives need to be evaluated for each step giving the high level of accuracy.

order Runge-Kutta algorithm. Hence, both techniques will be described briefly, following *Numerical Recipies in C* [30].

Let $\frac{\mathrm{d}}{\mathrm{d}x}y = f(x, y(x))$ be a differential equation, then Euler's simple method for a step size h,

$$y_{n+1} = y_n + hf(x_n, y_n) \ , \tag{4.16}$$

advances the solution from x_n to $x_{n+1} = x_n + h$. The problem with this approach is that it approximates the solution through the interval h in an unsymmetric way only considering informations about the derivative from the beginning of the interval. Therefore, the error of the step is of order $O(h^2)$ which is clear from equation (4.16) when viewed as Taylor expansion of $y(x)$ about x_n. With the following scheme, Euler's method can be improved by evaluating the derivative at the midpoint of the interval:

$$\begin{aligned} k_1 &= hf(x_n, y_n) \ , \\ k_2 &= hf(x_n + \frac{1}{2}h, y_n + \frac{1}{2}k_1) \ , \\ y_{n+1} &= y_n + k_2 + O(h^3) \ . \end{aligned} \tag{4.17}$$

This approach is called second-order Runge-Kutta or midpoint method. The accuracy indicated in the third line of equation (4.17) becomes clear after a Taylor expansion of k_2. However, one can do a lot better than that: the classical fourth-order Runge-Kutta formula

is even more advanced and accurate to order $O(h^5)$:

$$\begin{aligned} k_1 &= hf(x_n, y_n) \ , \\ k_2 &= hf(x_n + \frac{1}{2}h, y_n + \frac{1}{2}k_1) \ , \\ k_3 &= hf(x_n + \frac{1}{2}h, y_n + \frac{1}{2}k_2) \ , \\ k_4 &= hf(x_n + h, y_n + k_3) \ , \\ y_{n+1} &= y_n + \frac{k_1}{6} + \frac{k_2}{3} + \frac{k_3}{3} + \frac{k_4}{6} + O(h^5) \ . \end{aligned} \tag{4.18}$$

Figure 4.5 shows a graphical representation of the three methods described. Of course, further refinements can be made by, e.g., adaptive step size control of h [30]. In an interval of x in which $\frac{\mathrm{d}}{\mathrm{d}x}y(x)$ is large, i.e. the value of y changes a lot for only minor changes of x, a smaller step size h improves performance. On the other hand in an interval of x in which y is more constant and predictive somewhat larger steps may be sufficiently accurate.

Application of Runge-Kutta to the particles' trajectories is done by identifying the positions $\mathbf{r}_i$ with y, $\mathbf{v}_i$ with f and h with the time step Δt. Remember that $\mathbf{v}$ is a function of $\mathbf{v} = \mathbf{v}(\mathbf{M}(\mathbf{R}), \mathbf{F}(\mathbf{R}))$ where $\mathbf{M}$ is the full mobility matrix, $\mathbf{F}$ the corresponding force vector on all particles and $\mathbf{R}$ the positional coordinates of all particles. For this reason, all evaluations of $k_1, \ldots, k_4$ in equation (4.18) entail the full computational cost of an Euler step each and yet the solution is only advanced by one step h. In terms of computational efficiency, adapting Runge-Kutta only makes sense if the effective step size can be reliably chosen four times as big as would be required for an Euler integration.

In the context of our simulations, though, fourth-order Runge-Kutta does not perform significantly better than Euler's method at the same step size Δt. This becomes apparent when looking at often occurring problems in the simulations of the present work (see section 4.6.2). The problems seem to be connected to the nature of the equation of motion of the system rather than to numerical inaccuracies of integration.

In the system studied here, several relaxation processes to equilibrium take place on different time-scales at any point in the simulation. This is in stark contrast to freely evolving solutions of differential equations which allow for inaccuracies to add up over time. Because of this fundamental difference, advanced integration algorithms are basically superfluous since small errors relax back towards equilibrium as well.

4.6.2 Numerical instabilities

The discretization of time that is necessary for numerically simulating a filament entails problems that do not exist with a continuous time variable. Similarly, the bend relaxation of a discretized filament is problematic when the local curvature is big.

Both processes of bending and stretching have characteristic relaxation times that need to be resolved in the simulation time steps. These relaxation times are determined by the absolute values of the spring constant and the bend stiffness, respectively. Hence, for certain desired elastic properties, one is stuck with relaxation times that are typically some orders of magnitude faster than the filament dynamics. The problem is particularly acute for the stretch relaxation as the demand to keep the filament nearly inextensible sets the time resolution of required simulation steps per cycle. Numerically it has been found that each cycle of the filament motion needs 10^4 to 10^5 integration steps at the optimal actuation frequency.

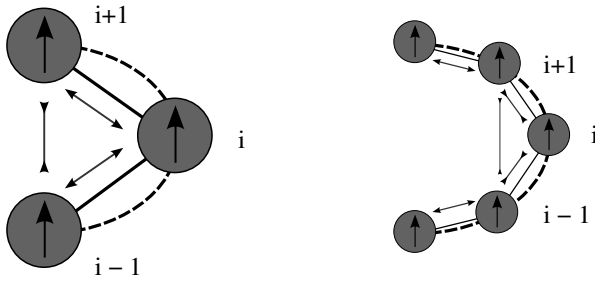

Fig. 4.6: The same curve drawn as dashed line is shown for two different discretizations. On the left, only three beads are considered and the angle enclosed by the connecting linkers is very far from π, which would mean a straight line. On the right, five beads are used to discretize the dashed line and the angles between the linkers are closer to π. Also schematically shown are the dipolar forces at work with the arrows painted. Inward-pointing arrowheads denote attraction and outward-pointing ones repulsion.

The observed failure of the filament to relax to a straight configuration can be understood to be a consequence of the discrete model for bending. In figure 4.6 the same curve for two different numbers of discretization points is shown. For the configuration on the left it is "hard" to relax back to a straight configuration as we will explain in the following.

Bending forces push bead i to the left. Yet for bead i an immediate motion to the left is not possible due to the inextensibility of the linkers. The bending forces acting on beads $i-1$ and $i+1$ also depend on beads $i-2$, $i-3$ and $i+2$, $i+3$, respectively [see equation (4.10)]. If we assume bead i to be somewhere in the middle of the filament with a hairpin shape (where bead i is the vertex) the considerable viscous resistance of all beads $j > i+1$ and $k < i-1$ needs to be overcome in order to move beads $i-1$ and $i+1$, respectively. Then, no swift "straightening out" of the hairpin can be expected. Furthermore, beads $i-1$ and $i+1$ attract because of dipolar interactions. If these are sufficiently strong, the hairpin possibly becomes even sharper. In this case both the bending forces and the dipolar attraction increase. However, the latter does so with $|\mathbf{r}_{i-1} - \mathbf{r}_{i+1}|^{-4}$ [see equation (4.14)] and hence overcompensates the increased bending forces. Therefore, the hairpin becomes ever sharper and there is consequently no possibility of a relaxation to the straight equilibrium configuration.

On the right of figure 4.6, the same situation is shown for five instead of three beads. This makes a real difference: dipolar forces between beads $i-1$, i and i, $i+1$ help in the relaxation process to a straight configuration because the interaction potential of two dipoles is minimal when the dipoles are aligned one behind the other. In this case both the bending and the dipolar interaction potential give rise to forces that help in "straightening out" the hairpin.

From these explanations, it is clear that failure of relaxing from a highly bent to a straight configuration can be seen as the combined effect of coarse discretization and strong dipolar interactions. There is always a critical local curvature at which a relaxation does not happen anymore. Since dipolar forces depend on the square of the magnetic field strength B, the critical curvature is very sensitive to modifications of B.

An obvious solution for overcoming this problem would be an increase in the number of beads N rather than a finer time resolution or a better integration mechanism. Unfortunately, the computational cost for simulating more beads grows with N^2 due to the pairwise additive mobilities. Accordingly, a discretization with a larger N is often not feasible in terms of the calculating power available.

4.6.3 Simulation parameters

In the following sections, the number of relevant parameters characterizing the filament will be reduced. At the same time, some parameters such as the radius of the beads or the equilibrium length between adjacent beads are not considered to be of particular interest and are kept constant throughout the simulation runs.

Nonetheless, two separate sets of these parameters were used for the simulations. In both systems that differ in size and mechanical properties the same qualitative features are observed thus confirming the scaling properties of the filaments outlined in the next section.

Both parameter sets use the viscosity of water for η and a centre-to-centre distance l_0 of three particle radii between neighbouring beads. For most simulation runs a filament length of 20 beads has proven to satisfy the requirements of a discretization that is not too coarse but is nevertheless computationally efficient. The major differences between the parameter sets are given below while the complete parameter sets can be found in detail in Appendix B.

- In **parameter set I**, the radius of the beads is $a = 2.25$ μm, a realistic value for super-paramagnetic colloids. The bend stiffness is set to $A = 6.75 \cdot 10^{-18}$ Jm, correspoding to a persistence length L_p on the order of 10^3 m which is hardly physically realistic. However, the physics turns out to be the same as in the more realistic parameter set II. All other parameters need to be adjusted and are not free to choose anymore. The spring constant has a value that restricts relative length fluctuations to around 1% (for the actuations we use). The strength of the external field needs to produce dipolar interactions sufficiently strong for the filament to follow the field at a Sperm number between one and ten. Typical actuation frequencies are in the range of 100 to 1000 Hz.

- **Parameter set II** has been introduced with the intention of matching the experimental setup of the one-armed swimmer of Dreyfus *et al.* [11] as closely as possible. The bead radius is $a = 0.5$ μm and the bend stiffness is $A = 4.5 \cdot 10^{-22}$ Jm which gives a persistence length L_p in the centimetre range. As above, spring constant, field strength and frequency range need to be adjusted. Actuation frequencies are on the order of 10 Hz.

4.7 Scaling laws of discrete filaments

Similar to the scaling invariance of a continuous filament with respect to the dimensionless "Sperm number" first introduced by Wiggins and Goldstein [38], an analogous expression can be found for the discretized realisation of a filament that is used throughout this work.

4.7.1 Scaling invariant expressions of the energies

Although the relevant quantities for the equation of motion are forces rather than energies, it is easier to use the energy terms for rescaling due to the simpler structure of the expressions. Moreover, the rescaling cannot be applied to a single bead on its own but is a matter of the whole filament. This fact is reflected in the energy sum in contrast to the force terms that act separately on each single bead.

Expressions $\tilde{H}$ for the relevant energies have to be identified by the demand that $\tilde{H}$ scales with one when the system's parameters such as the filament length are varied. All specific material properties then appear together in a pre-factor α. Of course, the product of the

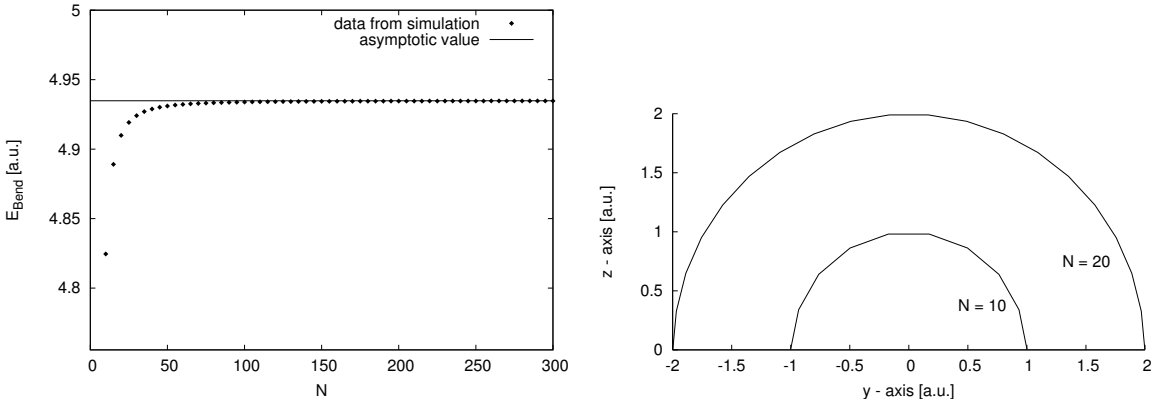

Fig. 4.7: Scaling invariance of the dimensionless bending energy $\tilde{H}^B$ in equation (4.20). **Left plot:** The x-axis shows the number of beads of the filament N, corresponding to the filament length by $L = (N-1)l_0$. The y-axis gives the energy for a semi-circular configuration. It can be seen that the energy term quickly converges for more than 20 beads. Note the scaling of the energy axis, even at $N = 20$ beads the relative deviation is less than 1%. The straight line marked as asymptotic value has been obtained from the simulation at N = 1500. **Right plot:** the semi-circular configuration for which the bending energy is obtained for 10 and 20 beads.

pre-factor and the dimensionless expression will have to be equivalent to the energy terms already given in the previous section: $H = \alpha\tilde{H}$.

The stretching, bending and dipolar energies are functions of positional coordinates with the dimension of a length. In order to introduce dimensionless quantities, coordinates are scaled by the length of the system L. A straightforward calculation for the stretching energy leads to the altered but equivalent expression

$$H^S = \frac{1}{2}k\frac{L^2}{N}\cdot N\sum_i\left(\frac{l_i}{L}-\frac{l_0}{L}\right)^2 \ , \tag{4.19}$$

which consists of a pre-factor before the dot "$\cdot$" with the dimension of an energy and a dimensionless expression only dependent on reduced lengths after the dot.

It is advantageous to apply the rescaling of the bending energy to equation (4.7) rather than to the discretized sum (4.8) because this correctly produces the factor N before the sum:

$$H^B = \frac{A}{L}\cdot N\sum_i(1-\hat{\mathbf{t}}_{i+1}\cdot\hat{\mathbf{t}}_i) \ . \tag{4.20}$$

Expressions (4.20) and (4.8) for the bending energy are also equivalent, but the N just before the sum is the important disctinction that guarantees the scaling invariance we demand above. The correctness of the scaling as a function of the number of beads N is investigated for the special conformation of a semi-circle in figure 4.7. A rapid convergence of $\tilde{H}^B$ to a constant value with deviations of less than 1% for more than 20 beads is observed.

In the same fashion, the dipolar interaction energy is rescaled

$$H^D = N^4\frac{\mu_0\chi^2B^2}{4\pi L^3}\cdot\sum_{i\neq j}\frac{1-3(\hat{\mathbf{r}}_{ij}\cdot\hat{\mathbf{p}})^2}{\tilde{r}_{ij}^3}\frac{1}{N^4} \ , \tag{4.21}$$

where $\hat{\mathbf{p}}$ is a unit vector along the dipole moment $\mathbf{p}$. For small N, $\tilde{H}^D$ depends on N due to the fact that dipoles at both ends of the filament contribute less to $\tilde{H}^D$ than dipoles in

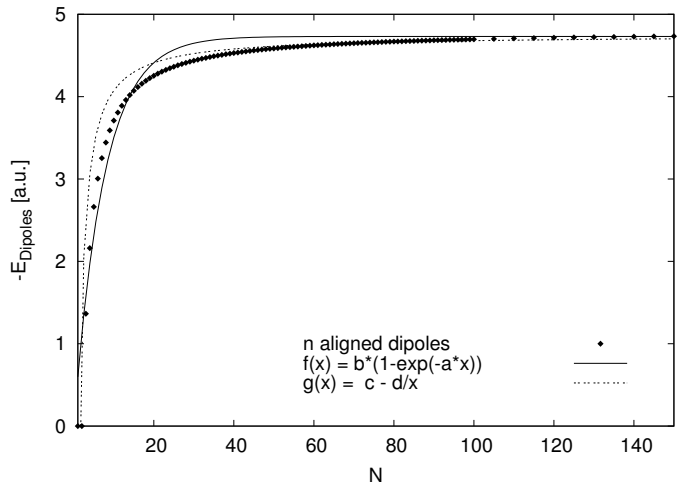

Fig. 4.8: Scaling invariance of the dimensionless dipolar energy contribution $\tilde{H}^D$ in equation (4.20). Again, the x-axis shows the number of beads of the filament. The y-axis gives the energy for a straight configuration. Two attempts to find a fitting curve are also shown. They show that the curve is neither exponential nor just an x^{-1} law, but roughly converges like the latter in the interesting range between 20 and 100. A slight divergence for large N has its cause in the fact that just a finite set of data up to $N = 1000$ has been used for fitting.

the middle of the filament. Remember that the dipolar interaction energy decays as the third power of the inverse distance $(1/r)^3$. Let us apply this to the bead-spring model. Let E_0 be the interaction energy of nearest neighbours, then the contribution from the next beads down the line at twice the distance is one eigth of E_0 and so on. The total interaction energy is

$$E = E_0 \sum_{i=0}^{\infty} \frac{1}{i^3} \cong E_0 \cdot 1.2020 \ ,$$

corresponding to a correction of about 20%. An agreement with a deviation of only 1% from the value $1.2020E_0$ is reached after seven neighbours are considered. The rescaled energy $\tilde{H}^D$ introduced above tends to a constant value in the limit of $N \to \infty$ but for finite and small numbers of beads, effects from the filament ends get noticeable, as can be seen in figure 4.8. Accuracy to the degree of 1% for the dipolar energy is only reached after around 200 beads are included. This is because not only the two beads at the ends miss seven interaction partners, but six further beads on both sides do not contribute the same interaction energy as a dipole in the middle of the chain. That explains the discrepancy between the number of seven interaction partners required for each bead in the sum and the high number of N necessary for a filament of finite length to come close to the limiting value with an accuracy of 1%.

To summarize: in the following representation of bending, stretching and dipolar interaction energies the dimensionless parts after the dot have the desired property of being

independent of the number of beads (i.e. the filament length) if N is sufficiently large:

$$\begin{aligned} H^B = \quad & \tfrac{A}{L} \cdot \tilde{H}^B \quad && = \frac{A}{L} \cdot N \sum_i (1 - \hat{\mathbf{t}}_i \cdot \hat{\mathbf{t}}_{i+1}) \ , \\ H^S = \quad & \tfrac{1}{2} k \tfrac{L^2}{N} \cdot \tilde{H}^S && = \frac{1}{2} k \frac{L^2}{N} \cdot N \sum_i \left(\frac{l_i}{L} - \frac{l_0}{L} \right)^2 \ , \\ H^D = \quad & N^4 \tfrac{\mu_0 \chi^2 B^2}{4\pi L^3} \cdot \tilde{H}^D && = N^4 \frac{\mu_0 \chi^2 B^2}{4\pi L^3} \cdot \sum_{i \neq j} \frac{1 - 3(\hat{\mathbf{r}}_{ij} \cdot \hat{\mathbf{p}})^2}{\tilde{r}_{ij}^3} \frac{1}{N^4} \ . \end{aligned}$$

The pre-factors before the dot are now referred to the inherent bending energy $k_B T \frac{L_p}{L} = \frac{A}{L}$ to yield two dimensionless energy ratios that compare the magnitude of the characteristic stretching and dipolar interaction energies to the bending energy, respectively:

$$H^{S0} = \frac{\frac{1}{2} k \frac{L^2}{N}}{A/L} = \frac{k N^2 l_0^3}{2A} \ , \tag{4.22}$$

$$H^{D0} = \frac{\frac{\mu_0 \chi^2 B^2 N^4}{4\pi L^3}}{A/L} = \frac{\mu_0 \chi^2 B^2 N^2}{4\pi l_0^2 A} \ . \tag{4.23}$$

4.7.2 Rescaling the equation of motion

In the previous section, rescaled energies were introduced whose value is of order one independent of the length of the filament. However, when looking at the dynamics of a filament, not energies but forces and the equation of motion (4.15) for each single bead become relevant. Keeping this in mind, the following scaling factors for length, time and velocity will eventually lead to a dimensionless equation of motion:

$$\tilde{\mathbf{r}} = \frac{\mathbf{r}}{L} \ , \tag{4.24}$$

$$\tau = \omega t \ , \tag{4.25}$$

$$\dot{\tilde{\mathbf{r}}} = \frac{d}{d\tau} \tilde{\mathbf{r}} = \frac{1}{\omega L} \dot{\mathbf{r}} \ . \tag{4.26}$$

Remember that the total force acting on each bead k is given in the usual way by

$$\mathbf{F}_k = -\nabla_{\mathbf{r}_k} (H^B + H^S + H^D) \ .$$

With the energy scaling factor A/L and a reduced nabla operator $\tilde{\nabla} = L\nabla$ the appropriate scaling factor for forces is identified

$$\tilde{\mathbf{F}}_k = -\tilde{\nabla}_{\tilde{\mathbf{r}}_k} \tilde{H} = -\frac{L^2}{A} \nabla_{\mathbf{r}_k} H = \frac{L^2}{A} \mathbf{F}_k \ . \tag{4.27}$$

The only as yet unscaled quantities are the mobility tensors $\boldsymbol{\mu}_{ij}$ in equation (4.15). The scaling factor that first comes to mind is just $(6\pi\eta a)^{-1}$. Indeed, this factor makes a nondimensional tensor of the mobilities but is not entirely correct. On second thought, it makes sense to introduce a rescaling that contains some information about the hydrodynamic resistence of the whole filament rather than just that of a single bead. This is consistent with the approach taken so far: the force on each bead is derived from the total energy of the

system rather than from single-bead potentials. This reasoning justifies a correction in the form of a factor of L/l_0 that just gives the number of beads N. This leads to the following rescaled expression for the mobilities $\tilde{\boldsymbol{\mu}}_{ij}$:

$$\tilde{\boldsymbol{\mu}}_{ij} = 6\pi\eta\frac{a}{l_0}L\ \boldsymbol{\mu}_{ij}\ . \tag{4.28}$$

In this representation, the scaling factor can be understood to give a friction per length (one bead per linker) times the length of the filament. Of course, making use of the fact that in our treatment the bond length is held constant at three bead radii $l_0 = 3a$, it can also be written as $\tilde{\boldsymbol{\mu}}_{ij} = 2\pi\eta L\ \boldsymbol{\mu}_{ij}$; yet, this is somewhat less intuitive. Note that this rescaling strictly only applies in absence of hydrodynamic interactions which will become clear later on.

Using rescaled quantities only, the original equation of motion for bead i,

$$\dot{\mathbf{r}}_i = \sum_k \boldsymbol{\mu}_{ik}\cdot\mathbf{F}_k\ ,$$

now turns into

$$\dot{\tilde{\mathbf{r}}}_i = \frac{A}{6\pi\eta\frac{a}{l_0}\ \omega L^4}\sum_k \tilde{\boldsymbol{\mu}}_{ik}\cdot\tilde{\mathbf{F}}_k \tag{4.29}$$

$$= Sp^{-1/4}\sum_k \tilde{\boldsymbol{\mu}}_{ik}\cdot\tilde{\mathbf{F}}_k\ . \tag{4.30}$$

Equation (4.30) describes the coupled motion of the constituent beads of our model filament. The relevant quantity that has emerged in equation (4.30), turns out to be a dimensionless number:

$$Sp = \left(\frac{6\pi\eta\frac{a}{l_0}\ \omega L^4}{A}\right)^{\frac{1}{4}} \cong \left(\frac{6\pi\eta a\ \omega l_0^3 N^4}{A}\right)^{\frac{1}{4}}\ . \tag{4.31}$$

Sp shares a perfect formal analogy with the quantity derived in a somewhat different way by Wiggins and Goldstein [38, 39] for a slender, continuous and inextensible filament

$$Sp^0 = \left(\frac{\zeta_\perp\omega L^4}{A}\right)^{\frac{1}{4}}\ ,$$

where $\zeta_\perp$ is the viscous resistance coefficient per length of a long cylinder moved orthogonal to its main axis that is used in slender-body theory. This quantity Sp dubbed "Sperm number" by Lowe and Lagomarsino [26, 23] is derived by rescaling the dynamic equation of an elastic rod in section 2.3.

For constant bead radius a and bond length l_0, the multitude of parameters of the bead-spring model reduces to just three relevant dimensionless quantities that determine the filament's dynamics, namely H^{S0}, H^{D0} and Sp. Varying the material parameters and the number of beads but keeping these three numbers constant will lead to the same response from the filament. The Sperm number is the length of the filament scaled by the viscoelastic penetration length $l_{\tilde{\nu}}$ (see section 2.3) and gives the ratio of viscous forces to forces resisting bending:

$$Sp = \left(\frac{\text{friction forces}}{\text{bending forces}}\right)^{\frac{1}{4}} = \frac{L}{l_{\tilde{\nu}}}\ .$$

A fourth important parameter connected to the geometry of actuation will have to be introduced. But first, let us put the predictions made so far to a test!

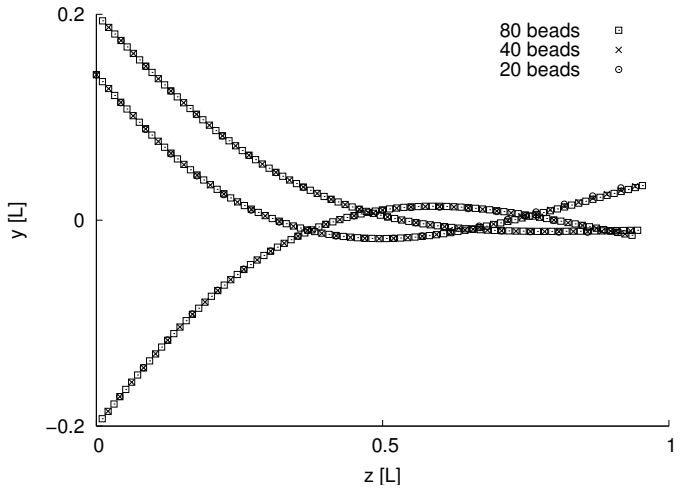

Fig. 4.9: Enforced wiggling of the left end as described in the text. In this plot, no hydrodynamic interactions are included, explaining the near perfect congruence of the three snapshots taken for different length filaments. The snapshots are printed in reduced length at the same points of reduced time.

4.7.3 Testing the scaling invariance

Interesting implications arise from the rescaling performed in the previous section. Remember that stretching was mainly introduced for numerical reasons as a simple way of keeping the filament at a nearly constant length. Thus, H^{S0} is not as interesting a parameter as H^{D0} and Sp, which describe the importance of dipole interactions and friction forces relative to bending, respectively.

It is easy to convince oneself that for constant N all material parameters in H^{S0}, H^{D0} and Sp can be modified in such a way that keeps H^{S0}, H^{D0} and Sp constant and an identical trajectory for each bead will ensue. The only non-trivial parameter is the overall length given by the number of beads. Due to the small length of filaments that are computationally viable, the scaling of bending and dipolar forces is not quite exact, as we have seen in the preceding paragraphs. Moreover, the neglect of hydrodynamic interactions in the derivation of the Sperm number also gives rise to some short-comings in the predictive power of Sp. How big these restrictions are, will be investigated in the following.

In order to test the quality of the predictions made by simulations, let us first look at the Sperm number separately in absence of dipolar interactions. Let the initial state of the filament be straight and aligned along the z-axis with the first bead in the origin of the coordinate system. Then the the boundary conditions are:

$$\begin{aligned} \mathbf{r}_i(t=0) &= (0, 0, [i-1]l_0) \ , \\ \mathbf{r}_1(t) &= (0, \alpha L \sin(\omega t), 0) \ . \end{aligned}$$

As before, l_0 and L denote the bond length and the filament length, respectively. α gives the amplitude of wiggling as a fraction of the filament length and ω the frequency.

Figure 4.9 shows snapshots for three different filament lengths with $N = 20, 40$ and 80. To offset different N in Sp and H^{S0}, the spring constant k and the frequency ω are adjusted as necessary. The snapshots shown are printed with the length scaled by L and at identical

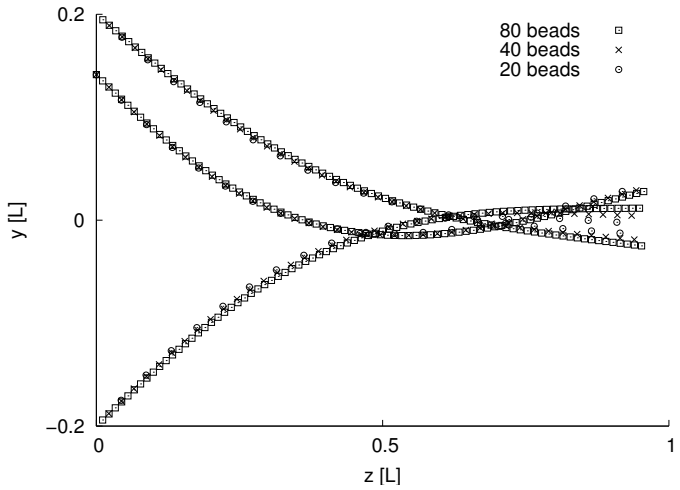

Fig. 4.10: Enforced wiggling of the left end as in figure 4.9. In this case, however, hydrodynamic interactions on the Rotne-Prager level are switched on.

rescaled times τ. The wiggling amplitude is set to $\alpha = 0.2$ with a wiggling frequency of $\omega = 10$ Hz. These simulation runs do not consider hydrodynamic interactions. Congruence on the left end is, of course, no surprise, as it is just given by the boundary condition of the first bead. Yet, the overall congruence is excellent with only a small visible deviation at the right both in x and y-direction. There are two different reasons for this: The cause for deviations in x-direction simply is that the scaling uses N as indicator of the length, whereas the length of the filament is really given by the number of linkers $L = (N-1)l_0$. Deviations in y-direction must stem from the rescaling of the bending energy since the scaling of the stretching energy is analytically exact, whereas finite length effects from the rescaling of the bending energy for $N \lesssim 100$ are visible in figure 4.7.

The effect of hydrodynamic interactions is visible in figure 4.10. Obviously, there is still a good level of agreement, albeit the striking congruence is lost. This comes as no surprise and has already been mentioned above. The Sperm number introduced in equation (4.31), as the one for the continuous filament introduced by Goldstein and Wiggins, does not consider hydrodynamic interactions.

Practically much more important than exact congruence, however, is the typical response of a filament subject to a time-varying constraint. Even when hydrodynamic interactions are included, the extinction length along the filament for a given disturbance at one end does not significantly change implicating that basically the same physics will take place.

Having thus established the Sperm number as the key quantity in determining the characteristics of filament dynamics, let us look at the essential parameters in Sp. Sp is a function of the filament length and the oscillation frequency, as well as the bending stiffness and friction coefficient, the latter two of which are not easily modifiable in an experimental system. The driving frequency is well suited for distinguishing between different regimes of beating of a filament; although identical results can be obtained by varying the length (see figure 2.8 in section 2.3). Figure 4.11 shows snapshots at regular time intervals of the same filament driven by three different frequencies. For each of these frequencies a different characteristic motion of the filament is clearly visible: In the uppermost plot, there is hardly any bending at all and

the filament pivots up and down similar to a rigid rod. In the middle, however, both bending and friction forces are more or less equally relevant, leading to noticeable bending along the entire length of the filament. The plot below shows heavy damping of the impressed wave by viscous forces.

At last, dipole interactions are also included. An actuation of the filament is achieved by applying a time-varying magnetic field rather than by enforced motion of one of the filament ends. Naturally, this produces symmetric deformations of the chain and a propulsive effect is prohibited by symmetry. The magnetic field has constant field strength but a sinusoidally modulated orientation according to

$$\mathbf{B}(t) = B_0 \begin{pmatrix} 0 \\ \sin(\varphi(t)) \\ \cos(\varphi(t)) \end{pmatrix} , \tag{4.32}$$

$$\varphi(t) = \varphi_{max} \sin(\omega t) , \tag{4.33}$$

the geometry of which is illustrated in figure 4.12. The additional parameters for $N = 20$ were set to $B_0 = 0.08$ T and $\varphi_{max} = 50°$ at a wiggling frequency of $\omega = 50$ Hz. In order to keep H^{D0} constant the value of B_0 was adjusted.

The plot in figure 4.13 shows snapshots in reduced length at concurrent moments of rescaled time without hydrodynamic interactions. The level of congruence is clearly less than for the nearly perfect match in figure 4.9. The rescaling of the magnetic field was found to be asymptotically correct for large N, yet for small numbers of N up to around 200 deviations bigger than one percent were found. In fact, at $N = 80$ the relative error is still around 2.5% whereas at $N = 20$ it is roughly 13% (see figure 4.8). This slow but monotone convergence is reflected here as a closer glance reveals: the 40- and 80-bead chains match much more closely than the 20- and 40-bead chains.

Interestingly enough, the inclusion of hydrodynamic interactions in figure 4.14 has a bigger influence on the tilting angle of the chains as a whole than on the fanning out between filaments of different length, albeit these deviations are more pronounced than in figure 4.13. It is immediately noticeable that all chains seem to have overcome some viscous resistance and are hence free for more tilting with respect to the z-axis. This seems to be especially true when the number of beads in a chain increases which illustrates the collective effect of hydrodynamic interactions. Letting more beads move into the same direction at comparable velocities reduces the viscous drag on every single one of them. Unlike in cycling races, however, it is not necessary to be more or less behind a moving obstacle but it suffices to be simply nearby.

We note that the characteristic response of the chain to an actuation by a magnetic field is still scaling invariant to a decent approximation, even though the dipolar scaling of finite length filaments and hydrodynamic interactions both somewhat corrupt the visible congruence of snapshots in a direct comparison. Nonetheless, keeping the purpose of propulsion and fluid transport in mind, the data do not give rise to the expectation of a radically different qualititative and even quantitative behaviour when the length of the filament is changed as long as the Sperm number and H^{D0} remain constant.

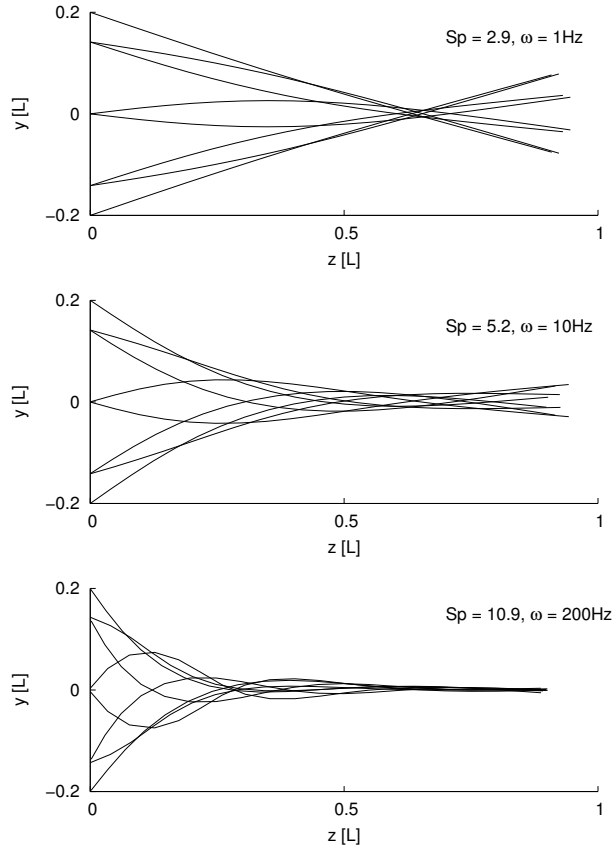

Fig. 4.11: Wiggling of a 20 bead filament (see text). The difference between the three plots is in the oscillation frequencies. For low frequencies we have a turning of a stiff filament similar to a rigid rod. In an intermediate frequency range, the whole rod assumes a state of bending while the disturbance decays fast at very high frequencies. Then, the right end of the filament no longer participates in the wiggling motion.

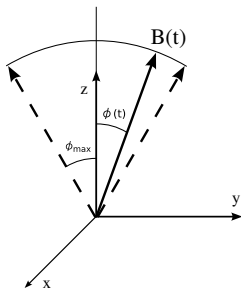

Fig. 4.12: The vector of the magnetic field has a constant magnitude but a time-varying direction. It moves in the yz-plane, wiggling about the z-axis.

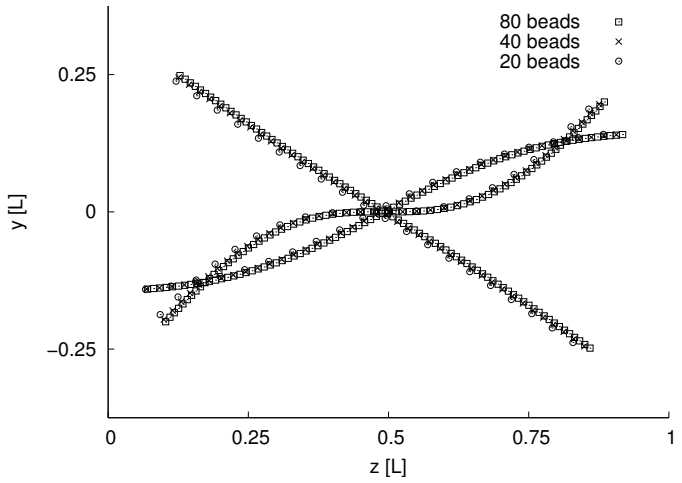

Fig. 4.13: Actuation of the filament by an external magnetic field without hydrodynamic interactions as described in the text. As before, the filaments are printed in reduced length and at concurrent instants of rescaled time. The 40- and the 80-bead chains match better than the 20- and the 40-bead ones.

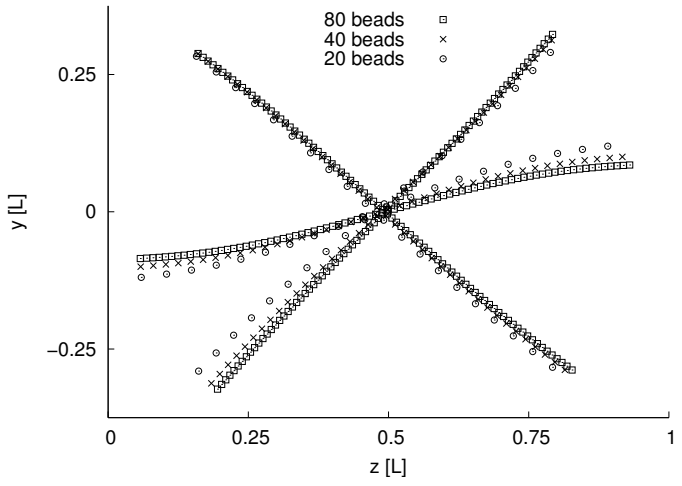

Fig. 4.14: Magnetically actuated filament as in figure 4.13 with the difference that hydrodynamic interactions are included, which make quite a difference here.

Chapter 5

One-armed swimmer

The dynamics of artificial filaments has been explored in some depth in the previous chapter. So let us devise a model swimmer that makes actual use of such a filament. A straightforward and yet interesting idea is that of an one-armed swimmer, i.e., a filament attached to a larger spherical bead. On the one hand, it is a very simple model relying on the propulsive power of wiggling filaments similar to the ones treated analytically in section 2.3. On the other hand, the one-armed swimmer is quite a realistic implementation of an artificial micro-swimmer that has recently been realized experimentally [11].

5.1 Model of the one-armed swimmer

A filament is attached to a larger bead that is not paramagnetic and serves as the "cell head" of the swimmer. The large sphere will hereafter be referred to simply as the head. The diameter of the head is about an order of magnitude larger than the beads which build the filament.[1] The connection between the first bead of the filament and the head has the same properties as the linkers in the filament as far as bending and stretching elasticity are concerned. Since the linker connects the centres of the spheres, its length is chosen so that the surface-to-surface distance is one radius a of the smaller beads.

The filament is driven by the magnetic actuation introduced in chapter 4. Since the field stays in the yz-plane, the motion of the one-armed swimmer is restricted to the same plane. As initial configuration, the filament is aligned with the direction of the magnetic field $\mathbf{B}(t = 0)$ along the z-axis. $\mathbf{B}(t)$ then wiggles about the z-axis. The angle enclosed by z-axis and $\mathbf{B}(t)$ is $\varphi(t) = \varphi_{max} \sin(\omega t)$ as illustrated in figure 5.1. We use an angular wiggling amplitude φ_{max} of around 45 degrees. How the properties of the one-armed swimmer depend on φ_{max} is explicitly studied later in this chapter.

Magnetic actuation of a free filament produces symmetric deformations (see figure 4.14) that do not lead to any net motion. The situation is different when a viscous load in the form of the head is attached; then propulsion can indeed be achieved.

Note also that in our model hydrodynamic interactions are necessary to generate motion. If only self-mobilities are considered, no motion should occur since then the previously introduced friction coefficients $\zeta_\perp$, $\zeta_\parallel$ of the filament (see sections 2.3, 4.2) are identical and the mobility matrix of the filament is isotropic precluding net propulsion as was found in section

[1] In parameter set I we have $a_0 = 8a$, where a_0 is the radius of the head and a the radius of the beads in the filament. In parameter set II we use $a_0 = 5a$.

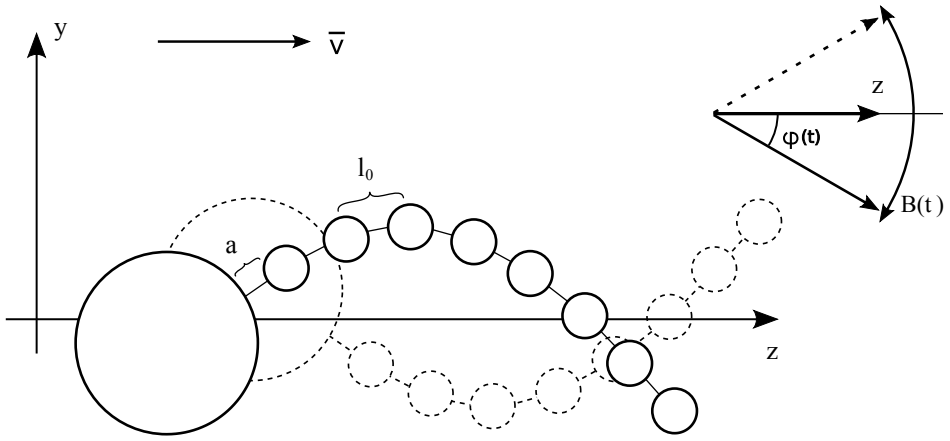

Fig. 5.1: Schematic drawing of the one-armed swimmer. The surface-to-surface distance between all beads has the same equilibrium value a. Field and swimmer wiggle around the z-axis and the net swimming velocity $\overline{\mathbf{v}}$ is parallel to the z-axis. Note that locomotion occurs into the direction of the tail of the swimmer.

2.3. This fact has also been verified by simulations. The simulation data presented in the following include hydrodynamic interactions in the Rotne-Prager approximation (3.48). For the interaction with the larger head, the expression (3.49) for unequal spheres is used.

5.2 Velocity and Efficiency

The net velocity of the swimmer is measured by time-averaging the velocity of the head over a multiple of the actuation cycle:

$$v = |\overline{\mathbf{v}}| = \frac{1}{nT} \int_{rT}^{(r+n)T} \mathbf{v}_0(t)\mathrm{d}t \ . \tag{5.1}$$

Here, T is the time required for running one complete actuation cycle ($T = \frac{2\pi}{\omega}$), n gives the number of cycles to average over, r sets the time when the averaging starts and $\mathbf{v}_0$ is the velocity of the zeroth bead, i.e., the head.

Typically, we start with $r = 3$ or larger and average over ca. $n = 5$ subsequent cycles depending on the value of Sp. This approach is necessary because the initial alignment of field and filament in z-direction is a special state that does not reoccur later in the simulation. Once the field starts wiggling, the filament tries to follow by realigning but it is generally no longer straight or parallel to the field vector $\mathbf{B}(t)$. Yet, after some time a limit cycle is reached. This means that after deduction of the net displacement per cycle, each bead moves on a well-defined and closed trajectory. It is only then, that the averaged swimming velocity is strictly parallel to the z-axis and can be safely measured. However, the time it takes to reach the limit cycle depends on the Sperm number. For $Sp \approx 1$, i.e., at low actuation frequencies, the filament manages to follow the field rather well and almost no initial effects persist into the second cycle. For $Sp \gg 1$, however, corresponding to high driving frequencies, even an approximate limit cycle might not have been assumed after ten or more cycles.

Equation (5.1) can be replaced by a simpler version by using the net displacement of the head $\mathbf{r}_0(t') - \mathbf{r}_0(t' + nT)$ during n cycles:

$$v = \frac{1}{nT}|\mathbf{r}_0(t') - \mathbf{r}_0(t' + nT)| \ . \tag{5.2}$$

This is valid for an arbitrary value of t' as long as t' is big enough for the system to have reached the limit cycle. Since the projection of $\mathbf{v}_0(t)$ onto the y-direction cancels out when averaged over a full cycle (once the limit cycle has been reached), it even suffices to take the difference of the z-components of $\mathbf{r}_0(t')$ and $\mathbf{r}_0(t' + nT)$ in equation (5.2). However, this is only possible when the net swimming is strictly along the z-axis.

The head of the one-armed swimmer is dragged rather than pushed by its tail. This swimming direction is opposite to what one would intuitively expect when thinking of *spermatozoa* whose swimming direction is into the direction of their heads. As was pointed out in section 2.3, the direction of swimming is opposite to the direction of the waves propagating along the filament. In the case of *spermatozoa*, the waves start at the head and propagate towards the free end of the tail [26]. This is different in our model of the one-armed swimmer since the free end is also the more "active" one which undulates with larger amplitude. The motion of the filament can be best described as a kind of mixture of a scooping and a paddling motion.[2] The simulations further show that in principal a reversal of direction is possible, when the head is made "active" by participating in dipolar interactions. Due to its bigger size, both the dipolar contribution and the viscous drag play important roles in determining which end is "more active". Therefore, a reversal of direction does not necessarily happen with a superparamagnetic head. For special parameter combinations, though, a swimming mode where the tail follows the head has been observed.

In order to study the efficiency of propulsion, a suitable efficiency measure needs to be defined. As the energy necessary for motion is transferred to the swimmer through the magnetic field, which we consider to be homogenous and of constant strength, the energy input is not directly accessible. What can be done, however, is to compare the rate of energy dissipated by the net swimming motion of the head to the time-averaged rate of the totally dissipated energy of the tail

$$\xi = \frac{6\pi\eta a_0 v^2}{\overline{\sum_{i\geq 1} \mathbf{F}_i \cdot \mathbf{v}_i}} \ . \tag{5.3}$$

The numerator of equation (5.3) gives the rate at which energy would be dissipated by motion of the head if it was moving straight with the time-averaged velocity $v = \overline{\mathbf{v}}_0$. In order to evaluate $\overline{\mathbf{F}}_0 \cdot \overline{\mathbf{v}}_0$, where $\mathbf{F}_0$ is the force needed to drag the sphere through the fluid at velocity v_0, the Stokes relation for an isolated sphere $\overline{\mathbf{F}}_0 = 6\pi\eta a \overline{\mathbf{v}}_0$ has been used. The denominator of equation (5.3) gives the time-averaged rate of energy dissipated by motion of the tail. $\mathbf{F}_i$ denotes the total force on bead i and $\mathbf{v}_i$ is its velocity.

Note that absolute values of the efficiency (5.3) should be interpreted with care for several reasons. First, it is not quite correct to use the Stokes relation for the head. The real resistence of the head is, of course, given by considering additional hydrodynamic interactions with the other beads. However, as the head is significantly larger than the beads of the tail, this

[2] Dreyfus *et al.* have also tried to identify a wave propagating towards the head with the help of stroboscopic snapshots [11]. However, the observed motion of the filament is not well approximated by a wave in our opinion.

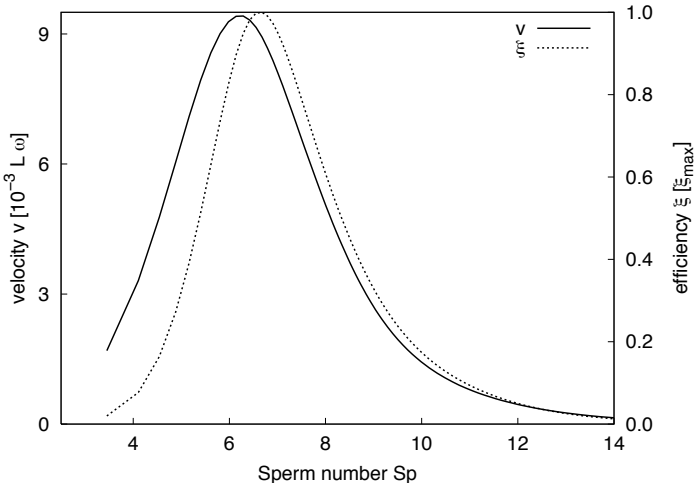

Fig. 5.2: The rescaled swimming velocity $\tilde{v} = v/(\omega L)$ and the efficiency ξ according to equation (5.3) as functions of the Sperm number Sp. The efficiency is given in units of ξ_{max} which is $\xi_{max} = 2.27 \cdot 10^{-3}$. The scaled value of the magnetic field is $B_s = 5.76$ [see equation (5.4)] and the data has been obtained with parameter set II.

correction should not exceed the single-digit percentage range. Secondly, the tail does not only drag the passive viscous load of the head but a substantial part of the propulsive power developed is used for locomotion of the tail itself.

Following the scaling laws derived in chapter 4, the generic way of presenting the swimming velocity is to consider the rescaled velocity $\tilde{v}$ as a function of the Sperm number Sp. Remember that the rescaled velocity is given by $\tilde{v} = \frac{v}{L\omega}$ and the Sperm number Sp is also a function of ω. So, if $\tilde{v}$ is plotted as a function of Sp (e.g. as in figure 5.2), the ordinate and the abscissa of such a plot are not independent of one another. Nevertheless, we shall present most of the results in this naturally rescaled way. Yet, whenever one has a particular swimmer with given mechanical properties and filament length L in mind, the absolute swimming velocity v achieved by that swimmer as a function of Sp, or equivalently the frequency of actuation ω, may also be of interest. Furthermore, there are some instances for which qualitative features with respect to a certain question are more easily visible if shown in absolute rather than rescaled units of the velocity. However, note that values of the absolute velocity do depend on the specific parameters of the system and cannot be directly compared to another swimmer with different parameters.

Figure 5.2 shows the rescaled velocity and the efficiency as functions of Sp. As we expect from similar studies in section 2.3, both velocity and efficiency have a distinct maximum, which here occurs for values of Sp around 6.3 and 6.7, respectively. For $Sp < 4$, the velocity and the efficiency become comparatively small and approach zero as should be the case for $Sp \to 0$. To the right of the respective maxima, the curves drop quickly with increasing Sp. Note that running simulations for $Sp \to 0$ requires either the frequency ω or the filament length to go to zero. Lower frequencies are connected to longer times $T = \frac{2\pi}{\omega}$ per simulation cycle while arbitrarily short filaments have no discretized representation. For these reasons, the limiting behaviour of $Sp \to 0$ has not been investigated.

Let us also look at the absolute velocity as a function of Sp to see what the differences

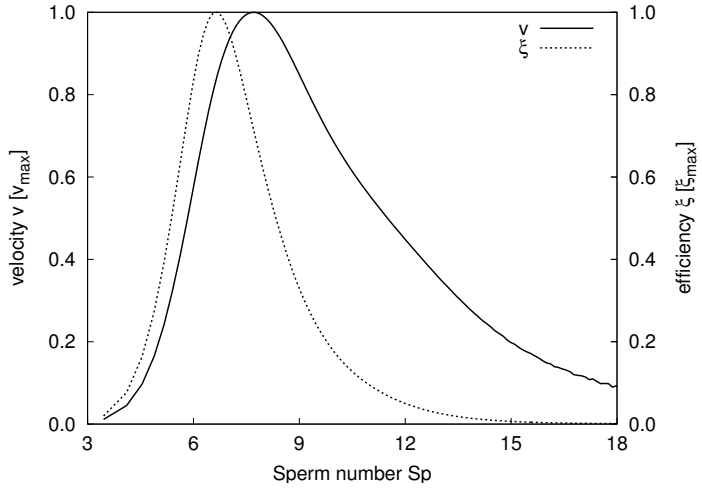

Fig. 5.3: Swimming velocity and efficiency versus the Sperm number. Both curves are given in units of the respective maximum values which are $v_{max} = 5.56 \cdot 10^{-5}$ m/s and $\xi_{max} = 2.27 \cdot 10^{-3}$. This plot shows the same data as figure 5.2 with the difference that the absolute swimming velocity is given rather than the rescaled one. The main difference is that the velocity peak is situated at a larger value of Sp and drops much slower than it does in figure 5.2.

between the two above-mentioned ways of plotting the velocities are. Figure 5.3 shows the same data as figure 5.2 with the velocity given in absolute units of v_{max}. The maximum of the velocity now moves to larger values of Sp at around 7.7. Moreover, the velocity drops at a much slower pace, meaning high (absolute) velocities can be realized in an energetically very inefficient way, since velocity and efficiency curve no longer match particularly well. The close match of rescaled velocity and efficiency in figure 5.2 is really a remarkable aspect. We try to give a qualitative argument for the congruence: per definition the rescaled velocity is related to the propulsive power of the filament per length and cycle. While propulsion always entails a dissipation of energy, the distinction between an efficient and an inefficient swimmer is in the ratio of dissipated energy that leads to directed motion compared to the totally dissipated energy. However, reciprocal motion as well as wiggling only at the ends of an unnecessarily long filament consumes energy but does not lead to efficient propulsion. Therefore, it comes as no surprise that the filament reaches its highest propulsive power at around the same value of Sp at which the biggest part of the dissipated energy is converted into propulsion.

What does the motion of the one-armed swimmer actually look like? Figure 5.4 shows snapshots of the shape of the filament taken at different points of time within one actuation cycle for values of $Sp = 3$, 6 and 12. The situation for the lower ($Sp = 3$) and intermediate ($Sp = 6$) value of Sp is similar to the snapshots shown in figures 2.8 and 4.11: at low Sperm number $Sp \lesssim 3$ only very little bending occurs and the motion is close to the regime of a reciprocal motion where the scallop theorem applies. For $Sp \approx 6$, a conspicuous state of bending is assumed that eludes the scallop theorem and generates propulsion. At higher Sperm numbers, however, the amplitude of the wiggling decreases strongly and only the ends perform some wiggling that is not at all efficient in terms of its propulsory effect.

The maximum of the velocity at around $Sp = 6$ is in fairly good qualitative agreement with the predictions from Wiggins *et al.* [38] and Lagomarsino [23] although both consider

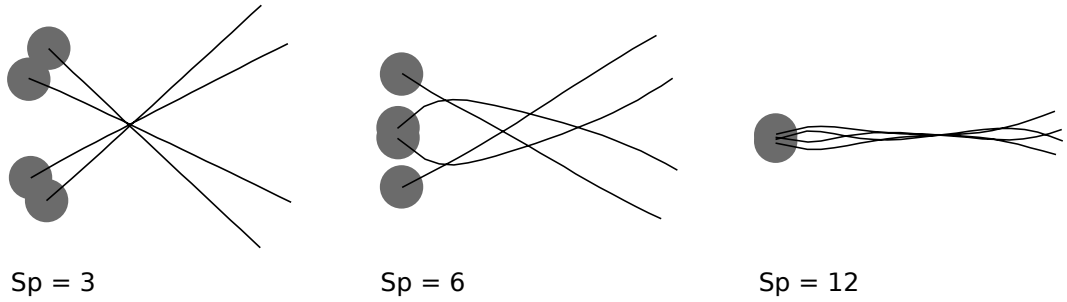

Fig. 5.4: Stroboscopic pictures of the shape of the one-armed swimmer taken at different points of time within one actuation cycle for values of $Sp = 3$, 6 and 12. The swimming displacement between subsequent snapshots is not shown.

quite different swimmers consisting of a passive filament with no viscous load.[3] Yet, what seems to be important is not the precise geometrical deformation but rather the amount of bending possible for a given filament and actuation. As long as the viscous load is big enough to make sure the wiggling is not symmetric about the middle of the filament, we may assume the absolute values of velocity and efficiency to depend on the viscous resistance of the load but not necessarily on Sp to the same extent. The difference between a passive and an active filament deserves some more attention.

Before we see what happens when the strength of the actuation is varied, remember that we have introduced three dimensionless quantities, H^{S0} (4.22), H^{D0} (4.23) and the Sperm number Sp (4.31) that fully characterize the filament in section 4.7. As in section 4.7.3, we do not consider H^{S0} to be an interesting parameter since the stretching elasticity was introduced mostly for numerical reasons. However, H^{D0}, which describes the relative importance of dipolar interactions and bending, will be an important parameter. Since $H^{D0} \sim \mathbf{B}^2$ [see equation (4.23)], we introduce the rescaled magnetic field B_s

$$B_s = \sqrt{H^{D0}} \; . \tag{5.4}$$

Figure 5.5 shows velocity and efficiency curves for different values of the rescaled magnetic field B_s. While the same qualitative features exist for the same data plotted with rescaled velocities, they are much less conspicuous. Therefore, velocities are given in absolute units for better visibility. Besides growing values of the velocities, all peaks move to larger Sperm numbers for increasing B_s. In contrast to the velocity, the efficiency does not increase with B_s. It remains more or less at the same level with a slight drop for the strongest magnetic field B_s shown. To understand why velocity and efficiency maxima apparently move to higher values of Sp with increasing (rescaled) field strength, look again at the definition of the Sperm number (4.31)

$$Sp = \left(\frac{6\pi\eta \frac{a}{l_0} \, \omega L^4}{A} \right)^{\frac{1}{4}} \; .$$

As has been discussed in section 4.4, a chain of dipoles favours a straight configuration for energetic reasons. Thus, bending is resisted not only by the bend stiffness A but also by

[3] The maximum of the scaling function $Y(Sp)$ connected to the swimming velocity is at around $Sp = 4$ (see section 2.3).

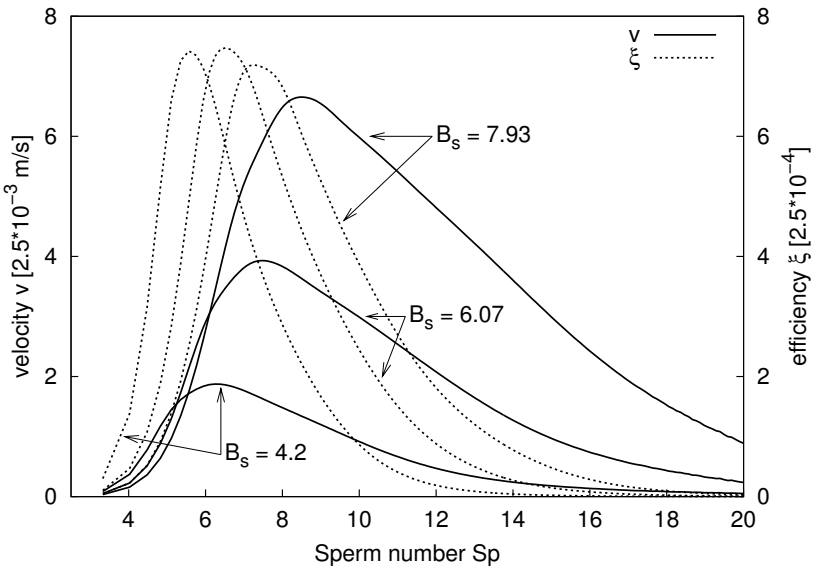

Fig. 5.5: Velocity and efficiency for different values of the rescaled magnetic field B_s. The velocities are given in units of m/s for a swimmer using parameter set I. For increasing B_s the peaks move to higher values of Sp because the forces that resist bending grow stronger (see text). Furthermore, the swimming velocities increase with B_s.

dipolar interactions, so that the *effective bend stiffness* increases with the strength of the dipolar interactions.[4] But if $A_{eff} > A$ then $Sp(A) > Sp(A_{eff})$, so this explains why the position of the maximum in terms of $Sp(A)$ depends on B_s. Figure 5.6 shows the velocity as a function of both B_s and Sp and the same effect can be seen nicely.

5.3 Dependence on the angular wiggling amplitude

So far we have used the respective angular wiggling amplitudes ("wiggling angles") $\varphi_{max} = 45°$ for the data in figures 5.3, 5.2 and $\varphi_{max} = 57°$ for the data in figures 5.5, 5.6. As will be shown in the following, the wiggling angle does not influence the qualitative features when it stays below a maximum value, while the absolute values of velocity and efficiency depend on φ_{max}.

In figure 5.8 the rescaled velocity is plotted as a function of the wiggling angle φ_{max} in the interesting Sperm number range between 5 and 11. The rescaled velocity increases for larger wiggling angles but the position of the maximum as a function of the Sperm number is essentially unaltered. A slight tendency favouring smaller Sperm numbers for larger wiggling angles can be discerned. This is probably due to the fact that a larger wiggling angle leads to enhanced bending at a lower frequency compared to a smaller wiggling angle. In this sense, faster wiggling at smaller angles is equivalent to slower wiggling at larger angles. Nevertheless, the optimal Sperm number does not seem to significantly depend on φ_{max}.

We need not stop at wiggling angles of 60°. Figure 5.9 shows an intersection of plot 5.8

[4]The dipolar potential cannot be seen as a bending potential in a strict way. However, dipolar forces also straighten the filament, so that for a qualitative discussion it is illustrative to speak of an increased effective bend stiffness even if this is formally not quite correct.

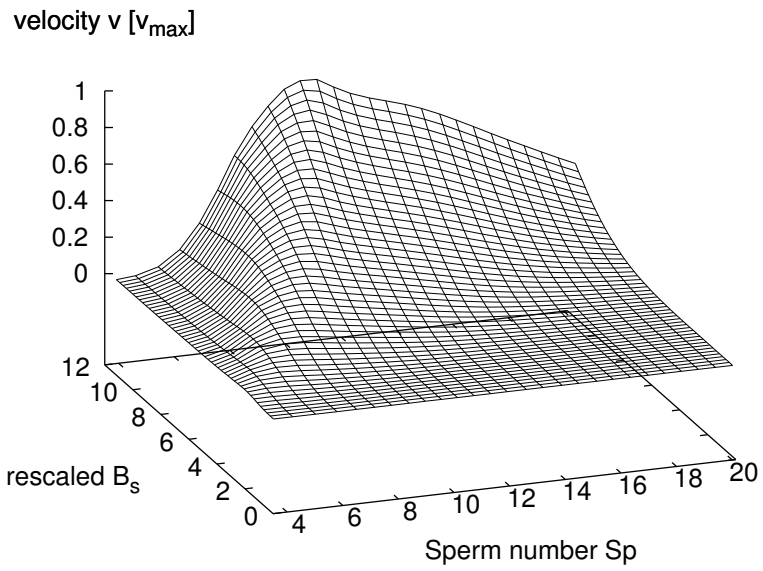

Fig. 5.6: The swimming velocity v as a function of Sp and the rescaled magnetic field B_s. The absolute maximal velocity goes up with increasing magnetic field strength but at the same time the maximum occurs at an ever larger Sperm number Sp. This effect is present but less visible when the rescaled velocity is plotted. The data is from the same swimmer as in figure 5.5.

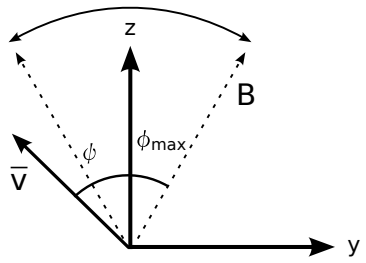

Fig. 5.7: Definition of the angular wiggling amplitude φ_{max} and the swimming angle ψ.

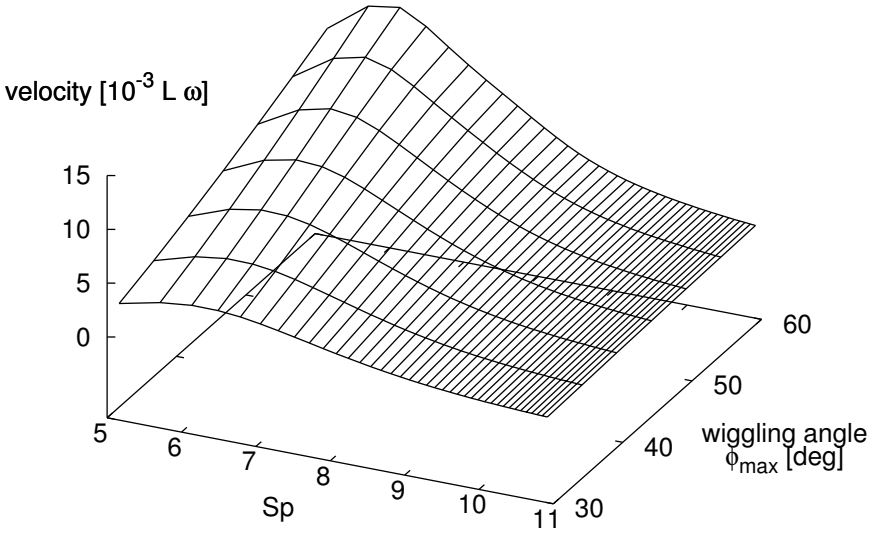

Fig. 5.8: The rescaled velocity $\tilde{v} = v/(L\omega)$ is plotted as a function of the maximal wiggling angle φ_{max} and Sp for a swimmer using parameter set II.

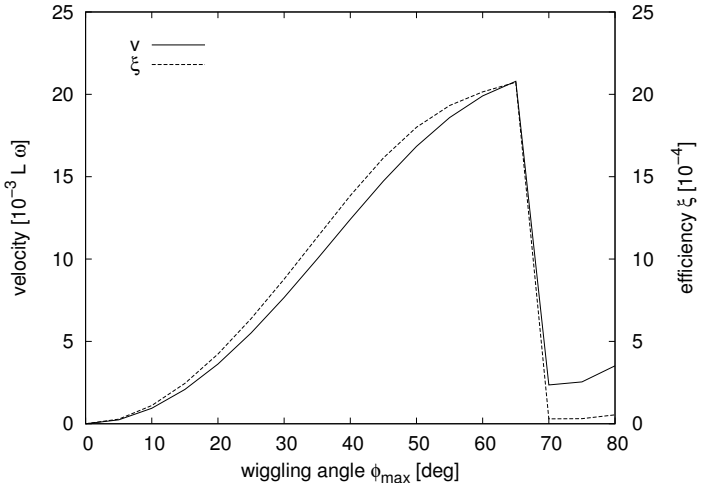

Fig. 5.9: Rescaled velocity $\tilde{v}$ and efficiency ξ are plotted as functions of the maximal wiggling angle φ_{max} at the Sperm number $Sp = 6.1$ for the same swimmer used in figure 5.8. Note the drastic drop in velocity and efficiency for $\varphi_{max} \geq 70°$.

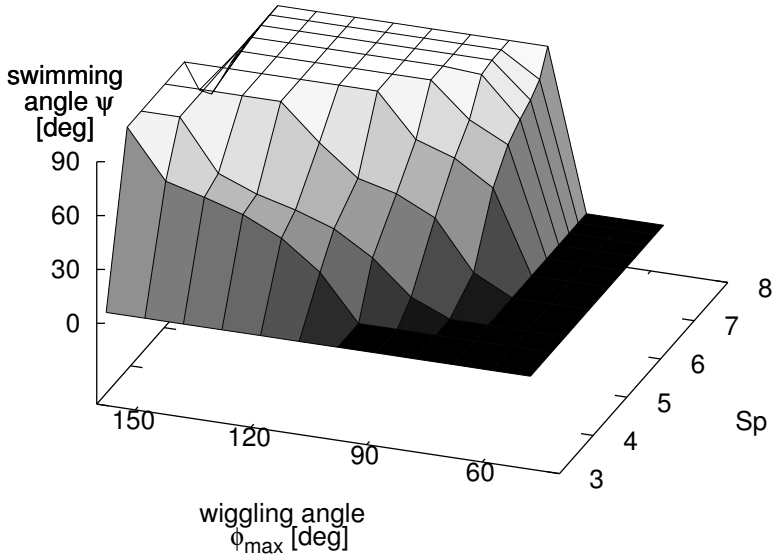

Fig. 5.10: The swimming angle ψ as defined in figure 5.7 is shown against the wiggling angle φ_{max} and the Sperm number Sp. In the region where $\varphi_{max} < 60°$ (not fully shown), ψ is zero, i.e. the swimming direction is parallel to the z-direction, independent of Sp. For $\varphi_{max} \in [60, 150]$ degrees there is a transitional regime or swimming in the y-direction depending on Sp. When $\varphi_{max} = 180°$ is approached, swimming angles parallel and anti-parallel to the z-axis occur. The Sperm number range covered is restricted to the interval of main interest. Lower Sperm numbers corresponding to lower frequencies are computationally expensive whereas at higher frequencies the limit cycle of filament motion is often not reached after hundreds of actuation cycles. The data have been obtained for parameter set I.

where Sp is held constant close to the optimal value of $Sp \approx 6$. Yet, in this plot a sharp drop of the velocity for $\varphi_{max} > 65°$ is visible.[5] This is the point where the time-averaged velocity of the head, $\overline{\mathbf{v}}$, is no longer parallel to the z-axis.

We define the angle enclosed by $\overline{\mathbf{v}}$ and the z-axis as swimming angle ψ (see figure 5.7). The swimming angle ψ as a function of Sp and the wiggling angle φ_{max} is shown in figure 5.10. While the motion is always in z-direction for $\varphi_{max} \leq 60°$, three different regimes depending on the Sperm number need to be distinguished for $\varphi_{max} > 60°$ degrees.

- At low Sperm numbers $Sp \lesssim 3$, the swimmer pivots like a rigid rod with only very small flexible corrections. In this case hardly any net displacement is possible since the motion is by and large reciprocal. Whatever tiny net motion remains from the flexible corrections is in the z-direction.

- At intermediate Sperm numbers $3 \lesssim Sp \lesssim 12$ considerable bending occurs but the filament does not manage to quite follow the field. This is particularly true for large wiggling amplitudes.

  In the interval $60° < \varphi_{max} < 160°$, the limit cycle produces a motion whose swimming

[5] The precise angle at which the drop occurs depends on Sp. However, we will later argue that it should be strictly 70 degrees.

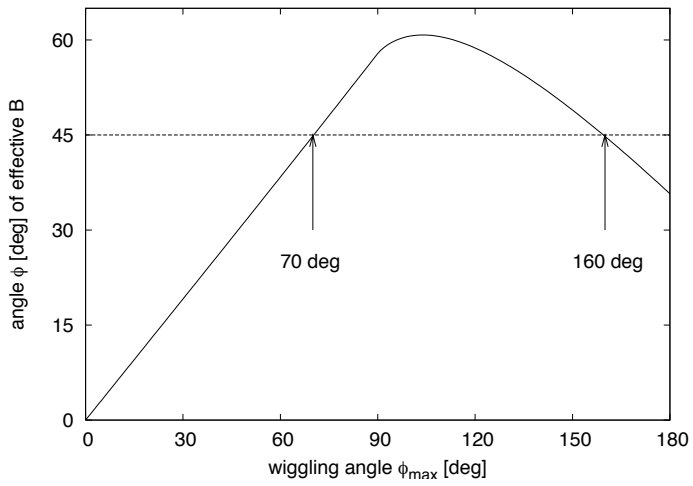

Fig. 5.11: This plot shows the angle enclosed by the time-averaged magnetic field of equation (5.5) and the z-axis as a function of the wiggling angle φ_{max}. The intersections with the horizontal line at 45° define an interval $[70, 160]$ of φ_{max} in which $\mathbf{B}$ spends more time at angles $\varphi > 45°$ than the other way round.

angle ψ is between 0° and 90°. The swimming angle is skew because symmetry is broken during the transition to the limit cycle. When the simulation first starts, both filament and $\mathbf{B}$ are parallel and tilt to the right at different speeds. When the field reverses, the filament lags behind and tilts even further to the right before it starts to go back to the left. It does not, however, manage to tilt as far to the left as it just did to the right, before it is again overtaken by the field back on its way to the right. This is the beginning of an asymmetry that builds up over many cycles until an asymmetric limit cycle is finally reached. The limit cycle does produce a net displacement, albeit at a skew angle ψ and low efficiency. Behaviour of this kind occurs in a roughly triangular region in plot 5.10. We see again that with regard to the direction of swimming there is some degree of equivalence of (i) wiggling with larger amplitude or (ii) wiggling at larger Sperm number, i.e., with faster frequencies.

At large enough wiggling amplitudes another mode of motion is assumed that leads to an average velocity orthogonal to the z-axis. This is described in the following paragraph.

- The transition from a parallel to an orthogonal swimming direction relative to the z-axis becomes sharper with increasing Sperm number. For $Sp \gg 6$ there is hardly any transitional regime and the transition occurs at a wiggling amplitude φ_{max} somewhere between 65° and 70°. Hence for large Sperm numbers and $\varphi_{max} \geq 70°$, swimming orthogonal to the z-axis is the prevalent picture before movement parallel or anti-parallel to the z-axis occurs when φ_{max} approaches 180°.

  How can the orthogonal swimming be explained? For large angular velocities of the field, the filament cannot even partially align with the field because a reorientation of it is slowed down by its viscous drag. Whether or not the filament succeeds in following the field depends both on the angular frequency, i.e., on Sp, and on the wiggling angle φ_{max}. For a pair of Sp and φ_{max} for which the filament cannot move fast enough to be

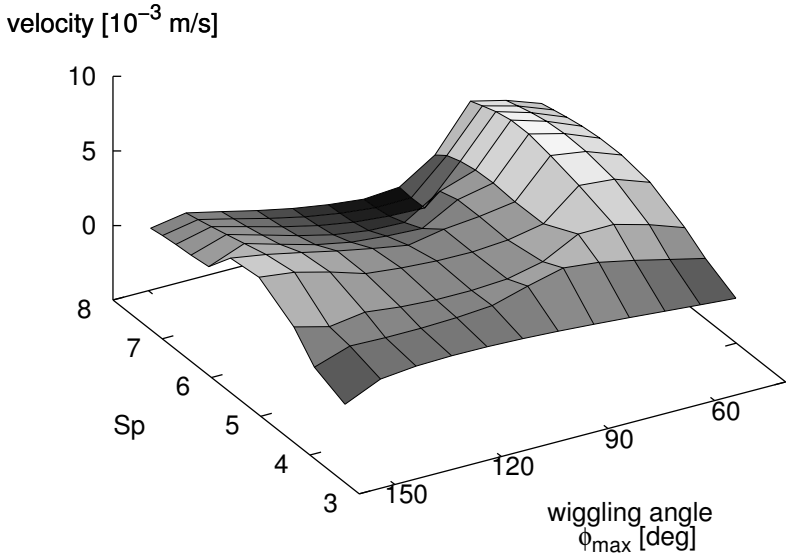

Fig. 5.12: The velocity of motion for large angular wiggling amplitudes. The plot is from the same data as in figure 5.10 but it shows the time-averaged absolute velocity. It is clearly visible that there is a significant drop in swimming velocity once the direction of net motion is no longer parallel to the z-axis.

oriented to $\mathbf{B}$, it effectively "feels" something like the time-averaged magnetic field

$$\overline{B}_i = \frac{1}{T} \int_{t=0}^{T} |B_i(t)| \mathrm{d}t \ . \tag{5.5}$$

According to equation (5.5) $\overline{\mathbf{B}}$ then is the effective field vector whose coordinates are given by the time-averaged coordinates of $\mathbf{B}$. Since the field turns "slowest" at the points of reversal (like a mathematical pendulum), $\mathbf{B}(t)$ "spends" most of the time at its maximal angular amplitude. Figure 5.11 shows the angle which the effective field $\overline{\mathbf{B}}$ defined by equation (5.5) encloses with the z-axis. Obviously, there is an interval of φ_{max} between 70° and 160° in which $\overline{\mathbf{B}}$ is more "parallel" to the y-axis than to the z-axis. Consequently, the filament turns around and prefers to be aligned with the y-axis. Nonetheless, some wiggling is still performed as a response to the time varying field. However, the wiggling is somewhat "out of sync" and has a very small amplitude. Therefore, the propulsive effect is not at all comparable to the situation where net displacement is parallel to the z-axis.

Figure 5.12 shows the absolute swimming velocity as a function of φ_{max} and Sp for the system of figure 5.10. Absolute values of the swimming velocity are used in figure 5.12 in order to better see the drop of the velocity when the wiggling angle is large and the motion is no longer in z-direction. For a constant $\varphi_{max} < 60°$, however, the behaviour is the same as in figure 5.3. Note that the velocity landscape in the region of $\varphi_{max} > 60°$ is by no means trivial. The origin of the complicated landscape can be understood when looking at the multifaceted

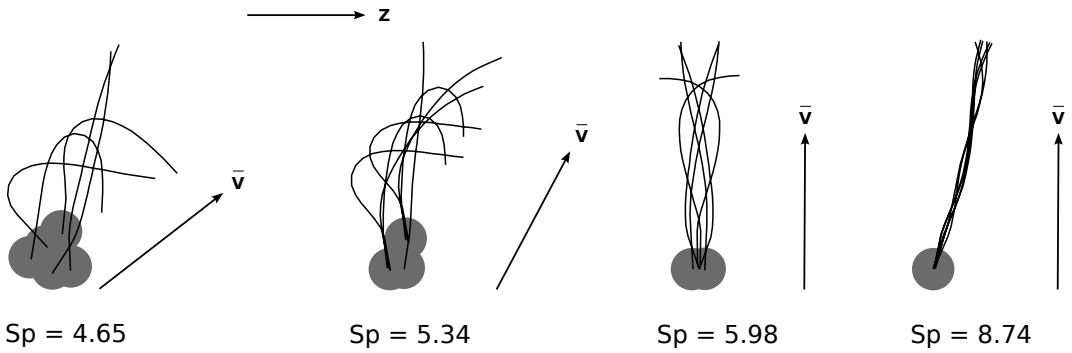

Fig. 5.13: Snapshots of wiggling modes in the transitional regime and on the plateau of figure 5.10. The wiggling angle φ_{max} of the actuating magnetic field is 100° for the two swimmers at skew swimming angles ψ on the left, $\varphi_{max} = 120°$ for the third swimmer from the left with symmetric wiggling about the y-axis and it is 150° for the swimmer on the right with $Sp = 8.74$. The approximate swimming angle ψ can be estimated by comparing the vectors $\overline{\mathbf{v}}$ to the horizontally drawn z-axis. As the third and fourth pictures from the left show, swimming in y-direction can be connected to symmetric wiggling about the y-axis but is not necessarily so.

wiggling modes assumed by the filament at different points (Sp, φ_{max}). Some snapshots of different wiggling modes in the transitional regime and on the plateau are shown in figure 5.13. One can imagine that it is difficult to find a representative and general description and we have chosen not to pursue this inefficient region any further.

5.4 Qualitative comparison to experimental data

As has already been mentioned several times throughout this text, a realization of the one-armed swimmer has been recently achieved by Dreyfus *et al.* [11]. They use a superposition of a static homogenous magnetic field in x-direction and a sinusoidal magnetic field in y-direction:

$$\mathbf{B}(t) = \begin{pmatrix} B_x \\ B_y \sin(2\pi f t) \\ 0 \end{pmatrix} . \tag{5.6}$$

Initially, the field is aligned in x-direction and the wiggling takes place in the xy-plane. In contrast to our system, the strength of the magnetic field is not constant at all times. Besides the Sperm number, Dreyfus *et al.* introduce two further dimensionless parameters to characterize their system: the ratio $b_0 = B_y/B_x$ and the "magnetoelastic number",

$$M_n = \frac{2\pi(aB_xL)^2}{3\mu_0 A}\left(\frac{\chi_\parallel - \chi_\perp + \chi_\parallel\chi_\perp/4}{(1-\chi_\parallel/6)(1+\chi_\perp/12)}\right) ,$$

where μ_0 is the magnetic permeability of vacuum and $\chi_\parallel$, $\chi_\perp$ give the magnetic susceptibilities parallel and orthogonal to the local direction of the filament. M_n is essentially our parameter H^{D0} up to a dimensionless pre-factor.

Experimental data for different values of b_0 and M_n are shown in figure 5.14. Also shown are corresponding curves from a numerical model by the same authors. The model relies on the slender-body approximation with anisotropic drag coefficients $\zeta_\parallel \neq \zeta_\perp$, hydrodynamic

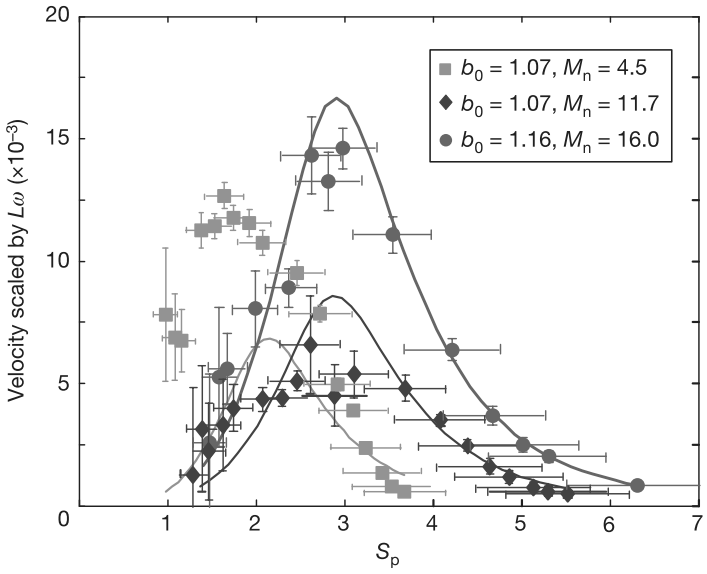

Fig. 5.14: The rescaled velocity as a function of the Sperm number for different values of the magnetic field. b_0 is the ratio of constant to time varying field $b_0 = B_y/B_x$ and M_n the "magnetoelastic number" (see text). The plot is taken from [11].

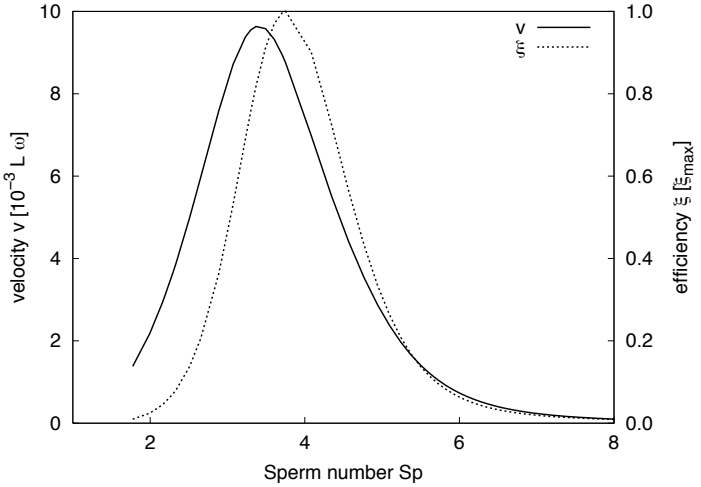

Fig. 5.15: The rescaled velocity and the efficiency as functions of the Sperm number for the magnetic actuation used by Dreyfus *et al.* We use the parameters $b_0 = 1.16$ and $M_n^* = 16.0$ corresponding to the data points drawn as circles in figure 5.14. However, the strength of the magnetic field was augmented to account for the larger distance between the dipoles (see text). The efficiency is given in units of $\xi_{max} = 02.32 \cdot 10^{-3}$ which is at $Sp = 3.75$. The velocity peak is at $Sp = 3.37$.

interactions are not included. Moreover, only next neighbour dipolar interactions are considered in the numerical model. The Sperm number Sp of the experimental data points has undergone a rescaling with a dimensionless parameter to account for the enhanced drag the swimmer experience close to a surface (see Supplementary methods of reference [11]). Although the agreement is fairly good for higher values of Sp, the data fail to satisfy on the left side of the peak.

Before one can compare the data shown in figure 5.14 to the simulation data from our model, one has to bear in mind that there are other fundamental differences besides the different time protocol of the actuating magnetic field. The artificial filaments of Dreyfus *et al.* consist of beads with a radius of $a \approx 0.5$ μm linked by several double-stranded DNAs with a length of 107 nm. The surface-to-surface distance of adjacent beads can thus be assumed to be smaller than 100 nm. These linkers will also have a non-trivial influence on the viscous resistance of the filament. (In the simulation model we use, the resistence of the linkers is neglected and the centre-to-centre distance of two adjacent beads is three particle radii so that the Rotne-Prager approximation can be used for hydrodynamic interactions.) Consequently, the viscous resistance of a filament of the same length is lower than in the experimental system. Due to the larger distance between the beads, dipolar interactions will also be weaker for the same strength of the external magnetic field.

Additionally, we believe that the bend stiffness in the experimental system must depend on the local curvature for the following reason: a high degree of local curvature will bring neighbouring beads into contact, if they are linked very close to one another. As we have no data of the real distance between adjacent beads, all we know is that it is at most 107 nm compared to spheres with a diameter of 1 μm. So, if we assume two adjacent beads to have a surface-to-surface distance of 100 nm, geometrical considerations show that the critical radius of curvature at which the beads touch is given by approximately 1150 nm (see reference [14]).[6] Further bending should then be only possible if the linkers on the far side (the side not in contact) are elongated. Therefore, a bend stiffness "constant" can only be assumed up to a critical degree of bending and the bend stiffness has to be assumed to be essentially non-linear for larger local curvatures.

Though a comparison of, e.g., figure 5.2 to the experimental data (or rather its numerical curves) in figure 5.14 shows a good qualitative agreement in spite of the differences outlined above, we have also implemented the actuation time protocol (5.6) employed by the experiment. Figure 5.15 shows the rescaled velocity as a function of Sp for the values of b_0 and M_n corresponding to the data shown as circles in figure 5.14. However, since in our simulation model the dipoles are farther apart from each other, the strength of the magnetic field has been fittingly augmented. We assume the distance between two dipoles in the experiment to be at most $d = 1.1$ μm compared to the bond length $l_0 = 1.5$ μm of our model. Since the dipolar interaction potential depends on the distance by $(1/r)^3$, the field strength needs to be stronger by a factor of 2.54 in order for two adjacent dipoles in our bead-spring model to have an interaction potential of the same strength.

If one looks at figure 5.15 one immediately notices that the maxima of velocity and efficiency have moved to smaller values of Sp when compared to figure 5.2. Thus, they are much closer to the experimental values. This must be a cause of the different actuation time pro-

[6] This corresponds to an angle of $\vartheta \approx 130°$ between two adjacent linkers in our bead-spring model, which is smaller than we observe in typical simulations. The snapshots in figure 5.13 come close with angles between 150° and 140°. However, if the surface-to-surface distance between adjacent beads in the experimental filament is a lot shorter than 100 nm, as we assume, this effect will become relevant at values of ϑ much closer to 180°.

tocols. The peak of the simulation only reaches two-thirds of the height of the experimental system. One the one hand, this might be due to the combined effects of different friction coefficients and a non-linear bend stiffness. On the other hand, the experimental beads are presumably much closer to each other. If, e.g., the beads were in contact, the magnetic field would have to be increased by a factor of 3.38 for a corresponding simulation run giving rise to a larger maximal velocity. However, this approach is somewhat questionable because one could also argue that the local field experienced by the finite size dipoles will become quite important and our assumption of point-like dipoles in a homogeneous external field of constant strength is no longer adequate for a description at such a short distance.

To conclude the comparison, we note that the simulation data is obtained without employing fit parameters or making any further assumptions. In contrast to the numerical model of [11], hydrodynamic and dipolar interactions between all beads of the filament are included.[7] As a further difference, the simulations work with a discretized filament very much like the experiment, whereas the numerical model relies on a continuous description of the filament. In this respect, we believe that our approach provides a valuable supplement to the experimental data as well as the numerical model.

[7] What could possibly be seen as a weak point of the simulations, however, is the assumption of point-like dipoles in a homogenous external field.

Chapter 6

Cilium attached to bounding wall

As a second simulation model, we study the motion of a filament that is attached to an infinitely extended bounding wall. This model is biologically inspired by the hair-like appendages called cilia on the surfaces of cells. Their motion is used for generating net thrust (also see section 2.2). Motile microorganisms, an example is the *paramecium* bacterium, swim with the help of cilia [29]. In contrast, other cells like those lining air passages, e.g., in the lung, use cilia to pump fluid.

6.1 Model of a cilium attached to a planar boundary

As for the one-armed swimmer, we use the discrete superparamagnetic filament as described in chapter 4. Instead of attaching it to a mobile head though, the filament is anchored in such a way that it protrudes orthogonal from an infinitely extended bounding wall in the xy-plane (see figure 6.1). In order to set the relaxed position along the z-axis, not only one but two points of attachment are needed since a single point acts like a free hinge. Consequently, the anchorage is achieved by having one point directly on the surface and another one "below" the bounding plane. These two points are kept at fixed positions and anchor the filament perpendicular to the xy-plane by linkers that participate in the bending and the stretching forces acting on the other spheres. However, they do not participate in hydrodynamic and dipolar interactions.

The filament is actuated by a time-varying external magnetic field, as before. However, we will see that it no longer suffices to employ a sinusoidally modulated field of constant magnitude. Instead, we use two different approaches that will be treated in sections 6.3 and 6.4, respectively. Nevertheless, the essential parameters of the system are still given by the Sperm number Sp (4.31) and the square root of H^{D0} (4.23), $B_s = \sqrt{H^{D0}}$. All data presented in this chapter has been obtained with parameter set II. However, we have also performed simulation runs with parameter set I to confirm the results and no qualitative or quantitative differences have occurred.

6.2 Efficiency for the performance of a cilium

Unlike the one-armed swimmer, a cilium as described above cannot acquire a time-averaged non-zero velocity because one of its ends is attached to the bounding wall. Nonetheless, if motion of the wall were possible, it typically would not be along the z-axis in the case of

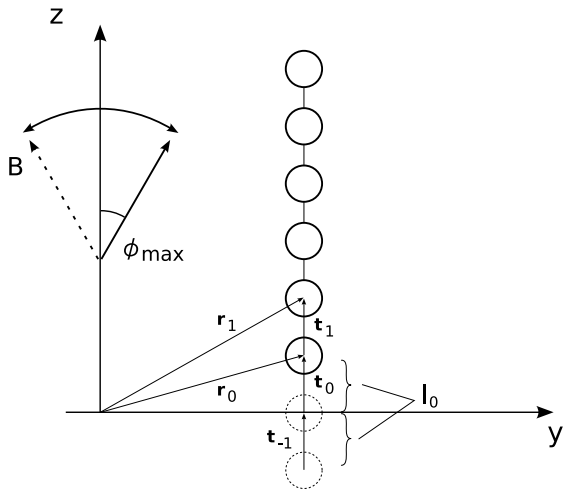

Fig. 6.1: Filament attached perpendicular to a bounding wall. The first three bonds $\mathbf{t}_{-1}$, $\mathbf{t}_0$ and $\mathbf{t}_1$ are shown. The filament really starts with the bead at $\mathbf{r}_0$, the virtual beads drawn as dotted lines are kept at fixed positions to anchor the filament perpendicular to the xy-plane. Furthermore, the virtual beads do not participate in hydrodynamic or dipolar interactions.

biological cilia. Even though developing thrust into the z-direction is possible by using the cilium as a flexible oar with a motion symmetric to the z-axis[1], this is not the task adopted by "real" cilia. In nature, cilia perform an asymmetric beating cycle consisting of a "power" and a "recovery" stroke as elaborated in section 2.2. In effect, each beating cycle then transports fluid along the plane which in the case of a mobile microorganism leads to propulsion in y rather than z-direction.

The goal of this section is to define a measure of efficiency for an asymmetric beating cycle of a cilium. Once this has been achieved, the question of how such an asymmetry can be implemented will be addressed in the following sections. The sloppy use of the term "asymmetry" can for now be seen as referring to the different filament shapes assumed by power and recovery stroke, respectively. Later, we will introduce a more well-defined asymmetry parameter.

As a tentative measure of efficiency, consider the difference between energy dissipated by motion parallel and anti-parallel to the plane (i.e. in positive versus negative y-direction) over the totally dissipated energy[2]

$$\xi = \frac{|\overline{W}_{\parallel}^{>} - \overline{W}_{\parallel}^{<}|}{\overline{\sum_i \mathbf{F}_i \cdot \mathbf{v}_i}} = \frac{\Delta \overline{W}_{\parallel}}{\overline{W}} \ , \tag{6.1}$$

[1]This can be observed in simulations by performing a symmetric wiggling and averaging over the stretching force on the anchoring point. Doing this shows that the averaged stretching force does not vanish indeed and the cilium thus "pulls" on the wall along the z-direction.

[2]Strictly speaking, $W(t)$ is the rate of dissipated energy at time t, so that $\overline{W} = \frac{1}{T}\int_0^T W(t)\mathrm{d}t$ is the time-averaged rate of dissipated energy. In equation (6.1), however, the normalising factor T^{-1} drops out. This is the reason why we sloppily just speak of the "dissipated energy".

where the respective energy contributions dissipated by motion in y-direction $W_{\parallel}^{\gtrless}$ are defined as

$$W_{\parallel}^{\gtrless} = \sum_i (\mathbf{F}_i \cdot \mathbf{e}_y)(\mathbf{v}_i \cdot \mathbf{e}_y) \qquad \forall\ (\mathbf{v}_i \cdot \mathbf{e}_y) \gtrless 0\ . \tag{6.2}$$

The line on top of the symbols in equation (6.1) denotes a time-averaged quantity over an actuation cycle. As before, $\mathbf{F}_i$ is the total force on bead i and $\mathbf{v}_i$ is its velocity. Note that for this measure there is no need to be able to distinguish directly between power and recovery stroke in equation (6.2). At each simulation step, all beads moving into positive y-direction contribute to $W_{\parallel}^{>}$, whereas all beads moving into negative y-direction contribute to $W_{\parallel}^{<}$.

Applying the efficiency of equation (6.1) to extremely simplified cases shows that (6.1) makes sense indeed. In order to obtain an upper bound of ξ, let all beads move along the positive y-axis, then $\xi = 1$. Of course, going into one direction only is not possible for a periodic motion since all beads somehow need to get back to their initial positions. Therefore, $\xi = 1$ cannot be practically achieved by a cyclic ciliary beating. On the other hand, consider wiggling the filament about the z-axis as is done for the one-armed swimmer. In this case the motion is symmetric to the z-axis. It is clear that $W_{\parallel}^{>} = W_{\parallel}^{<}$ and hence $\xi = 0$ as must be, because there cannot be any net fluid transport parallel to the bounding wall.

From these considerations we expect ξ as defined in equation (6.1) to assume values in the range $[0, 1)$ depending on the "degree of asymmetry" within one beating cycle. As we have done before, we now explicitly partition the beating cycle of a cilium into two different processes of (i) an effective power stroke at high energy cost and (ii) a recovery stroke at the minimal energetic cost possible where the cilium is positioned for the next power stroke.

As has been mentioned in section 2.2, a power stroke can be realized by pivoting a straight cilium at maximal viscous resistance while in the corresponding recovery stroke a bent configuration is assumed that reduces the viscous resistance on the way back.

The state of bending that our model filament assumes as response to an external driving force is determined by the Sperm number. Therefore, having a more rigid filament for the power and a more "sloppy" filament for the recovery stroke is tantamount to switching the Sperm number Sp between two different values during the actuation cycle. While this picture of a variable Sp is illustrative, we will introduce an average Sperm number and express the asymmetry with the help of an additional asymmetry parameter. How this can be achieved is investigated in the following.

6.3 Model I: unequal velocities of beating

Besides material parameters and the length L, which we consider to be unmodifiable for a given filament, Sp depends on the frequency of actuation. By using unequal velocities of beating for power and recovery stroke, it should be possible to realise an asymmetric cycle. In contrast to the sinusoidal time dependence of φ in section 4.7.3 and chapter 5, φ is linear in time with two distinct velocities. The wiggling angle φ_{max} is kept constant at 80° for this model. The Sperm number is now defined with the frequency ω of the complete beating cycle. Then we take the period $T = 2\pi/\omega$ and partition it into intervals a and b for recovery and power stroke so that $T = a + b$. The asymmetry parameter ε describes the ratio of times taken by the magnetic field $\mathbf{B}(t)$ to turn from $-\varphi_{max}$ to φ_{max} and vice versa as illustrated in figure 6.2. Hence, we define ε as

$$\varepsilon = \frac{b - a}{a + b}\ . \tag{6.3}$$

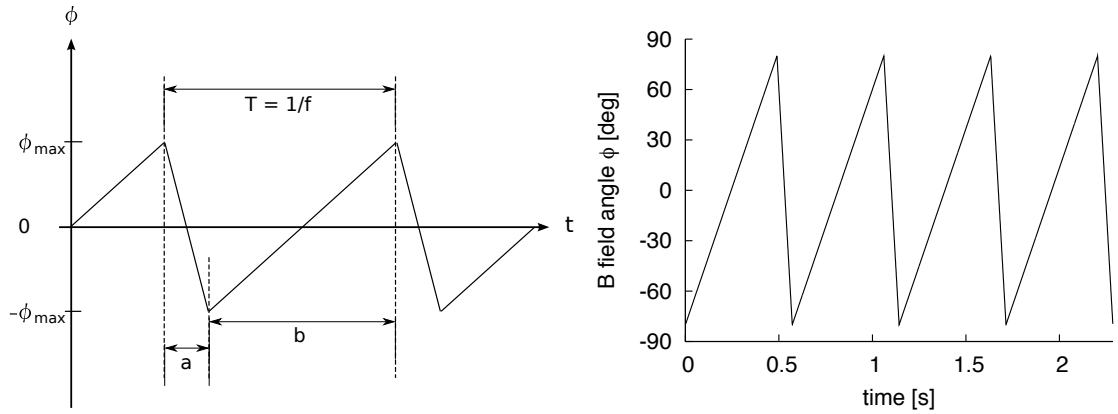

Fig. 6.2: **Left**: the angle φ enclosed by $\mathbf{B}(t)$ and the z-axis as a function of time. φ has different velocities when decreasing and increasing, respectively. The duration of a cycle is given by $T = 2\pi/\omega = a + b$, where a and b are the respective durations of recovery and power stroke. We define an asymmetry parameter $\varepsilon = \frac{b-a}{a+b}$. **Right**: $\varphi(t)$ with $\varphi_{max} = 80^\circ$ for a typical value of $\varepsilon \approx 0.7$.

Then, ε evaluates to $\varepsilon = 0$ for $a = b$, whereas $\varepsilon = 1$ denotes the extreme case where the power stroke takes the entire time of the period T and the recovery stroke is performed instantaneously. Note that the term "asymmetry" previously referred to asymmetric motion of the filament while it is now much better defined by characterizing the degree of asymmetry of the actuation.

Figure 6.3 shows the efficiency ξ as a function of Sp and ε. The exact shape of the curves for constant Sp can better be seen in figure 6.4. The snapshots in figure 6.5 belong to the curve with $Sp = 3.34$. The effect of ε on both shape and maximal amplitude of the beating filament is clearly visible. As must be the case, ξ vanishes for all Sperm numbers when $\varepsilon = 0$. It is clearly visible that decreasing ω, which corresponds to smaller Sperm numbers, has the potential for better efficiency values if ε is increased at the same time. This is not at all surprising when one remembers that the power stroke is meant to be performed in rigid rod-like fashion which requires values of $Sp \lesssim 3$ (see section 2.3). In turn, the velocity of the recovery stroke is adjusted through the asymmetry parameter ε. Hence, one observes that there is an optimal ε that is small for large values of Sp and that increases when Sp is decreased. This means that there is a point at which it does not make sense to drive the recovery stroke faster. Obviously, the filament cannot perform the recovery stroke at an arbitrary velocity. If the field changes its direction too fast, recovery does not happen exclusively in the recovery time slot but also in the time alloted to the power stroke. This reduces the amplitude of beating as illustrated in figure 6.5 for increasing ε. At the same time, however, the visible asymmetry of the shape of the cilium further increases. Yet, it is a tempting delusion to assume the asymmetry of the shape is necessarily connected to a larger efficiency value. After all, not momentous snapshots but equation (6.1) determine the efficiency by considering the motion averaged over a beating cycle. In this respect, there is an optimal ε for any constant value of Sp, albeit the drop of ξ with increasing ε is fairly moderate.

Although a global peak of efficiency is not shown in figure 6.3, it is clear from the reasoning above that the efficiency ξ tends to ever larger values for $Sp \to 0$ and $\varepsilon \to 1$. This does not, however, mean that there is no upper bound on ε. On the contrary, ξ, as defined in equation

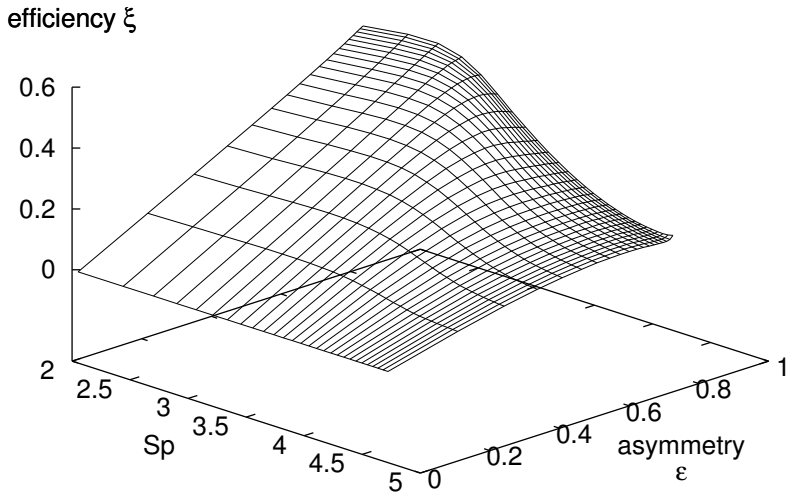

Fig. 6.3: Efficiency ξ as defined in equation (6.1) as a function of Sp and the asymmetry parameter ε. The cilium performs power and recovery strokes at different velocities, the ratio of which is characterized by ε. The magnetic field is kept constant at $B_s = 3.29$.

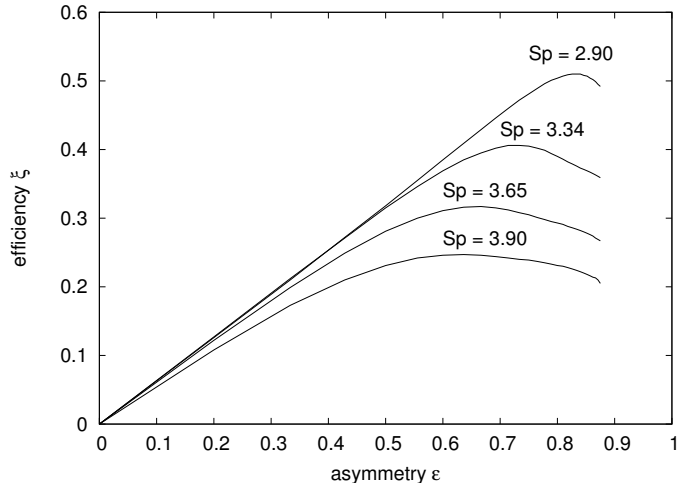

Fig. 6.4: Efficiency ξ versus asymmetry parameter ε. This plot shows four curves at different values of Sp while the field is $B_s = 3.29$ as in figure 6.3. It is clearly visible that the peak of the efficiency moves to larger values of ε for lower values of Sp. To the right of the maxima the efficiency declines visibly.

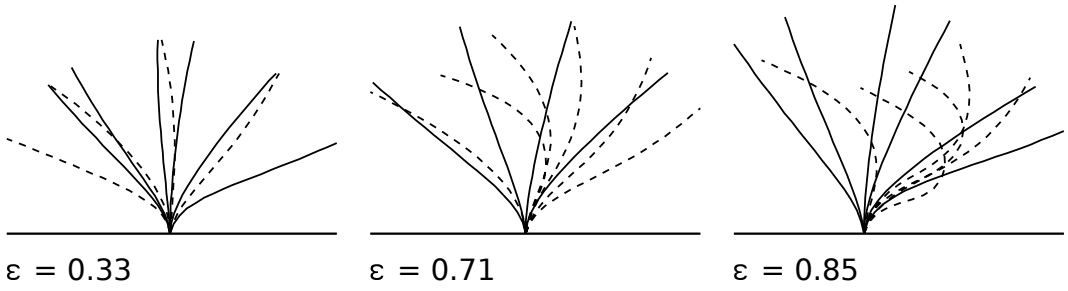

Fig. 6.5: Snapshots of the filament shape during one cycle for different ε. The snapshots are taken in a way that equally represents power and recovery stroke rather than at equidistant points of time. The parameters used are $Sp = 3.34$ and $B_s = 3.29$. In the slower power stroke (drawn as solid line) the filament tilts from left to right and for the faster recovery stroke (dotted line) from right to left. By this beating, fluid is transported from the left to the right.

(6.1) is smaller than one by definition. In practice, the value of one cannot be reached, since there always is a finite contribution of energy dissipated by motion in z-direction on top of the energy dissipated during the recovery stroke.

In figure 6.6 the time-averaged rate of dissipated energy $\overline{W}$ as a function of Sp and ε is shown. The lowest value is in the foremost left corner, i.e. at the lowest driving frequency and at $\varepsilon = 0$. The line at $\varepsilon = 0$ gives the power required for operating a symmetric beating of the cilium as a function of the Sperm number.[3]

The region covered by the ridge from the front right to the back left roughly corresponds to the region in figure 6.3 where ξ assumes its maximal values as a function of ε with constant Sp. While a fairly high rate of dissipated energy is to be expected at the maximal efficiency, it is remarkable that there is a steep decline to the left of the ridge in figure 6.6 whereas the efficiency in figure 6.3 remains at a rather high value. This can only mean that lower values of Sp at constant ε are not as advantageous as it might have seemed by only looking at figure 6.3. As 6.6 shows, the cilium operates at very low "power" even if the efficiency ξ is good. After all, however, one needs "power" to transport fluid. The argument above does not only apply when comparing motion at different values of Sp for a constant ε. We have stated that a global efficiency maximum exists in the limit $Sp \to 0$ and $\varepsilon \to 1$. On the other hand, by looking at figure 6.6 one notes that the rate of dissipated energy is maximal for $\varepsilon = 0$. Therefore, the global maxima of efficiency and "power" of the cilium do not appear at the same values of Sp and ε.

Similarly, a cilium operating at larger values of ε compared to its optimum value may only experience a moderate drop in ξ whereas the rate of dissipated energy is more significantly reduced, as can be seen well in figure 6.7. In this plot, both the rate of energy dissipated by motion in y-direction $\overline{W}_{\parallel} = \overline{W}_{\parallel}^{<} + \overline{W}_{\parallel}^{<}$ and the rate of the totally dissipated energy $\overline{W}$ are plotted. The nearly constant offset in the y-direction of the plot between these curves is typical and shows that the rate of energy dissipated by motion in z-direction is nearly constant.[4]

[3] The time-averaged rate of dissipated energy has the unit J/s which corresponds to a power. Since the energy consumed by the motion of the filament is supplied by forces through the external field, the rate of dissipated energy is connected to the work done by the magnetic field.

[4] Although the calculations are three-dimensional, there is no motion and hence no energy dissipated by motion in x-direction due to the symmetry of the actuation.

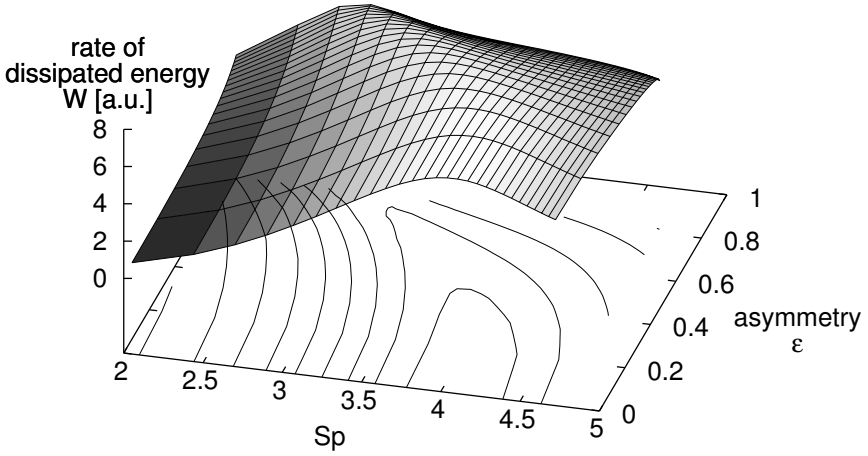

Fig. 6.6: The time-averaged rate of dissipated energy $\overline{W}$ as a function of Sp and ε in arbitrary units (absolute values are on the order of 10^{-9} J/s). The ridge starting in the front right of the middle covers the region of maximal efficiency in figure 6.3. Notably in contrast to the efficiency landscape is the fact that the steeper decline is to the left of the ridge, i.e., at lower values of Sp. Black shading corresponds to the lowest and the white colour to the highest value of $\overline{W}$ and the lines on the base denote equidistant levels of altitude.

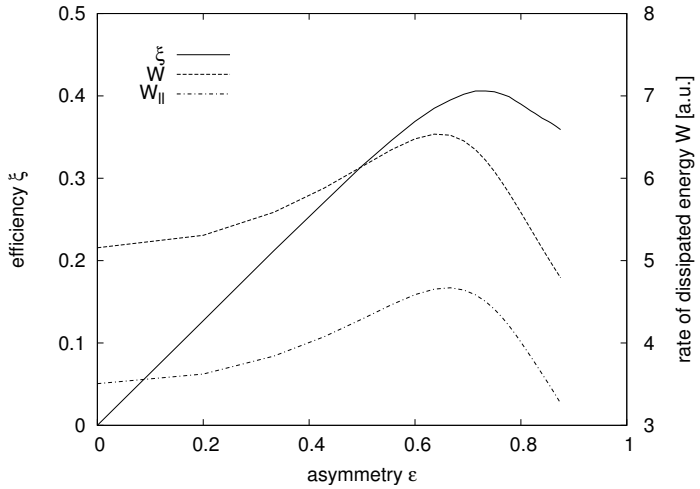

Fig. 6.7: Efficiency ξ versus ε at $Sp = 3.34$. Also shown are the time-averaged rate of dissipated energy $\overline{W}$ and the time-averaged rate of energy dissipated by motion in y-direction $\overline{W}_{\parallel}$.

To conclude the study of a cilium with different beating velocities during power and recovery stroke, it can be said that we have found a mode of operation for an asymmetric beating cycle that is definitely functional and delivers excellent performance on our efficiency scale (6.1). We have obtained a thorough understanding of the system and have shown that very high values of ξ can be reached at low Sperm numbers and large ε while the demand for more "power" in the beating of the cilium requires larger values of Sp and smaller values of ε. A trade-off between these two aspects gives the parameters at which our model cilium is best employed.

6.4 Model II: varying field strength

As we have noted in section 5.2, increasing the external field has an effect similar to an increase of the bend stiffness insofar as the filament prefers a straight configuration corresponding to the minimum of the dipolar interaction potential H^D. This motivates to realise power and recovery stroke by applying a field with alternating strength.

The angle φ between field and z-axis is again given by a sinusoidal time dependence $\varphi(t) = \varphi_{max}\sin(\omega t)$. The magnitude of the field, on the other hand, varies during one beating cycle, so that the time dependence of the field is given by

$$\mathbf{B}(t) = B(t)\begin{pmatrix} 0 \\ \sin(\varphi(t)) \\ \cos(\varphi(t)) \end{pmatrix} , \tag{6.4}$$

where

$$B(t) = B_0 + \frac{\varepsilon B_0}{2}\left(1 - \frac{4}{\pi}\left\{\sin(\omega[t+\pi/2]) + \frac{\sin(3\omega[t+\pi/2])}{3} + \frac{\sin(5\omega[t+\pi/2])}{5} + \frac{\sin(7\omega[t+\pi/2])}{7}\right\}\right) . \tag{6.5}$$

Equation (6.5) describes a magnetic field of magnitude B_0 during the recovery stroke that is periodically augmented by $\Delta B = \varepsilon B_0$ during the power stroke as illustrated in figure 6.8. ε denotes the asymmetry parameter. At $t = 0$ both cilium and field are aligned along the z-axis, i.e. in the middle of a stroke. $B(t = 0)$ starts at the augmented value $B_0 + \Delta B$ suited for the second half of the power stroke. When φ_{max} is reached, it drops to B_0 for the recovery stroke and then goes up again in anticipation of the following power stroke.

The terms enclosed in curly brackets in equation (6.5) are the leading terms of a Fourier series of a step function with step height $\pi/4$. We use the Fourier series rather than the step function itself in order to have a smooth transition from lower to augmented field values B and vice versa. Otherwise, the filament performs a visible jerk to adapt to the suddenly switched value of the magnetic field. Since this is of no perceivable advantage and in addition obscures the visible distinction of power and recovery stroke in snapshots and movies of the system, we subdue the effect by a continuous change of B.

Figure 6.9 shows the efficiency as a function of B_s and the asymmetry parameter ε. The rescaled field strength B_s is evaluated for B_0 and the additional field ΔB during the power stroke is solely expressed by the parameter $\varepsilon = \Delta B/B_0$. One immediately notices that the plot is incomplete and there is no data shown in the region of the upper right corner. In this region, our model filament encounters numerical instabilities of the nature described

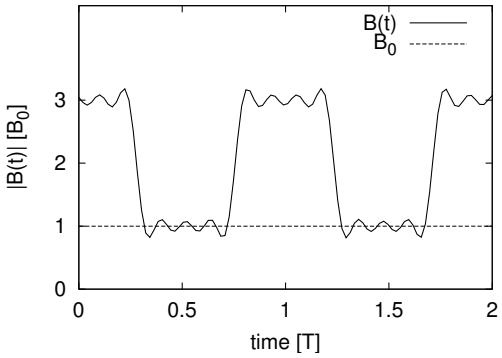

Fig. 6.8: The magnitude of the magnetic field **B** is shown in units of B_0 as a function of time. The illustrative value of $\varepsilon = 2$ is used. The x-axis is given in units of T which is the time required for one cycle by the relation $T = 2\pi/\omega$. As only the first four terms of the Fourier series for a step function are included, bumps on the horizontal parts are clearly visible.

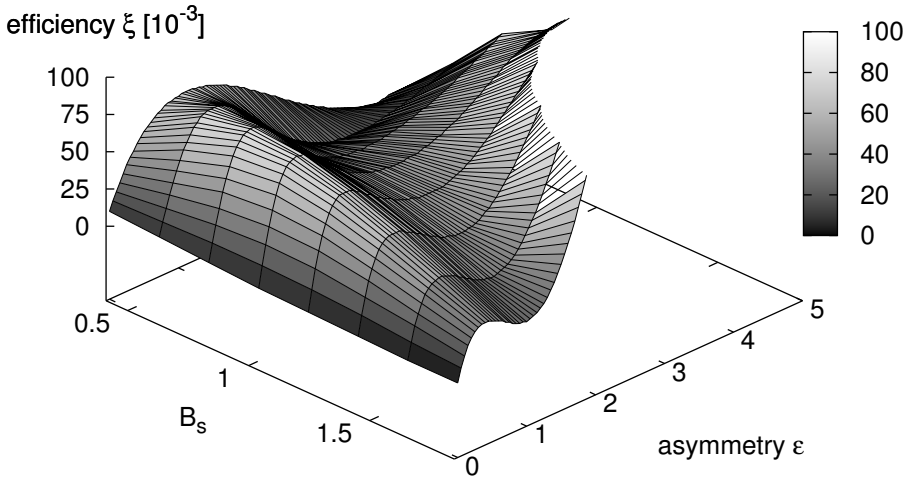

Fig. 6.9: The efficiency ξ of equation (6.1) as a function of B_s and the asymmetry parameter ε. No data exists for the upper right corner due to numerical instabilities. This plot has been obtained at $Sp = 4.34$, but the qualitative features are not very sensitive to minor changes of Sp.

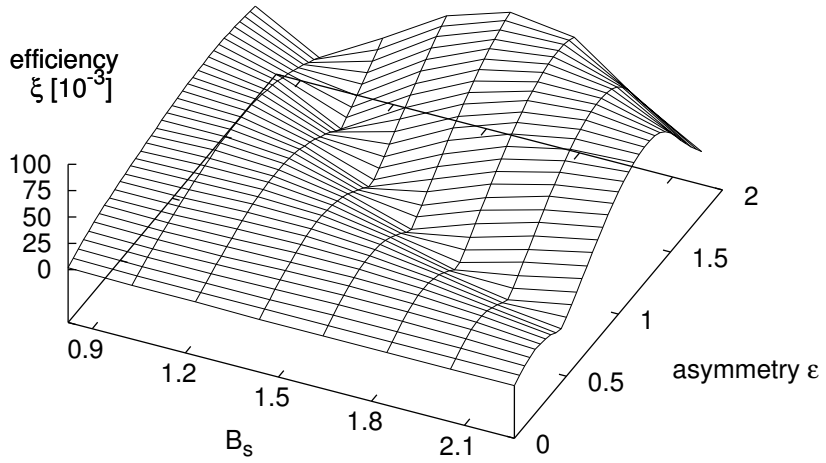

Fig. 6.10: Again, the efficiency ξ as a function of B_s and ε but at a larger Sperm number $Sp = 6.5$ and for a smaller parameter range than in figure 6.9. For $\varepsilon \to 0$, however, the data is not reliable as the limit cycle of the beating has not been reached. This explains the non-zero $\xi(\varepsilon = 0)$.

in section 4.6.2. These cannot be avoided by smaller integration steps. They seem to be connected to the fast change of the magnitude of the field in combination with large driving angles φ_{max}. There is, however, no point in driving the filament at small angles because the desired asymmetry between power and recovery stroke also decreases. For this reason, $\varphi_{max} = 60°$ is used throughout this section.

The features shown in figure 6.9 are not very sensitive to small variations of Sp in the optimal Sp range of 4 to 7. Hence Sp is not an important parameter in this system, other than that it needs to be at a value that readily allows bending of the cilium during the recovery stroke. However, at larger values of Sp the system tends to be somewhat more stable at larger values of ε while, on the other hand, it takes longer to reach the limit cycle. Using a larger Sp we have obtained the data shown in figure 6.10 at considerable computational cost. Note that B_s and ε cover a smaller range compared to figure 6.9. For symmetric beating, i.e., for $\varepsilon = 0$, ξ must be zero, which it is neither exactly in figure 6.9 nor in 6.10 (even if the perspective makes it hard to tell the values precisely). This is simply due to the fact that ξ is evaluated after a simulation time in which the limit cycle of the cilium has not been reached and effects from the initial configuration persist. This preferably happens for small values of ε and when in addition B_0 is very small and Sp large. We have performed simulation runs of much longer duration and there is no doubt that $\xi(\varepsilon = 0) \to 0$ asymptotically. At the same time, results become more accurate with increasing ε beyond 0.1, so that the qualitative features of figures 6.9 and 6.10 can be confirmed with confidence.

Figure 6.10 suggests that the steep ascent of ξ towards bigger ε in figure 6.9 soon drops again. In figure 6.10 the drop is visible for the parameter combination $\varepsilon > 1.75$ and $B_s > 1.8$. In figure 6.11 the same situation is shown in a two-dimensional plot for lower values of B_s

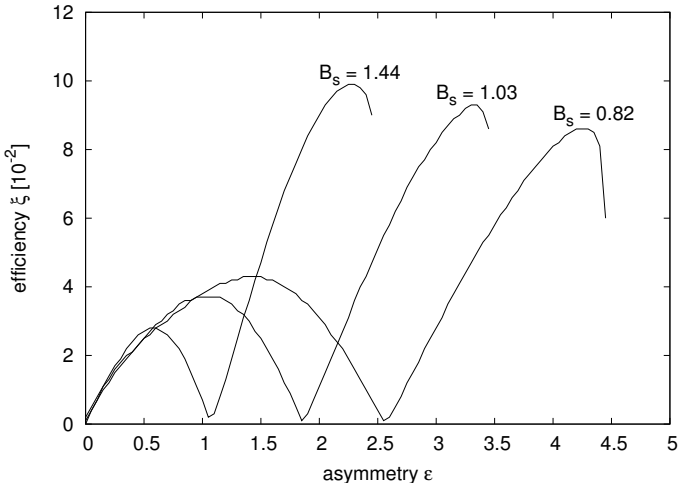

Fig. 6.11: ξ as a function of ε for several values of B_s at $Sp = 6.5$. All curves share the same characteristics of two maxima with a sudden drop right after the second and larger peak, albeit at different values of ε. For smaller values of B_s the first peak gains in magnitude compared to the second one.

(again, the curves do not start exactly at zero for $\varepsilon = 0$ due to evaluation of ξ before the limit cycle has been reached). For these curves, the drop looks even more sudden and drastic.

Surprisingly, for a fixed value of B_s there seems to be not only one maximum but there are two peaks at different values of ε with a significant drop into a valley close to zero in between. This is hard to understand and seems to be connected to different modes of motion belonging to different intervals of ε. Unfortunately, these modes are not immediately apparent to the eye when snapshots or movies of the beating cilium are studied.

Nonetheless, figure 6.12 shows some typical snapshots of a cilium operating at the small maximum on the left, in the valley and on the large maximum to the right. (The snapshots correspond to figure 6.9 even though the large maximum is not resolved in this figure). At the small maximum, there is some asymmetry in the motion but the amplitude of beating is small. So, this is the cause for the low value ξ. In the valley, the asymmetry looks more pronounced. However, this is not all that counts because it is also important just how the relaxation from a more bent to the more straight configuration happens. Apparently, in the valley a motion is assumed that is asymmetric but does not achieve a notable efficiency according to equation (6.1). It is visible that the beating cycle for cilium operating at the higher maximum is similar to the motion we have found in the previous section. During the recovery stroke, the filament is partially folded. Just before the power stroke, it straightens by moving the loose end along the tangent of the filament thus with a minimum of friction.

The drop of ξ at even larger values of ε is easier to understand because the motion of the filament suddenly looks completely different as shown in figure 6.13. Apparently, the free end of the filament is folded to a hairpin. This is somewhat reminiscent of the swimming modes of the one-armed swimmer at large angles φ_{max} (see section 5). After several beating cycles, a configuration is established for which the free end of the cilium bends by nearly 180°. However, this final configuration is not a consequence of following the field which only has a wiggling amplitude φ_{max} of 60°, meaning field and filament cannot be parallel for the hairpin configuration. On the contrary, in figure 6.13 the free end of the cilium folds to the left when

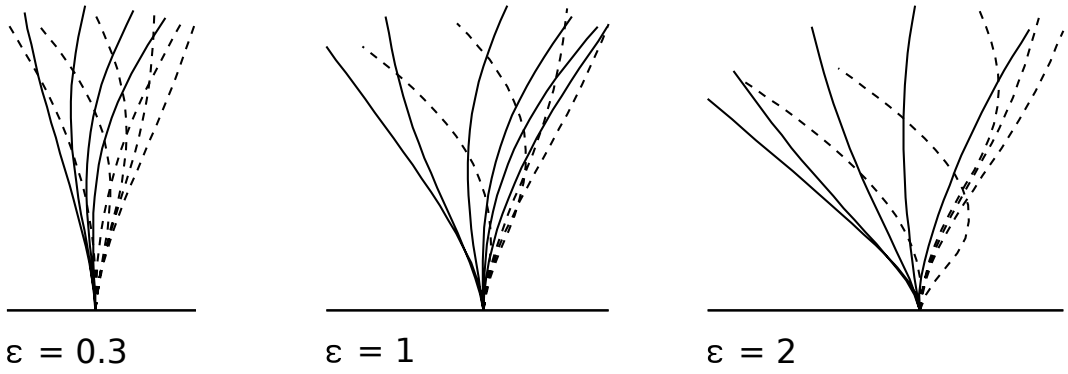

Fig. 6.12: Snapshots of the filament shape during one cycle for different ε with the parameters $B_s = 1.64$ and $Sp = 4.34$. For this B_s the cilium operates at the lower peak for $\varepsilon = 0.3$, down in the valley for $\varepsilon = 1$ and at the ascent to the higher peak for $\varepsilon = 2$ (see figure 6.9). The power stroke is drawn as solid line and the recovery stroke as dotted line.

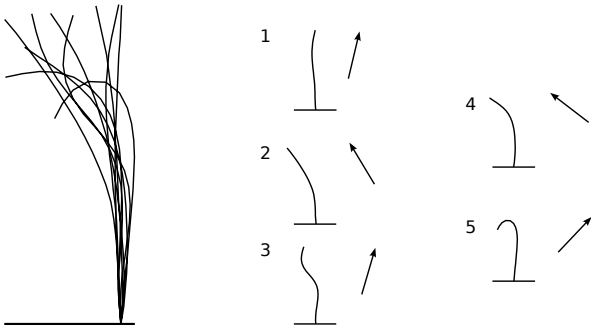

Fig. 6.13: **Left:** snapshots of the shape of the cilium taken for parameters $B_s = 0.82$, $Sp = 6.5$ and $\varepsilon = 4.6$, corresponding to the drop of the efficiency in one of the curves of figure 6.11. **Right:** schematic depiction of how the filament folds to a hairpin. The arrows denote the direction of the magnetic field.

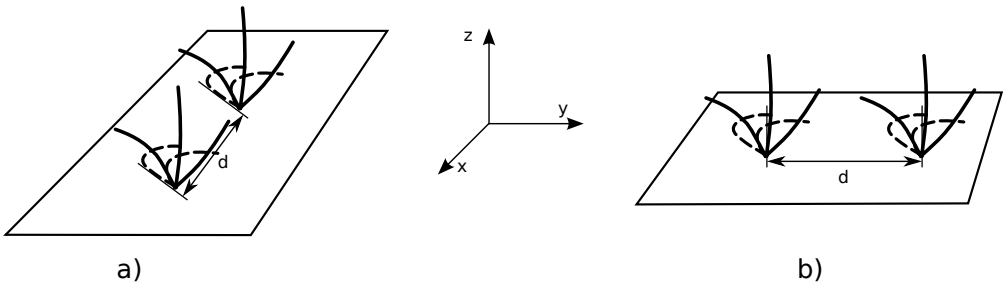

Fig. 6.14: Geometry of two cilia with distance d between them attached to a bounding plane. **a)** "Parallel" beating of two cilia that are both located along the x-axis. The motion of the cilia takes place in two planes parallel to the yz-plane. **b)** "In-line" beating of two cilia that are both located along the y-axis. The motion of both cilia takes place in the yz-plane.

the field tilts to the right. This mode of motion sets in quite suddenly above a critical value of ε for a given field strength B_s. It marks the transition to a region of $\xi(B_s, \varepsilon)$ which is no longer efficient according to (6.1) and which is also prone to numerical instabilities. In addition, it can be found by investigating the trajectories of single beads or watching a movie of the motion of such a filament that the beating seems to be chaotic and often no limit cycle is reached before a numerical instability finally occurs. However, the common feature in this regime is the hairpin as illustrated in figure 6.13.

Even though we have not studied all aspects of the system as thoroughly as in the previous section, we have shown that performing power and recovery stroke in model II is feasible, albeit at much lower efficiency and with more complicated dynamics as in model I. This system only achieves efficiency values $\xi < 0.1$ that are small compared to the values of $\xi \approx 0.6$ of model I. Furthermore, our work has been hindered by numerical problems to which a solution may yet be found. For the time being, though, the approach of using different beating velocities for power and recovery stroke as described in the previous section seems far more promising.

6.5 Collective beating of two cilia in proximity

It has long been believed that hydrodynamic interactions play an important role in the synchronisation of ciliary beating necessary for *metachronal waves*. The first attempt of describing the effect of hydrodynamic interactions of beating flagella has been made by Taylor [36]. While the present work does not address this intricate problem of ciliary synchronisation, the effect of hydrodynamic interactions is present and visible for two cilia beating synchronously in close proximity. However, the work on this has only just begun and the results presented in the following have a preliminary character.

We study the efficiency ξ for the collective beating of two cilia that are situated as illustrated in figure 6.14. The cilia are actuated as in model I (section 6.3) and the optimal asymmetry parameter $\varepsilon \approx 0.71$ for the cilium with $Sp = 3.34$ from figure 6.4 is used. Note that we use cilia with $N = 20$ beads, which gives a length of the cilium from wall to the last bead of the loose end of $L = 20l_0$. The efficiency ξ is evaluated as defined in equation (6.1) for all beads of both cilia.

Table 6.1 shows the efficiency values for both two-cilium configurations at different distances between the cilia. The efficiency values are given in units of ξ^0 which is the efficiency

	$B_s = 2.47$		$B_s = 3.29$	
$d\,[L]$	$\xi_{parallel}\ [\xi_1^0]$	$\xi_{in-line}\ [\xi_1^0]$	$\xi_{parallel}\ [\xi_2^0]$	$\xi_{in-line}\ [\xi_2^0]$
0.2	1.13	-	1.05	-
0.3	1.09	1.17	1.04	-
0.5	1.04	1.11	1.01	1.04
1.0	1.01	1.05	1.00	1.02

Tab. 6.1: Efficiency values ξ of a two-cilia configuration for two different values of B_s. The leftmost column gives the distance between the cilia in units of the cilium length $L = 20l_0$. The geometrical arrangement is expressed through $\xi_{parallel}$ for "parallel" beating and $\xi_{in-line}$ for "in-line" beating (see figure 6.14). The efficiencies $\xi_{parallel}$ and $\xi_{in-line}$ are given in units of the respective efficiency for a single cilium $\xi_{1,2}^0$. For the lower value of the magnetic field $B_s = 2.47$ the efficiency of a single cilium is $\xi_1^0 = 0.31$. At field strength $B_s = 3.29$ a single cilium operates with an efficiency of $\xi_2^0 = 0.406$.

of an isolated cilium operating at the same parameters. Some data for "in-line" beating is missing because the cilia come too close to each other during the beating cycle. It can be clearly seen that the increase of efficiency for a two-cilia system is larger at the lower value of the field B_s. Furthermore, the data suggests that the hydrodynamic coupling for "in-line" beating is more pronounced than for the "parallel" configuration. In this respect, there seems to be an equivalence for "parallel" beating at a distance of around $d = 0.3L$ and "in-line" beating at around $d = 0.5l_0$.

While the data in table 6.1 is not representative of all possible geometrical configurations for two or several cilia, it has become clear that two synchronously beating cilia at a distance d on the linear dimension of the length of the cilia L interact with each other through hydrodynamic interactions. This increases the efficiency of both cilia. The increase depends on the geometry of the configuration and subsides with increasing distance d. If one bears in mind that many cell surfaces are covered with dense arrays of cilia, one can easily imagine, that these effects become much more relevant than they are for two cilia in an otherwise quiescent fluid. As an outlook, this motivates the study of systems consisting of more than two cilia. The detailed knowledge of the role of hydrodynamic interactions in such multicilia systems could be an important step towards a better understanding of the complex collective beating patterns observed in nature.

Chapter 7

Conclusion

The major objective of this work has been to gain an understanding of the dynamics of biomimetic filaments in a highly viscous environment. The filaments are used in the context of biologically inspired machines for locomotion and fluid transport. We have developed the bead-spring model of a magnetic, discrete filament which is both computationally efficient and also has an experimental representation with the artificial filaments fabricated in the group of J. Bibette [14].

Throughout the present work, a special focus has been set on the role of hydrodynamic interactions. In our model, hydrodynamic interactions have been shown to be crucial for generating net motion in the case of the one-armed swimmer. They also play an important role for the efficiency of a cilium attached to a wall. This becomes apparent, for instance, by the considerable increase of efficiency of fluid transport when two cilia in very close proximity perform a synchronous beating compared to the beating of an isolated cilium. Moreover, the synchronisation of ciliary beating that leads to the phenomenon of so-called metachronal waves, has long been believed to be caused by hydrodynamic interactions, starting with the work of Sir Taylor [36]. For these reasons, a solid framework for the inclusion of hydrodynamic interactions both in an unbounded fluid and in the vicinity of an infinitely extended bounding wall has been given in chapter 3.

In chapter 4, a set of robust scaling laws has been derived that allow a general treatment of the dynamics of a magnetically actuated discrete filament. These scaling laws have been shown to be analytically exact in absence of hydrodynamic interactions and for a filament of infinite length. However, even when hydrodynamic interactions are considered and for filaments with a small number of only 20 beads, the results are convincing to the degree of justifying the characterization of the filament by the dimensionless Sperm number Sp and the rescaled magnetic field B_s in combination with the geometry of actuation.

With the one-armed swimmer, a simple realisation of a micro-swimmer has been thoroughly investigated in chapter 5. We have obtained a detailed understanding of the swimming velocity and the efficiency as functions of the system and actuation parameters which are subsumed in the Sperm number and the rescaled magnetic field. Furthermore, we have shown that both the swimming velocity and the efficiency of the one-armed swimmer become larger with an increasing wiggling angle up to the point at which swimming no longer occurs along the main axis about which the wiggling takes place. For larger wiggling angles, the swimmer turns around and performs an inefficient wiggling that in general is asymmetric. This leads to swimming at a skew angle or orthogonal to the main axis. Therefore, steering

of the one-armed swimmer should not be achieved by swimming at a skew angle to the main axis of actuation. The swimmer can be turned around more efficiently by allowing time for a complete reorientation to the new swimming direction indicated by a static magnetic field. Last but not least, we have compared our simulation results to the experimental velocity data available from the swimmer of Dreyfus *et al.* [11] to find a full qualitative agreement for the velocity curves. Even quantitatively, the results match well with a mere factor of 1.5 by which the peak values of the simulated velocity and the experimental velocity differ. If one considers the differences that do exist between experiment and simulation, and also the fact that the hydrodynamic properties of the experimental filament are not very well known, this is an impressive result. The experimental and the simulated swimmer undoubtedly share the same physical characteristics. Consequently, this work supplements the experimental data and it allows an easy and detailed study of the operational mode of the one-armed swimmer.

Chapter 6 shows that fluid transport and mixing at low Reynolds number is possible with the help of the superparamagnetic, elastic filament which serves as an artificial cilium. Moreover, such a machine need not have a complex design but can be easily powered by an external time-varying magnetic field. While we have shown that different beating velocities during one cycle and a periodic augmentation of the magnetic field have the desired effect of producing an asymmetric beating cycle, the latter system has turned out not to be as promising as the first one. We have shown that operating the first model (with different beating velocities during one cycle) at both maximal efficiency and "power" is not possible because the respective maxima do not appear at the same parameter values. Nevertheless, a compromise can be found, so that the operation of the cilium at good values of efficiency and at high "power" can be attained. We believe that this system qualifies as a suitable candidate for experimental realisation.

Although the study of collective beating of cilia has only just begun, we have shown that the beating of two cilia in close proximity increases the efficiency of each cilium by up to 20% through hydrodynamic interactions. The data obtained suggest that this effect is significantly more pronounced for the configuration in which the cilia are situated behind each other compared to a sideways configuration relative to the plane of motion. The coupling is not only present for cilia very close to each other but also plays an important role on distances comparable to the linear dimension of the length of the cilia.

In the future it would be interesting to further pursue this co-operative aspect of ciliary beating. The still not completely solved question of a possible synchronisation of two originally asynchronously beating cilia mediated by hydrodynamic interactions could also be addressed with our simulation model. Moreover, one can easily imagine that much more pronounced hydrodynamic coupling occurs on a surface that is covered by a closely packed array of cilia, as is indeed the case for many cells. There will no longer be a quiescent fluid background and the advent of self-organised complex collective beating patterns like that of metachronal waves seems very plausible.

Chapter 8

Acknowledgements

First and foremost, I am deeply indebted to my supervisor Dr. Holger Stark, who was always willing to donate as much time as necessary for delving into interesting and elucidating discussions about any questions and problems I encountered. At the same time, the supervision was performed in a way that put an emphasis on his being available whenever I needed support but also giving me the time and freedom for trying to find my own way first. This has been an experience I have very much enjoyed!

Professor Peter Nielaba has kindly offered to assess this work as a second corrector. He has also encouraged me by showing enthusiasm for and interest in this project. For this I would like to express my gratitude.

I am also especially grateful to Michael Reichert, who was ready to go to any length to share his impressive expertise on the particular subject of simulations in Stokes flow and also to lots of other questions related to physics in general. Many difficulties I encountered could be solved with his help and the present work owes quite a few ideas and approaches of physical or technical nature to his suggestions.

Furthermore, I would like to acknowledge Rémi Dreyfus's important contribution to the present work. During his short stay in Konstanz in February, some fruitful discussions and a nice presentation of his experimental results have influenced the focus of my work and provided me with a good deal of motivation for this project.

Nathan Isert deserves special thanks for spending hours with the tedious verification of the mobility tensors close to a wall! After having calculated them myself in the first place, I know very well that this can by no means be called a pleasant task ... Cheers, mate!

As far as this text is concerned, I am very grateful to the people who proofread the manuscript for all their critical suggestions. This provided me with an invaluable assistance for improving the presentation and readability of this text. I am aware of the fact that many arguments herein were far less convincing or did not really come across before this correction. This thank you is directed especially to Holger Stark but it also applies to Michael Reichert, Nathan Isert and Peter Groß!

However, the last year has not only been work but also a lot of fun. It would be an understatement to refer to the atmosphere at work as simply amicable and pleasant. I believe this has been contributed to by all members of the group as well as some "workplace asylum seekers". Besides the people already mentioned this specifically refers to Michael Schmiedeberg, Andrej Grimm and Markus Müller. Thank you all for the interesting conversations and your company not only during the numerous coffee breaks!

It has also been great to be part of the group of Professor Georg Maret. I particularly enjoyed participating in the group outings and many other activities which would not have happened or not have been as much fun in our small group! Many thanks to all members of the Maret Group! I am also thankful for the benefits I have received in the form of talks and workshops of the International Research Training Group.

Moreover, I am very much indebted and grateful to my family for their constant support which has not been restricted to the past year! Without this I would not have been able to concentrate on my studies in the same way. The financial support I have received is but one aspect of this complemented by many other and immaterial things. For this I would like to heartily thank my parents and my grandmother!

Last but not least, I would like to express my gratitude to Tina, who was very understanding and helpful during the past year. This was necessary during the last two months more than at other times. Quite often, I was too absorbed in my work to find the time for her she deserved. Nevertheless, her constant support and company has meant a lot to me! I have also appreciated the patience and endurance that might have been necessary at times with someone who only has physics on his mind.

Chapter 9

Zusammenfassung

Auf der Größen- und Zeitskala von biologischen Mikroorganismen werden hydrodynamische Gesetzmäßigkeiten wichtig, die uns im Alltagsleben gänzlich unbekannt sind. Bewegung ist ein Prozess, der in unserer Erfahrungswelt weitestgehend durch Trägheit bestimmt ist, was bei einer bewegten Flüssigkeit zu Turbulenzen führt. Im Bereich der niedrigen Reynolds Zahlen hingegen spielt Trägheit keine Rolle und jegliche Bewegung ist einzig durch Reibung mit der umgebenden Flüssigkeit bestimmt. Für einen bewegten Körper bedeutet dies, dass seine Bewegung genau so lange aufrechterhalten bleibt, wie eine äußere Kraft auf ihn wirkt. Fällt die schiebende Kraft weg, so hält er augenblicklich an. Des weiteren ruft jeder sich bewegende Körper ein weitreichendes, laminares Strömungsfeld in seiner Umgebung hervor, das den Bewegungszustand anderer, sich in der Nähe befindender Körper beeinflusst. Dadurch verändern sich deren Bewegungsrichtung und Geschwindigkeit. Diesen Sachverhalt bezeichnet man als hydrodynamische Wechselwirkungen.

Es ist nicht einfach, sich bei niedrigen Reynolds Zahlen fortzubewegen. E.M. Purcells Artikel "Life at low Reynolds number" [32] erläutert diese Problematik auf anschauliche Weise. In einer Umgebung, die keine Trägheit kennt, bedarf es eines nicht-reziproken Bewegungsablaufs, um sich durch eine zyklische Deformation fortbewegen zu können. Die meisten uns bekannten Schwimmtechniken sind somit nutzlos. Auf diese Besonderheit sind die Fortbewegung und der Flüssigkeitstransport von Bakterien abgestimmt. *E. coli* Bakterien schwimmen, indem sie einen helisch geformten Stab, der einem Korkenzieher ähnelt, drehen. Der Durchmesser des Stabes beträgt nur wenige Nanometer und der in der Zellwand verankerte Rotationsmotor ist ein wahres "Wunderwerk der Technik" auf molekularer Größe [1]. *Spermatozoa* schwimmen durch fortlaufende Wellen entlang ihrer Geißeln, die vom Kopf aus starten [5]. Die Oberflächen anderer Zellen, wie zum Beispiel die des *Paramecium*-Einzellers (Pantoffeltierchen), sind mit feinen Härchen bestückt, die Zilien genannt werden. Sie bewerkstelligen einen Flüssigkeitstransport entlang der Oberfläche durch einen asymmetrischen und zyklischen Bewegungsablauf. Flagellen und Zilien haben ein kompliziertes Innenleben auf der Größenskala von Nanometern. Die Schlagbewegung von Zilien beruht auf einem so genannten Axonem. Dies ist eine zylindrische Anordnung von meist neun äußeren und zwei inneren Mikrotubuli-Paaren, die sich durch Dyneinmotoren gegeneinander verschieben. Daraus resultieren interne Spannungen, die zur Krümmung der Zilie führen [7].

In dieser Arbeit geht es allerdings nicht in erster Linie um die Funktionsweise der genannten Nanomotoren. Vielmehr steht die hydrodynamische Umgebung solcher Antriebsmechanismen im Vordergrund. Unter diesem Gesichtspunkt beleuchtet die vorliegende Arbeit die

Hydrodynamik im Bereich der niedrigen Reynolds Zahlen nebst einer ausführlichen Darstellung hydrodynamischer Wechselwirkungen. Zilien und Flagellen werden dann mithilfe des so genannten *Bead-spring Models* simuliert. Dafür wird ein elastischer Stab durch eine Kette von Kugeln angenähert. Diskretisierte Dehnungs- und Biegekräfte wirken auf die Kugelmittelpunkte und hydrodynamische Wechselwirkungen lassen sich als Wechselwirkungen zwischen Kugeln implementieren. Wie auch im Kontinuumsmodell eines dünnen elastischen Stabes [38], unterliegt das "Bead-spring Model" Skalengesetzen, sodass die Dynamik in reduzierten Größen darstellbar ist.

Im Gegensatz zu Lagomarsinos [23] Simulationsstudie, in der ein solches Filament durch periodische Randbedingung bewegt und der damit verbundene Antrieb untersucht wird, verwenden wir ein realistischeres Modell, das in Analogie zu dem inhärent aktiven Antrieb biologischer Zilien auf einen Antrieb setzt, der an jeder Stelle des Filaments lokal wirkt. Um das zu realisieren nehmen wir an, die Kugeln seien superparamagnetisch. Ein externes, zeitabhängiges Magnetfeld führt dann zu Dipol-Dipol-Wechselwirkungen, wodurch das Filament angetrieben wird. Der Antrieb ist somit über die gesamte Länge des Filaments verteilt, wobei benachbarte Dipole stark koppeln und weiter entfernte Dipole sich nur schwach beeinflussen. Die Idee hierfür verdanken wir den Arbeiten von R. Dreyfus *et al.* [11] und J. Bibette *et al.* [14], die biomimetische Flagellen aus superparamagnetischen Kolloiden zusammensetzen. Diese Teilchen-Ketten sind das experimentelle Analogon unseres "Bead-spring Models" und verfügen ebenfalls über Elastizität in Form von Biege- und Dehnungskräften.

Im Rahmen dieser Arbeit wurden zwei unterschiedliche Systeme basierend auf dem "Bead-spring Model" untersucht. Der "One-armed Swimmer" besteht aus einem Filament, das an einem größeren Zellkopf befestigt ist. Durch eine periodische Richtungsabhängigkeit des magnetisches Feldes kommt eine Fortbewegung zustande. Zentrale Eigenschaften dieses Schwimmers wie Geschwindigkeit, Effizienz und die Abhängigkeit dieser Größen von der Geometrie der magnetischen Anregung wurden untersucht. Die Ergebnisse tragen zu einem umfassenden Verständnis des "One-armed Swimmers" bei, der unlängst von R. Dreyfus *et al.* [11] als erster experimenteller Mikro-Schwimmer realisiert wurde. Ein Vergleich experimenteller Daten mit unseren Simulationsergebnissen zeigt eine beeindruckende qualitative Übereinstimmung auf; auch quantitativ unterscheiden sich die Werte nur geringfügig, was angesichts der nur unvollständig bekannten hydrodynamischen Eigenschaften und weiterer Differenzen zwischen Simulation und Experiment im Detail als voller Erfolg gewertet werden muss.

Als zweites Simulationsmodell wurde der asymmetrische Schlagzyklus einer an einer Wand verankerten Zilie untersucht. Die Asymmetrie wird durch (i) unterschiedliche Schlaggeschwindigkeiten oder (ii) unterschiedliche Magnetfeldstärken für "Power"- und "Recovery"-Schlag erreicht. Beide Varianten sind funktionsfähig und führen zum Flüssigkeitstransport entlang der Oberfläche, wobei die Effizienz des Modells (i) deutlich überlegen ist. Zusätzlich besticht Modell (i) durch eine einfacher verständliche Dynamik. Für dieses System wurde ein effizienter Operationsmodus identifiziert, der eine hohe Leistungsaufnahme mit hoher Leistungsumwandlung vereinbart. Dies wäre ein geeignetes System für eine experimentelle Umsetzung.

Des weiteren wurde mit der Untersuchung des Einflusses von hydrodynamischen Wechselwirkungen auf die Dynamik eines Systems mit mehreren Zilien begonnen. Erste Ergebnisse zeigen, dass hydrodynamische Wechselwirkungen die Effizienz des Schlagzyklus erhöhen. Weiter besteht die Hoffnung, mit diesem Modell die Synchronisation mehrerer Zilien zu beschreiben und ferner aufzuzeigen, dass hydrodynamische Kopplung innerhalb eines dichten Zilien-Teppichs für die komplexen kollektiven Schlagmuster der so genannten *Metachronal Waves* verantwortlich ist, wie schon lange vermutet wird [36].

Appendix A

Rotne-Prager level HI mobility matrices near a planar boundary

In the following the derivation of an approximation of hydrodynamic interactions for the self-mobility of a single sphere and for two-sphere interactions in the proximity of a bounding wall with no-slip boundary condition is sketched. Calculations were carried out using Maple.

A.1 Blake's tensor components

As in Oseen or Rotne-Prager approximation, the mobility matrices are assumed to be pairwise additive. Consider two spheres labelled sphere 1 and sphere 2, then Blake's Green's function is given by:

$$\mathbf{G}^{Blake}(\mathbf{r}_1, \mathbf{r}_2) = \mathbf{G}(\mathbf{r}_1 - \mathbf{r}_2) - \mathbf{G}(\mathbf{r}_1 - \bar{\mathbf{r}}_2) + \delta\mathbf{G}^{im}(\mathbf{r}_1, \bar{\mathbf{r}}_2) \ , \tag{A.1}$$

where $\mathbf{G}(\mathbf{x} - \mathbf{y})$ is the Oseen tensor and $\delta\mathbf{G}^{im}(\mathbf{x}, \mathbf{y'})$ contains a stresslet and a sourcelet contribution at the image position. The vectors are taken as defined in section 3.8 and the distance between sphere 1 and the image system of sphere 2, s, is defined:

$$\begin{aligned} \mathbf{r}_1 = (x_1, y_1, z_1) \ ; \ \mathbf{r}_2 = (x_2, y_2, z_2) \ ; \ \bar{\mathbf{r}}_2 = (x_2, y_2, -z_2) \ , \\ s = |\mathbf{r}_1 - \bar{\mathbf{r}}_2| = \sqrt{(x_1 - x_2)^2 + (y_1 - y_2)^2 + (z_1 + z_2)^2} \ . \end{aligned}$$

In order to be able to obtain matrix components as simple as possible we will assume the wall to be in the xy-plane, that is at $z = 0$ without loss of generality. The sourcelet and stresslet of Blake's image system are given as matrix components in [21] or can alternatively be calculated from

$$\mathbf{G}^{stresslet}_{\alpha\beta}(\mathbf{x}) = \frac{1}{8\pi\eta}(1 - 2\delta_{\beta z})\frac{\partial}{\partial x_\beta}\left(\frac{x_\alpha}{|\mathbf{x}|^3}\right) \ , \tag{A.2}$$

$$\mathbf{G}^{sourclet}_{\alpha\beta}(\mathbf{x}) = \frac{1}{8\pi\eta}(1 - 2\delta_{\beta z})\frac{\partial}{\partial x_\beta}\left(\frac{\delta_{\alpha\beta}}{|\mathbf{x}|} + \frac{\mathbf{x}_\alpha \mathbf{x}_\beta}{|\mathbf{x}|^3} \ , \right) \tag{A.3}$$

the subscripts α, β denote component indices. The elements of Blake's tensor are given in

Cartesian coordinates by:

$$
\begin{aligned}
(\delta\mathbf{G}^{im})_{xx} &= -2z_1z_2\left(\frac{1}{s^3}-3\frac{(x_1-x_2)^2}{s^5}\right)\\
(\delta\mathbf{G}^{im})_{yy} &= -2z_1z_2\left(\frac{1}{s^3}-3\frac{(y_1-y_2)^2}{s^5}\right)\\
(\delta\mathbf{G}^{im})_{zz} &= 2z_1z_2\left(\frac{1}{s^3}-3\frac{(z_1+z_2)^2}{s^5}\right)\\
(\delta\mathbf{G}^{im})_{xy} &= 6\frac{z_1z_2\,(x_1-x_2)\,(y_1-y_2)}{s^5}\\
(\delta\mathbf{G}^{im})_{yx} &= (\delta\mathbf{G}^{im})_{xy}\\
(\delta\mathbf{G}^{im})_{xz} &= 2\,(x_1-x_2)\left(\frac{{z_1}^2}{s^3}-3\frac{z_1z_2\,(z_1+z_2)}{s^5}\right)\\
(\delta\mathbf{G}^{im})_{zx} &= 2\,(x_1-x_2)\left(\frac{{z_1}^2}{s^3}+3\frac{z_1z_2\,(z_1+z_2)}{s^5}\right)\\
(\delta\mathbf{G}^{im})_{yz} &= 2\,(y_1-y_2)\left(\frac{{z_1}^2}{s^3}-3\frac{z_1z_2\,(z_1+z_2)}{s^5}\right)\\
(\delta\mathbf{G}^{im})_{zy} &= 2\,(y_1-y_2)\left(\frac{{z_1}^2}{s^3}+3\frac{z_1z_2\,(z_1+z_2)}{s^5}\right)\quad .
\end{aligned}
$$

A.2 Sourcelet and stresslet components

The sourcelet and stresslet contributions to the components of the mobility matrix for two spheres interacting close to a wall are printed below. They are obtained by applying the differential operator $\left(1+\frac{a^2}{6}\nabla^2_{\mathbf{r}_1}\right)\left(1+\frac{a^2}{6}\nabla^2_{\mathbf{r}_2}\right)$ to the non-Oseen terms in Blake's tensor (see section 3.8). The Laplacians were calculated with the help of Maple. As this produces very complex expressions, all terms were contracted manually to a more compact representation. These terms were expanded and checked against the original Maple expressions to make sure that no errors were introduced by the manual simplification.

A.2.1 Matrix components of the self-mobilities

Due to the axial symmetry of the sphere with its image system all but the diagonal elements vanish and the xx and the yy elements are identical:

$$
\delta\boldsymbol{\mu}_{self}=\frac{1}{6\pi\eta a}\begin{pmatrix}\nu & 0 & 0\\ 0 & \nu & 0\\ 0 & 0 & 2\nu\end{pmatrix}\quad, \tag{A.4}
$$

where

$$
\nu=-\frac{3}{16}\left[\frac{a}{z}-\left(\frac{a}{z}\right)^3+\frac{1}{3}\left(\frac{a}{z}\right)^5\right]\quad. \tag{A.5}
$$

Note that this expression, or rather the full self-mobility of a sphere close to a wall, equation (A.6), has been confirmed by comparison with an expression from [12, 19]. Unfortunately, though, the authors do not give expressions for cross-mobilities of two spheres close to a boundary.

A.2.2 Matrix components of the cross-mobilities

The components of the vector $\mathbf{r}_1 - \overline{\mathbf{r}}_2$ are conveniently defined as

$$R_x = (x_1 - x_2) \; ; \; R_y = (y_1 - y_2) \; ; \; R_z = (z_1 + z_2) \; .$$

As the bounding wall is in the xy-plane, it follows from symmetry that the xy and yx elements are identical as is already the case in Blake's tensor. Furthermore, the xx and yy elements are formally equivalent when R_x is interchanged with R_y. The same holds for the xz and yz or zx and zy elements, respectively.

$$\begin{aligned}
8\pi\eta(\delta\boldsymbol{\mu}_{12})_{xx} &= -2z_1z_2\left(\frac{1}{s^3} - 3\frac{R_x^2}{s^5}\right) - \frac{2a^2}{s^7}R_z^2(4R_x^2 - R_y^2 - R_z^2) \\
&- \frac{2a^4}{3s^9}(4R_x^4 - R_y^4 + 4R_z^4 + 3R_x^2R_y^2 + 3R_y^2R_z^2 - 27R_x^2R_z^2) \\
8\pi\eta(\delta\boldsymbol{\mu}_{12})_{yy} &= -2z_1z_2\left(\frac{1}{s^3} - 3\frac{R_y^2}{s^5}\right) - \frac{2a^2}{s^7}R_z^2(4R_y^2 - R_x^2 - R_z^2) \\
&- \frac{2a^4}{3s^9}(4R_y^4 - R_x^4 + 4R_z^4 + 3R_x^2R_y^2 + 3R_x^2R_z^2 - 27R_y^2R_z^2) \\
8\pi\eta(\delta\boldsymbol{\mu}_{12})_{zz} &= 2z_1z_2\left(\frac{1}{s^3} - 3\frac{R_z^2}{s^5}\right) - \frac{2a^2}{s^7}R_z^2(3(R_x^2 + R_y^2) - 2R_z^2) \\
&- \frac{2a^4}{3s^9}(3R_x^4 + 3R_y^4 + 6R_x^2R_y^2 - 24R_z^2(R_x^2 + R_y^2) + 8R_z^4) \\
8\pi\eta(\delta\boldsymbol{\mu}_{12})_{xy} &= 6\frac{z_1z_2R_xR_y}{s^5} - \frac{10a^2}{s^7}R_xR_yR_z^2 - \frac{10a^4}{3s^9}(R_x^2 + R_y^2 - 6R_z^2)R_xR_y \\
8\pi\eta(\delta\boldsymbol{\mu}_{12})_{yx} &= 8\pi\eta\delta(\boldsymbol{\mu}_{12})_{xy} \\
8\pi\eta(\delta\boldsymbol{\mu}_{12})_{xz} &= 2R_x\left(\frac{{z_1}^2}{s^3} - 3\frac{z_1z_2R_z}{s^5}\right) + R_xa^2\left(\frac{2}{3}\frac{1}{s^3} + \frac{10}{s^7}R_z^3 - \frac{2}{s^5}\left[R_z + 2(z_1^2 + z_1z_2)\right]\right) \\
&+ \frac{10a^4}{3s^9}R_x(3R_z[R_x^2 + R_y^2] - 4R_z^3) \\
8\pi\eta(\delta\boldsymbol{\mu}_{12})_{zx} &= 2R_x\left(\frac{{z_1}^2}{s^3} + 3\frac{z_1z_2R_z}{s^5}\right) + R_xa^2\left(\frac{2}{3}\frac{1}{s^3} - \frac{10}{s^7}R_z^3 + \frac{2}{s^5}\left[R_z - 2(z_1^2 + z_1z_2)\right]\right) \\
&- \frac{10a^4}{3s^9}R_x(3R_z[R_x^2 + R_y^2] - 4R_z^3) \\
8\pi\eta(\delta\boldsymbol{\mu}_{12})_{yz} &= 2R_y\left(\frac{{z_1}^2}{s^3} - 3\frac{z_1z_2R_z}{s^5}\right) + R_ya^2\left(\frac{2}{3}\frac{1}{s^3} + \frac{10}{s^7}R_z^3 - \frac{2}{s^5}\left[R_z + 2(z_1^2 + z_1z_2)\right]\right) \\
&+ \frac{10a^4}{3s^9}R_y(3R_z[R_x^2 + R_y^2] - 4R_z^3) \\
8\pi\eta(\delta\boldsymbol{\mu}_{12})_{zy} &= 2R_x\left(\frac{{z_1}^2}{s^3} + 3\frac{z_1z_2R_z}{s^5}\right) + R_ya^2\left(\frac{2}{3}\frac{1}{s^3} - \frac{10}{s^7}R_z^3 + \frac{2}{s^5}\left[R_z - 2(z_1^2 + z_1z_2)\right]\right) \\
&- \frac{10a^4}{3s^9}R_y(3R_z[R_x^2 + R_y^2] - 4R_z^3)
\end{aligned}$$

A.3 Full mobility functions

In an N particle system with an infinitely extended planar boundary at $z = 0$, the pairwise additive mobility functions are:

$$\boldsymbol{\mu}_{ii}^{wall} = \mu_0 \hat{\mathbf{I}} - \boldsymbol{\mu}^{rp}(\mathbf{r}_i - \overline{\mathbf{r}}_i) + \delta\boldsymbol{\mu}_{self} \tag{A.6}$$

$$\boldsymbol{\mu}_{ij}^{wall} = \boldsymbol{\mu}^{rp}(\mathbf{r}_i - \mathbf{r}_j) - \boldsymbol{\mu}^{rp}(\mathbf{r}_i - \overline{\mathbf{r}}_j) + \delta\boldsymbol{\mu}_{ij} \ . \tag{A.7}$$

Here, the $\boldsymbol{\mu}^{rp}(\mathbf{x} - \mathbf{y})$ are Rotne-Prager tensors and come from the Oseen terms in Blake's tensor. They give the interaction with the image bead. The contributions $\delta\boldsymbol{\mu}_{self}$ and $\delta\boldsymbol{\mu}_{ij}$ are given in the two preceding sections and are further corrections from image stresslet and sourcelet.

Appendix B

Simulation parameters

We use two different sets of parameters in our simulations (see section 4.6.3). In order to study the properties of the simulation models it is necessary to vary a small number of essential parameters. Most other parameters are either held constant at all times or fittingly adjusted as necessary. In the following we distinguish three parameter categories:

1. **Essential system parameters** are shown at typical values in bold print. These parameters are frequently used to vary the dimensionless Sperm number Sp, the rescaled magnetic field B_s and the wiggling angle is just φ_{max}.

2. *Parameters adjusted as necessary* are shown at typical values in italic print.

3. Parameters constant at all times (unless explicitly stated) are shown in normal print

B.1 Parameter set I

Parameter	Symbol	Value
Number of beads	N	20
Radius of beads	a	2.25 μm
Radius of head	a_0	$8a$
Bond length	l_0	3a
Magnetic susceptibility	χ	1.704
Fluid viscosity	η	$1 \cdot 10^{-3}$ Ns/m^2
Spring constant	k	1 N/m
Bend stiffness	A	$6.75 \cdot 10^{-18}$ Nm
Magnetic field strength	B	0.4 T
Wiggling frequency	ω	500 Hz
Wiggling angle	φ_{max}	57°
Integration time step	Δt	$1 \cdot 10^{-8}$ s
Number of simulation cycles		15

B.2 Parameter set II

Parameter	Symbol	Value
Number of beads	N	20
Radius of beads	a	0.5 μm
Radius of head	a_0	$5a$
Bond length	l_0	3a
Magnetic susceptibility	χ	0.993
Fluid viscosity	η	$1 \cdot 10^{-3}$ Ns/m^2
Spring constant	k	$1.5 \cdot 10^{-3}$ N/m
Bend stiffness	A	$4.5 \cdot 10^{-22}$ Nm
Magnetic field strength	B	30 mT
Wiggling frequency	ω	10 Hz
Wiggling angle	φ_{max}	45°
Integration time step	Δt	$1 \cdot 10^{-6}$ s
Number of simulation cycles		15

Bibliography

[1] Berg, H.C.; Anderson, R.A.: *Bacteria swim by rotating their flagellar filaments.* Nature **245**, 1973, p. 380-382

[2] Blake, J.R.: *A note on the image system for a stokeslet in a no-slip boundary.* Proc. Camb. Phil. Soc., Vol. **70**, 1971, p. 303-310

[3] Bossis, G.; Meunier, A.; Sherwood, J.D.: *Stokesian dynamics simulations of particle trajectories near a plane.* Phys. Fluids A, Vol. **3**, No. 8, 1991, p. 1853-1858

[4] Brandt, S.; Dahmen, H. D.: *Elektrodynamik. Eine Einführung in Experiment und Theorie.* Springer, Berlin 1997, p. 45ff

[5] Brennen, Christopher; Winet, Howard: *Fluid mechanics of propulsion by cilia and flagella.* Ann. Rev. of Fluid Mech., Vol. **9**, 1977, p. 339-398

[6] Camalet, Sébastian; Jülicher, Frank: *Self-organized beating and swimming of internally driven filaments.* Phys. Rev. Lett., Vol. **82**, No. 7, 1999

[7] Camalet, Sébastian; Jülicher, Frank: *Generic aspects of axonemal beating.* New Journal of Physics, Vol. **2**, 2000

[8] Carrasco, Beatriz; Torre, José García de la: *Hydrodynamic properties of rigid particles: comparison of different modeling and computational procedures.* Biophysical Journal, Vol. **75**, No. 6, 1999, p. 3044-3057

[9] Cichocki, B.; Jones, R.B.; Kutteh, R.; Wajnryb, E.: *Friction and mobility for colloidal spheres in Stokes flow near a boundary: The multipole method and applications.* Journal of Chemical Physics, Vol. **112**, No. 5, 2000, p. 2548-2561

[10] Dhont, Jan K. G.: *An introduction to dynamics of colloids.* Elsevier Science, Amsterdam 1996

[11] Dreyfus, Rémi; Baudry, Jean; Roper, Marcus L.; Fermigier, Marc; Stone Howard A.; Bibette, Jérôme: *Microscopic artificial swimmers.* Nature **437**, 2005, p. 862-865

[12] Dufresne, Eric R.; Squires, Todd M.; Brenner, Michael P.; Grier, David G.: *Hydrodynamic coupling of two brownian spheres to a planar surface*, Phys. Rev. Lett., Vol. **85**, No. 15, 2000

[13] Durlofsky, L.; Brady, J.F.; Bossis, G.: *Dynamic simulation of hydrodynamically interacting particles.* Journal of fluid mechanics, Vol. **180**, No. 21, 1987

[14] Goubault, C.; Jop, P.; Fermigier, M.; Baudry, J.; Bertrand, E.; Bibette, J.: *Flexible magnetic filaments as micromechanical sensors.* Phys. Rev. Lett, Vol. **91**, No. 26, 2003

[15] Grassia, P.S.; Hinch, E.J.: *Computer simulations of polymer chain relaxation via Brownian motion.* Journal of Fluid Mechanics, Vol. **308**, 1996, p. 255-288

[16] Greiner, W.; Stock, H.: *Theoretische Physik 2a, Hydrodynamik* (1991)

[17] Gueron, Shay; Levit-Gurevich, Konstantin: *Computation of the internal forces in cilia: application to ciliary motion, the effects of viscosity, and cilia interactions.* Biophysical Journal, Vol. **74**, No. 4, 1998, p. 1658-1676

[18] Gueron, Shay; Levit-Gurevich, Konstantin: *Energetic considerations of ciliary beating and the advantage of metachronal coordination.* PNAS, October 26, 1999; 96(22): 12240 - 12245.

[19] Happel, John; Brenner, Howard: *Low Reynolds number hydrodynamics.* Noordhoff, Leyden 1973

[20] Jeffrey, D.J.; Onishi, Y.: *Calculation of the resistance and mobility functions for two unequal rigid spheres in low-Reynolds-number flow*, Journal of Fluid Mechanics, Vol. **139**, 1983, p. 261-290

[21] Jones, Robert B.; Kutteh Ramzi: *Sedimentation of colloidal particles near a wall: Stokesian dynamics simulations.* Phys. Chem. Chem. Phys., Vol. **1**, 1999, p. 2131-2139

[22] Kim, S.; Karilla, S.J.: *Microhydrodynamics, principles and selected applications.* Butterworth-Heinemann, Boston 1991

[23] Lagomarsino, Marco Cosentino: *Biologically inspired problems concerning semifliexible filaments.* Dissertation Thesis, University of Leiden 2004. Online at www.amolf.nl

[24] Lagomarsino, M. C.; Pagonabarraga, I; Lowe, C.P.: *Hydrodynamic induced deformation and orientation of a microscopic elastic filament.* Phys. Rev. Lett., Vol. **94**, 2005

[25] Landau, L.D; Lifshitz, E. M.: *Lehrbuch der theoretischen Physik VI, Hydrodynamik.* Akademie Verlag, Berlin 1991

[26] Lowe, Christopher P.: *Dynamics of filaments: modelling the dynamics of driven microfilaments.* Philos. Trans. R. Soc. Lond. B Biol. Sci., 2003

[27] Manghi, Manoel; Schlagberger, Xaver; Netz, Roland R.: *Propulsion with a rotating elastic nano-rod.* Submitted to Phys. Rev. Lett., 2005

[28] Najafi, Ali; Golestanian, Ramin: *Simple swimmer at low Reynolds number: three linked spheres.* Phys. Rev. E, Vol. **69**, 2004

[29] Nelson, Philip: *Biological physics: energy, information, life.* Freeman, New York 2004

[30] Numerical Recipes in C: The art of scientific computing. Cambridge University Press, Cambridge 1992

[31] Perkins, G.S.; Jones, R.B.: *Hydrodynamic interaction of a spherical particle with a planar boundary*. Physica A, Vol. **189**, 1992, p. 447-477

[32] Purcell, E.M: *Life at low Reynolds number*. American Journal of Physics, Vol. **45**, No. 1, 1977

[33] Reichert, Michael; Stark, Holger: *Hydrodynamic coupling of two rotating spheres trapped in harmonic potentials*. Phys. Rev. E, Vol. **69**, 2004

[34] Reichert, Michael; Stark, Holger: *Synchronization of rotating helices by hydrodynamic interactions*. Eur. Phys. Journal E, Vol. **17**, 2005, p. 493ff

[35] Roper, Marcus L.; Dreyfus, Rémi; Baudry, Jean; Fermigier, Marc; Bibette, Jérôme; Stone Howard A.: *On the dynamics of magnetically driven elastic filaments*. submitted to Journal of Fluid Mechanics, 2005

[36] Taylor, Sir Geoffrey: *Analysis of the swimming of microscopic organisms*. Proc. Roy. Soc., A **209**, 1951, p. 447-461

[37] Torre, José García de la; Bloomfied, V.A.: *Hydrodynamic theory of swimming of flagellated microorganisms*. Biophysical Journal, Vol. **20**, 1977, p. 49-67

[38] Wiggins, Chris H.; Riveline, D.; Ott, A.; Goldstein, Raymond E.: *Trapping and wiggling: elastohydrodynamics of driven microfilaments*. Biophysical Journal, Vol. **74**, 1998, p. 1043-1060

[39] Wiggins, Chris H.; Goldstein, Raymond E.: *Flexive and propulsive dynamics of elastica at low Reynolds number*. Phys. Rev. Lett, Vol. **80**, No. 17, 1998